III-V / Silicon tandem solar cell grown with molecular beam epitaxy

Amadeo Michaud

Sorbonne Université

Ecole doctorale Physique et Chimie des matériaux

Total GRP & Centre de Nanoscience et de Nanotechnologies

III-V/ Silicon tandem solar cell grown with Molecular Beam Epitaxy

MICHAUD Amadéo

Thèse de doctorat de Physique des matériaux

Dirigée par Jean-Christophe Harmand et Jara Fernandez Martin

Présentée et soutenue publiquement le [Date de soutenance]

Devant un jury composé de:

Alain Le Corre

James Connolly

Wilfried Favre

Andrea Gauzzi

Pou diw ke la vi a no man sé an batay

Sé alé i ka alé i pa ni tan pou fè détay

Mè nou pé pa gannié si nou ka pétayé

Pa pè an nou lévé i ja tan pou nou alé

Arété di kow boug mwen kè ou pé pa

On moun ki pé pa sé an moun ki vé pa

Vansé sé pa san pèn' tchilé sé pa la pèn'

Pansé positif mé pa pansé pasif

Pou pé pété tout' pot' ké ou vlé pété

E. sy Kennenga

Résumé

Le photovoltaïque terrestre est actuellement largement dominé par des dispositifs à base de Silicium. La limite théorique d'efficacité de photoconversion pour les cellules solaires en silicium est de l'ordre de 29%. Avec des modules photovoltaïques ayant une efficacité de 26.3% sur le marché, la filière Si est à un niveau de maturité avancée et exploite déjà la quasi-totalité du potentiel de ce genre de cellule solaires. Le travail exposé ici traite d'une autre voie d'amélioration de l'efficacité de conversion des dispositifs photovoltaïques. En effet, les cellules solaires tandem, assemblées en empilant plusieurs cellules permettent de dépasser les limites associées aux cellules Si. La complémentarité importante des cellules solaire III-V avec les cellules Si permettrai en théorie d'atteindre plus de 40% d'efficacité. Cette thèse vise à l'élaboration de cellule III-V performante et compatible avec un usage en tandem.

Dans un premier temps, l'épitaxie d'alliages phosphures a été étudiée et en particulier l'influence des conditions de croissance sur le GaInP. Une réduction de la pression en phosphore durant la croissance provoque des modulations de composition au sein de l'alliage. La température a un impact significatif sur la valeur de bande interdite qui diminue en augmentant la température. Des caractérisations de photoluminescence ont permis de définir les conditions optimales de croissance en maximisant le signal de luminescence de l'alliage. L'étude a notamment révélé que cru dans les conditions choisies, le GaInP présente moins de défaut et d'états profonds qu'à plus faibles températures de croissance. Enfin la capacité à atteindre des niveaux de dopages élevés dans l'alliage AlGaInP et l'impact de sa composition sur le dopage ont étés étudié.

Dans un second temps, la structure des cellules solaires simple jonction GaInP a été optimisée. Nous illustrons l'impact de la passivation de la surface des cellules par AlInP et AlGaInP, ainsi que l'amélioration du photo-courant par l'amincissement de l'émetteur dopé n. L'introduction de couche non-dopée dans la structure ne permit pas de remédier au problème de collection des porteurs constaté dans les cellules.

La couche limitant l'efficacité des cellules est composée de p-GaInP. Des caractérisations par Cathodoluminescence et Fluorescence résolue en temps d'échantillons identiques à cette couche ont été menées. Elles ont mis en avant une faible longueur de diffusion des porteurs générés dans le matériau. La comparaison de ces propriétés avec la littérature et celle mesurées pour GaInP épitaxié par MOCVD, indique que l'amélioration de l'efficacité des cellules passe par une augmentation de la mobilité des porteurs au sein du GaInP. Une solution pratique, combinant GaInP et AlGaAs dans une cellule à hétérojonction a été mise en œuvre. Ce type de structure est une autre perspective intéressante à l'avenir puisque des efficacités à l'état de l'art ont été mesurées.

Enfin nous avons développé un procédé permettant d'adapter les cellules pour un usage tandem. Les structures sont crues en inversé puis transférées sur verre ou wafer de silicium sans endommager leur performance. Toutefois, des améliorations sont toujours nécessaires pour permettre l'assemblage d'une cellule tandem fonctionnelle. En effet, la non-planéité introduite par les contacts arrières de la cellule III-V cause actuellement des problèmes de collage.

Mots-clé: Photovoltaïque, semiconducteurs III-V, MBE, cellule solaire tandem, GaInP.

Abstract

Terrestrial photovoltaic is dominated by Silicon based devices. For this type of solar cells, the theory predicts an efficiency limit of 29%. With photovoltaic modules showing 26.6% efficiency already, Silicon-based modules is a mature technology and harvest almost their full potential. In this work, we intend to explore another path toward the enhancement of photovoltaic conversion efficiency. Tandem solar cells that consist in stacking sub-cells, allow to overcome the Si efficiency limit. Since solar cells made of III-V semiconductors are complementary to Silicon solar cells, theory predicts that efficiency above 40% is attainable when combining those types of cells. Here we focus on the elaboration of a performant III-V solar cell, compatible for a tandem use.

The first stage of the PhD was to build know-how on phosphide alloys epitaxy with MBE. The influence of the growth conditions on GaInP properties was studied. We noted that composition modulations appear in the alloy when grown with low phosphorus pressure. The growth temperature also impacts the material bandgap, which reduces while increasing the temperature. Photoluminescence characterization served to select the best growth conditions by maximizing the photoluminescence efficiency. We could also highlight that in the conditions chosen, the GaInP exhibits less defect states. AlGaInP alloys are used for passivation purposes in the cells, the influence of the composition of the alloy on the Beryllium doping efficiency was studied.

Then GaInP single junction solar cells were fabricated. The different layers composing the cells were optimized. The impact of the front surface passivation with AlGaInP and AlInP was emphasized; improvement of the cell photocurrent by the thinning of the n-doped GaInP layer was also demonstrated. The introduction of a non-intentionally-doped layer in the structure was tested in order to remedy the limits encountered with photocurrent collection.

The p-GaInP composing the cells was eventually identified as the limiting factor. In depth characterization of samples mimicking the limiting layer was performed with cathodoluminescence and time-resolved fluorescence. A small diffusion length of the generated carriers was evidenced. Comparison with MOVPE and with literature values suggests that improving the carrier mobility in this layer is the main route to follow for improving of the GaInP cell efficiency. A practical solution was proposed and implemented: we designed a cell combining GaInP and AlGaAs in a heterojunction cell. This structure proves to be very relevant for the project since state of the art photoconversion efficiency of 18.7% was obtained.

Finally a process was developed to adapt the III-V solar cells to the tandem configuration. Inverted PV cells structures were grown and transferred on glass or Silicon hosts without degradation of their efficiency. Further improvement of the process is needed to build a full tandem device, in particular the back metallization of the III-V cells must be compatible with the bonding of the cells on the host substrate.

Keywords: Photovoltaics, III-V semiconductors, MBE, GaInP, tandem solar cells.

Remerciements

to be written

Contents

Chapter 1

Introduction to photovoltaics and tandem solar cells

1.1 Photovoltaic effect and current status

1.1.1 Presentation of the photovoltaic effect

The sun radiates energy over the whole solar system and above. It is at the origin of the equilibrium that permitted Life to develop on Earth and is powering most of the mechanisms involved in the life cycle (water cycle, biomass creation ...). Nature has been exploiting the solar energy for a long time with photosynthesis. Plants, for example, absorb light thanks to pigments that transform the radiation in chemical energy. This energy is then used to power reactions between minerals, water and CO_2 in order to synthetize the carbohydrate and organic molecules the plant needs to grow (see Figure 1.1).

In 1839, Antoine Becquerel discovered the photovoltaic effect using a conductive solution. But it was much later that the Bell lab managed to assemble solar panel that mimic the photosynthesis and creates electrical energy from light. The photovoltaic effect lies on the fact that when exposed to light , semiconductors absorb photons by promoting electrons from the valence band to the conduction band. The generated free carriers can be collected as a current flow. This is one of the semiconductor properties that are the cornerstone of photovoltaics for now.

The sun delivers more energy to the earth in one hour than we currently use from fossil fuels, nuclear power and all renewable energy sources combined in a year. Its potential as a renewable energy source, therefore, is vast. [1]

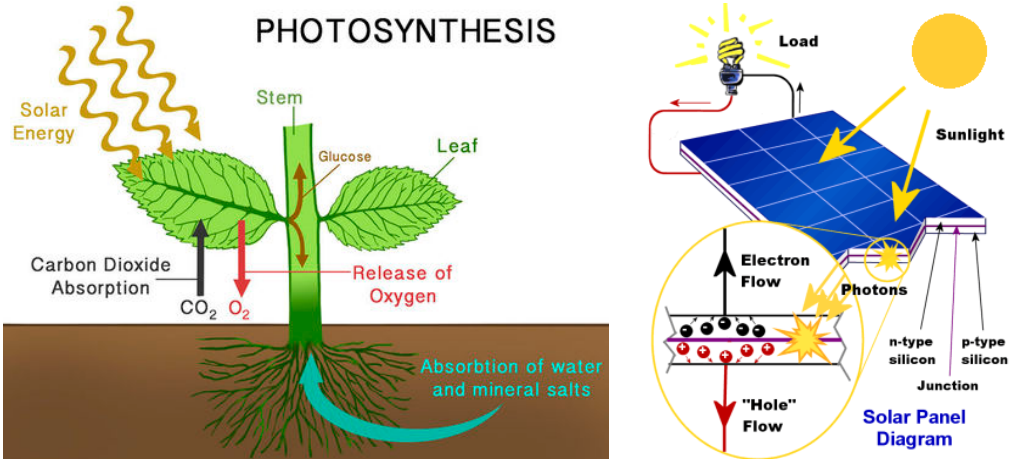

(a) From [2] (b)

Figure 1.1: From photosynthesis to photovoltaics. a) Natural photosynthesis process where solar energy is transformed in organic matter. b) Photovoltaic device transforming solar energy in electrical power.

1.1.2 Current PV market

In its report on Photovoltaics[3], Fraunhofer Institut for Solar Energy Systems estimated the global cumulative PV installation to 515 GW in 2018. PV currently accounts for only 1.7% of the electricity production worldwide, but it is a fast growing sector since its compound annual growth rate for the past seven years has been above 20%. Figure 1.2 illustrates how important is the PV capacity installed each year, further 100 GW installation is forecasted for 2019. Silicon-based technologies dominate the market: they accounted for 95% of the module production in 2018. Indeed thin film cell (CIGS, CdTe based) share have gradually decreased over the years (Figure 1.2).

Si cells are either multi-crystalline cells or crystalline cells (C-Si). Transition to more efficient structure for Si solar cell is ongoing with broader production of PERC cells (Passivated Emitter and Rear Cells) [5]. In this design, cells are passivated with Al_2O_3 and antireflection coating (ARC) is also deposited on the back of the cells. Laser opening of the ARC permits to contact the back of the cell with Aluminum,22% efficiency is obtained with this type of cell.

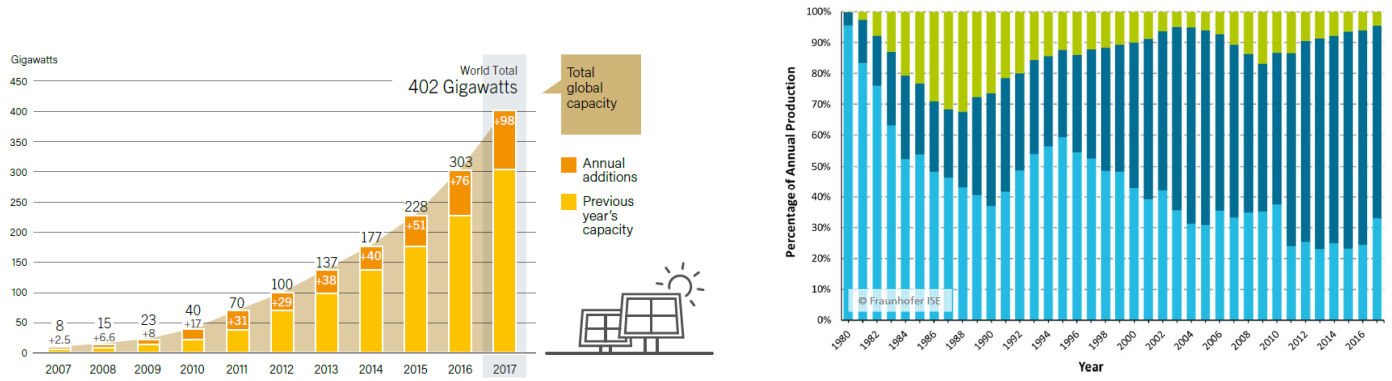

(a) (b)

Figure 1.2: a) Evolution of the global PV capacity (in GW). In orange, the capacity installed each year [4]. b) Repartition of the shares of the different technologies on the global PV production per year[3].

1.2 Climate stakes and energy prospects

In the recent years, global warming has attracted more and more attention from the public opinion and authorities. In 2015, the COP21 climate change conference gathered many actors from different countries in order to set clear goals to tackle climate change issues.

Following this event, the IPCC (Intergovernmental Panel on Climate Change) was formed and has since published a report drawing a clear picture of Climate change origins and consequences. Human kind is for now responsible for 1°C temperature raise from the pre-industrial era. Our past activities will continue to provoke temperatures to raise and effort must be made to limit this phenomenon. IPCC fixes a "1.5°C raise" target that would already have important consequences. Such an increase would cause sea level to rise, more extreme meteorological events and important migrations. Significant impact on biodiversity is forecasted, even for sea life as the increase of ocean temperature causes its acidification.

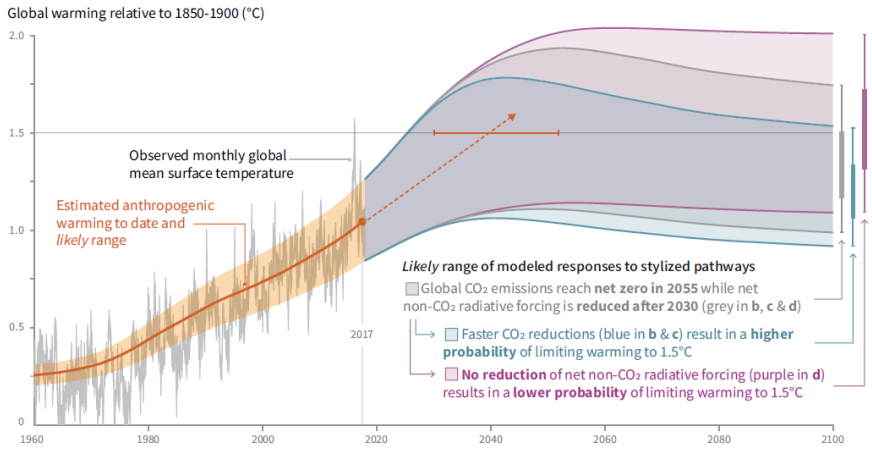

Figure 1.3: ICPP forecast on global warming evolution for different scenari [6].

The report recommendation to comply with this goal is to reduce drastically CO_2 emission. Emissions should be reduced by 45% in 2030 and a net zero CO_2 emission attained in 2050. Figure 1.3 shows the projected temperature for this scenario in purple. Blue range corresponds to a 0 emission reached in 2040.

Such a decreased of our CO_2 emission is extremely challenging and requires changes of our infrastructures and urban organization but most of all, a drastic change in the way we produce and consume energy. Transition to low carbon and sustainable sources of energy is compulsory.

Another challenge is related to the fact that energy demand will continue to grow. Indeed developing countries consumption will increase has they carry on securing their growth. It is interesting to see, in Figure 1.4, the geographic and the sector repartition of the demand in the future. In its scenario "Evolving Transition" (ET), developed in "Energy outlook" [7], British Petroleum forecasts an increase of 3.6 million toe of the energy demand (toe= ton oil equivalent), thus 41 900 TWh. They expect 75% of this growth to be used for power production (meaning for electrical power supply). Gas and renewables energies will provide 85% of this growth and Renewables will account for 15% of the energy mix in 2040.

However this Evolving Transition scenario is based on the assumption that the transition follows the manners and pace of the recent years. Focusing on CO_2, it only secures a stagnation of global yearly emission. They expose another scenario more consistent with IPCC goals, the Rapid transition (RT scenario) in which CO_2 emission does decrease over the year. In this case, renewables account for 30% of the energy mix in 2040.

Figure 1.5 emphasizes the share of solar in the renewable power generation based on the conservative ET scenario. It is clear that photovoltaics is a major source of renewables. Picturing the pace at which solar production would increase for the Rapid Transition, one understands that we cannot limit ourselves to the current market integration of photovoltaics. Better PV conversion efficiencies and higher power density are major stakes in the fight against global warming.

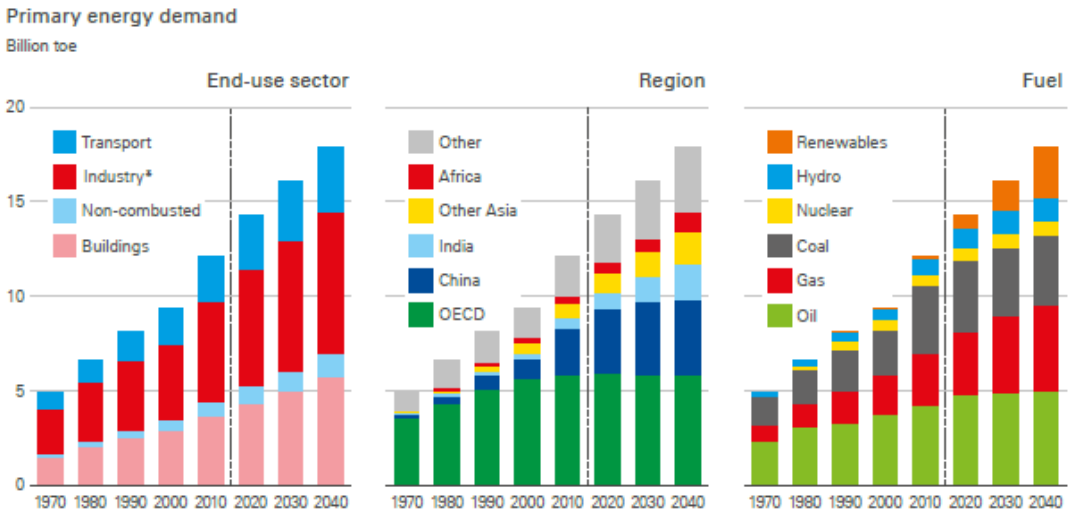

Figure 1.4: BP prediction of Energy demand growth depending on: the sector, the geographic area, or the energy source [7].

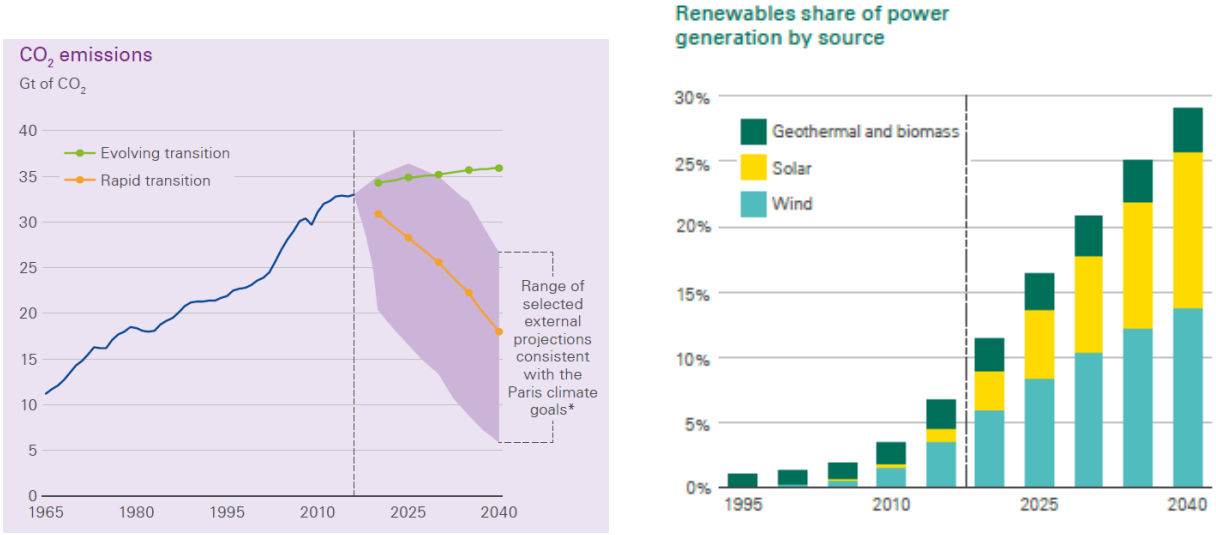

(a) (b)

Figure 1.5: a) Global CO_2 emission for a Energy transition scenari following: the current trends in green, emission in agreement with ICPP recommendation in yellow. b) Prediction of the share of each Renewable source in future power generation in the RT scenario [7].

For example, new concepts like virtual power plants, smart grids and building integrated PV (BIPV) will become tangible to bring power production closer to consumers. They will require more compact modules and therefore research on new PV technologies is needed to raise PV efficiency and build systems compatible with area restriction.

1.3 Single-junction solar cells limitations and path toward more efficient cells

1.3.1 PV cell limitations and losses

Silicon-based solar cells has proven itself as a robust and profitable technology. However in order to tackle the problem of increasing production need, Si based solar cells, and single junction cell more generally, have to overcome their intrinsic limitations.

In 1964, Shockley built the so called "Detailed balanced limit" (hereafter SQ limit) that predicts the maximum theoretical efficiency achievable for cells of a given bandgap value [8]. It accounts for entropic losses mainly linked to light (reemission, light leaks...) and energy losses from Carnot cycle and thermalisation mostly.

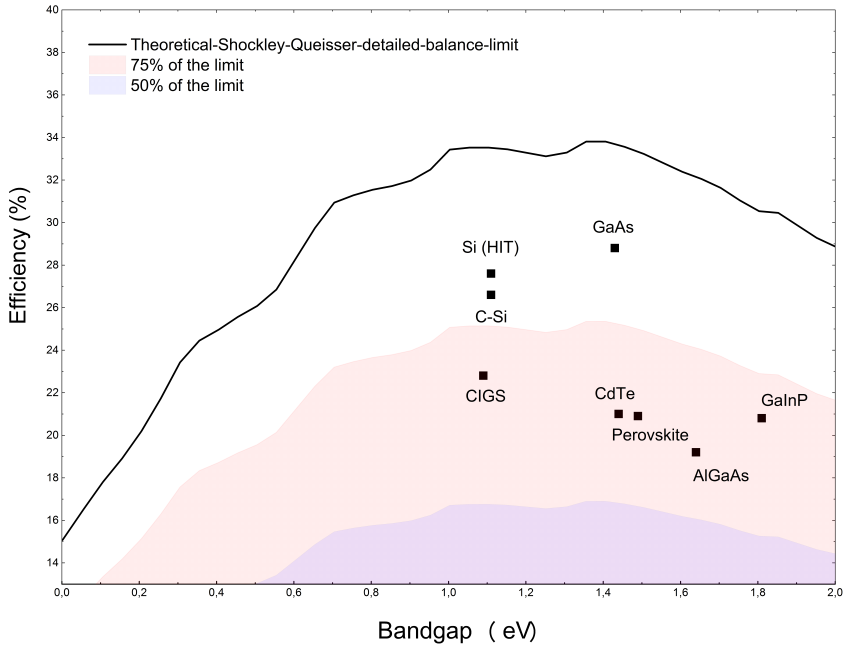

Figure 1.6: Schokley Queisser detailed balance limit and different materials efficiency record for single junction cells.

Practical efficiency limit is even lower because of losses related to the device and cell to modules losses, which will add up to those considered in the SQ limit. Figure 1.6 details the best efficiencies for different materials and how they perform in comparison with the SQ limit. Single junction solar cells cannot exceed 34% efficiency. Si and GaAs base technologies are already mature and close to the SQ limit, accounting for the additional practical limitations not much improvement is expected in the future. Other materials still offer room for improvement as they do not reach 75% of the SQ limit yet.

Figure 1.7 details the origins of energy losses leading to the current single junction cells efficiency and the associated solutions. Particular designs offer interesting way to reduce those losses, like light trapping solution [9] or hot carriers collection [10]. However they are limited to laboratory scale for now.

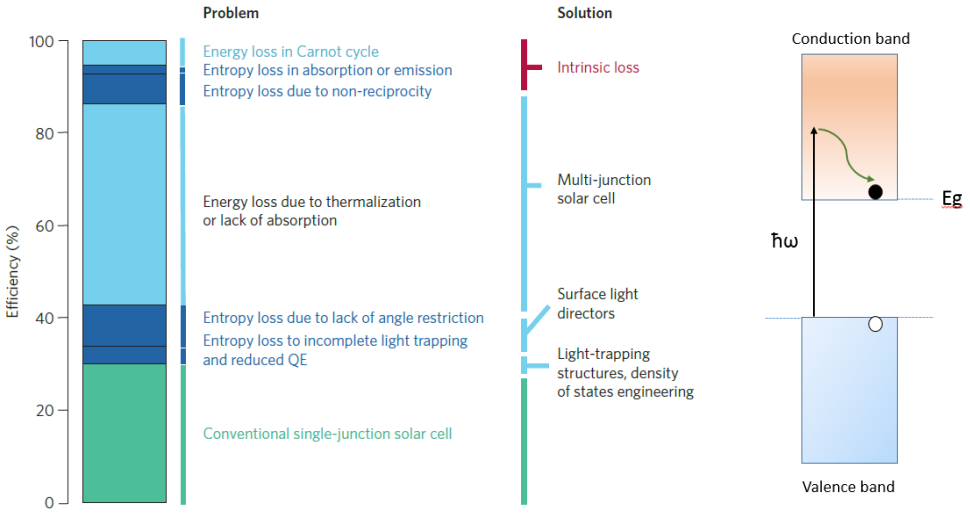

(a) [11] (b)

Figure 1.7: a) Different losses leading to 28.3% efficiency for GaAs single junction cell and associated solutions. b) Sketch of the thermalisation process.

1.3.2 Current technologies increasing the photoconversion efficiency

One of the implemented solution from the industry is the use of bi-facial Si modules. Using transparent back sheet modules and a grid back metallization on the Si cells, light can also be harvested on the back of the panels. The albedo (light reflected by the environment) provides an extra energy production without reducing the front side conversion efficiency [12, 13]. This promising method offers better energy production density at small additional cost. Nevertheless it suffers from a lack of standardization and understanding [14] and is not suitable for all area. It is most useful where diffuse light prevails and when the environment provides good albedo (snow, light sand...).

In single junction cells, thermalisation is the main cause of energy loss. Photons with higher energy than the semiconductor bandgap creates electron-holes pairs which relax via kinetic energy transfer to the material lattice. Figure 1.8 illustrates well the inner battle occurring while designing single junction cells: huge loss of absorption while increasing the bandgap or better absorption with lower bandgap at the price of more thermalisation.

Stacking multiple junctions provides an effective solution to this issue (see Figure 1.9). Increasing the number of junctions in a cell allows to increase absorption and reduce thermalisation losses. Carefully choosing the bandgaps combination in the Multijunction solar cell provides significant enhancement of the photoconversion. 38.8% was attained with a 5 junction solar cells [15], 37.9% with three junctions [16]. Multijunctions cells usually consist in single junction cells assembled in series and connected with tunnel junctions. One drawback of this design is that the cell with the lowest output current limits the whole device current. Careful choice of the sub-cells material and thickness is needed in order to provide lattice match between the layers and current matching between cells.

Multijunction (MJ) cells are made of III-V semiconductors and are therefore expensive. Thus they are used for space applications which are less concerned by cost issues and where III-V's resistance to radiation damages is a major advantage [17].

To solve this issue for terrestrial application, concentration emerged as a method to build competitive systems out of these Multijunctions cells. Using an optical systems to concentrate light on cells of reduced area, 46% efficiency was reached at 518 suns [18] and 38.9% efficient modules with a concentration of 333 suns [19] were built. The design consists in an optical system focusing the light the MJ cells with mirrors or Fresnel lenses. Since only direct light is focused properly and because the system has a finite acceptance angle, the modules are mounted on trackers that change their orientations according to the sun position [20, 21]. If it is believed that CPV can be competitive with Si flat panels [22] , the CPV installed capacity has decreased from

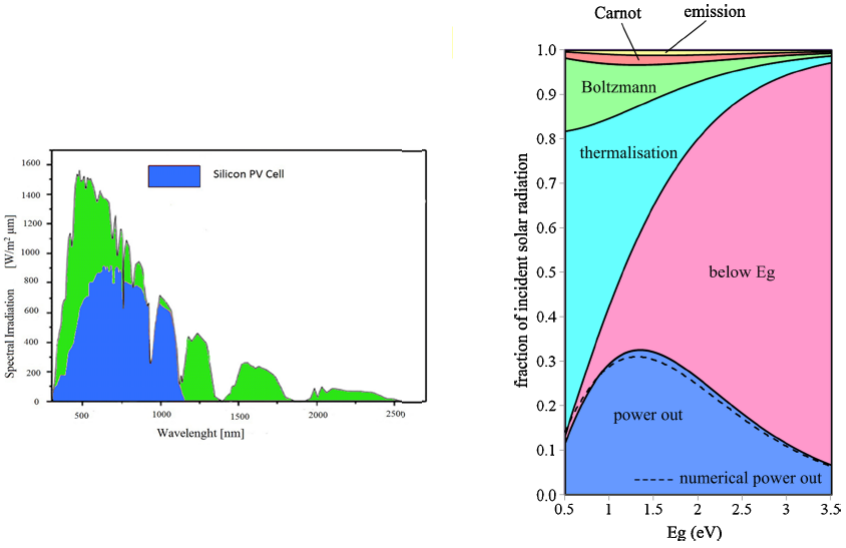

(a) (b)

Figure 1.8: Single junction limitations. a) In blue the power converted by a Si cell from the sun spectral irradiance. b) Distribution of the different losses depending on the single junction bandgap Eg. From [11].

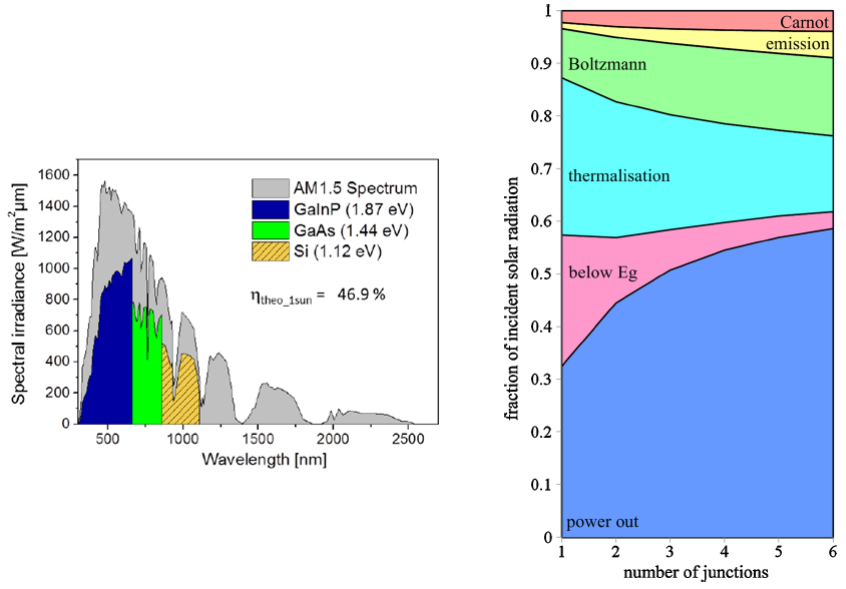

(a) (b)

Figure 1.9: Interest of Multijunction solar cells. a) Power converted by a three junctions solar cell from the sun spectral irradiance. b) Evolution of the losses distribution with increasing number of junctions. From [11]

more than 120 MW in 2012 to about 10 MW in 2016. Several reasons like the need of high Direct Normal Irradiance area (meaning areas with less diffuse light), the optics sensitivity causing additional maintenance due to soiling or tracker system may have caused this lack of enthusiasm from the market. Thus limited market and deficit of standardization and feedback from CPV installations are currently limiting the growth of this technology.

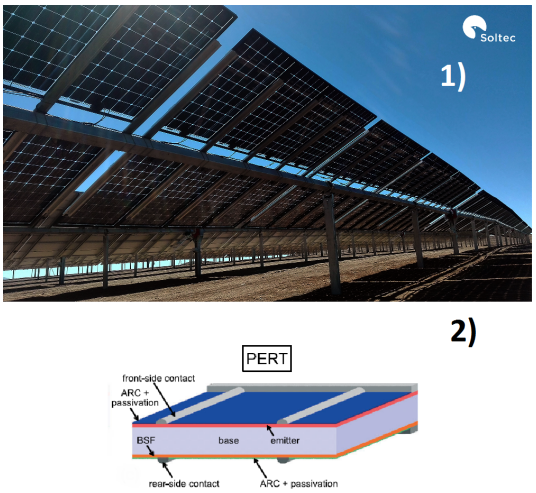

(a) From [23, 13]

(b) From [21]

Figure 1.10: a) 1) Image of a Bi-facial modules plant 2) Scheme of a modified PERT bi-facial cell. b) Concentrated solar cell module and schema of usual design of concentrator cells.

1.4 The tandem design compromise

1.4.1 Tandem solar cells a promising path

In addition to the technical issues evoked for the different technologies, economic stakes are major in the photovoltaics industry. Silicon industry has driven the prices so low that all emerging new technologies have lost market shares in the recent years. As an example CIGS and CdTe accounted for 17% of the market in 2009 and only 5% in 2017 [3]. Even Si companies suffer from those tough price competition and need to decrease their modules $/W costs. Material related costs have been dramatically reduced already, companies have to increase the power production of PV modules through efficiency increase.

This is why tandem solar cell is a promising solution. Here we will consider that tandem cells consist in "two junctions cells" assembled with two "single junction cells". Tandem using Si bottom is a compromise between the Multijunction cells, with high efficiency but costly, and Si cells. It allows to increase the PV efficiency using already a mature technology for the bottom cell.

However tandem cells will be successful only if the top cell offers 20% efficiency and a good coupling with the Si cell. It must also have long durability to ensure a 25 years warranty for modules. All at acceptable cost, meaning that the module cost must remain low in comparison to the costs due to all of the other components associated to the photovoltaic installation, the so called Balance of System (BOS) costs [24].

For tandem with a Si-based cell, two types of materials arise interest in the photovoltaic community, the perovskite and the III-V semiconductors. Perovskites are a promising materials in PV, much research effort is currently ongoing. Despite some non-compatibility between perovskite cells process and Si bottom cell, adjustment can be made and good efficiency attained. [25, 26]. However perovskites suffer from an instability that is not compatible with a 25 years modules lifetime for now [27].

III-V cells are more mature and provide sufficient efficiency and durability already. But they are too costly. With the current costs of III-V cells, a tandem comprising III-V and Si sub-cells would only be competitive for area limited application (residential PV) where the "areal" BOS cost of such installation is high [28]. The main cost of III-V cells is the growth substrate, accounting for more than 80% of the process expenses [29]. Methods allow to reduce this cost, epitaxial lift off (ELO) [30] is particularly interesting as it permit to remove the cells from the growth substrate and reuse it for other growth after treatment [31, 32]. Providing that substrate recycling can be repeated multiple times without reduction of the cell quality, III-V/Si tandems might be competitive for all applications.

1.4.2 Possible architectures and associated requirements

Three types of tandem cells configurations exist, corresponding to the number of connections needed to wire the cell in a module.

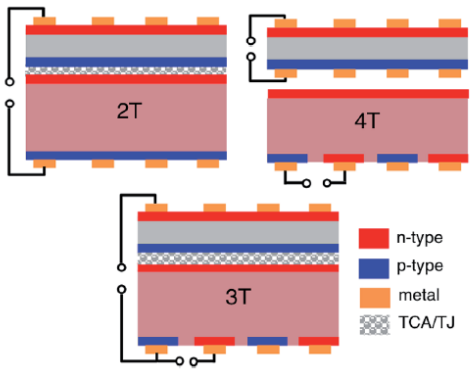

Figure 1.11: Different tandem cell architectures possible [27].

The 2 terminals (2T) cells, have only two connections and thus can be integrated in the module like usual single junctions cells. The sub-cells are assembled in series, thus the tandem has a higher Voc than single junction cells (sum of sub-cells voltages) and the same current passes through all sub-cells. In other words

the sub-cell with lowest current generation limits all the device's current. This means that the structures of the cell have to be optimized to ensure current matching between the sub-cells. The connection of the cells requires a tunnel junction. This configuration also needs the use of demanding bonding process or top cell fabrication (epitaxy methods detailed later on). Although, it has been the strategy chosen by Fraunhofer ISE that developed performant 2T cells. They currently hold the **three junctions** tandem cells efficiency record with a GaInP/GaAs//Si cell with 33,3% efficiency under one sun [33]. With a perovskite top cell, a 25.2% efficient textured tandem was fabricated with monolithic perovskite deposition on Si[26] .

In the 4 terminals (4T) version each sub-cell has its own contacts. The two cells are operated independently, the top cell acts as a light filter for the bottom cell. The efficiency of the tandem cell is simply the sum of the two sub-cells efficiency. This design gives less constrain on the sub-cells design and assembly but the modules have to be adjusted as the cells wiring changes in comparison to usual modules composed of single junction cells. Best **dual junctions** tandem cells reported are 4T cells with GaAs/Si cell at 32.82% and GaInP/Si cell at 32.45% [34]. This technique has the advantage of allowing to process the sub-cells separately, stacking can be the last process step indeed.

Third possibility is the 3 terminal configuration were the sub-cells share one of the contact. It permits to operate sub-cells at maximum power point. It is most interesting in a configuration where the bottom cell is an interdigitated back contact Si cell [35, 36].

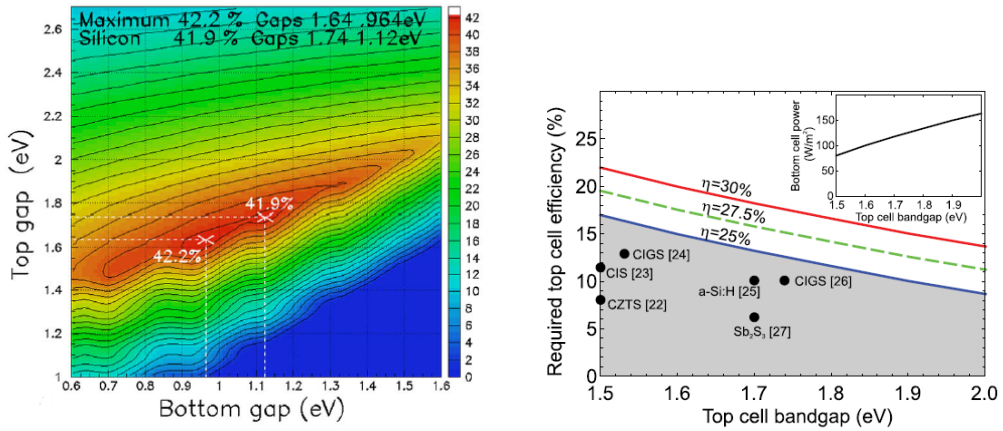

(a) (b)

Figure 1.12: a) Theoretical efficiency limits for tandem cells depending on sub-cells bandgap [37]. b) Influence of the top cell bandgap on its required efficiency to assemble Si based tandem cell with 30% efficiency in red, 27.5% in green and 25% in blue [38].

Connoly et al calculated the maximum tandem theoretical efficiency as a function of the sub-cell bandgaps [37]. Figure 1.12 shows that, assuming ideal conversion for each sub-cells, the best bandgap combination is a 1.74 eV top cell associated to a 0.96 eV bottom cell, efficiency of 42.2% could be achievable. Fixing the bottom cell bandgap at 1.12 eV (Si bandgap value) efficiency of 41.9% is achievable. We now understand why high bandgap III-V semiconductor are of interest for tandem application. Nevertheless no III-V semiconductor offers this bandgap value and the lattice match to Si. Lattice match is an important condition to preserve good electronic properties in the semiconductor. 1.74 eV ideal bandgap is possible with an AlGaAs alloy cell. GaInP with slightly higher bandgap can theoretically provide cells with about 35% efficiency. Thus, various methods have been developed to integrate those alloys on Silicon.

White et al explained the top cells requirements in order to assemble performant tandems with a Si bottom cell. Fixing an efficiency goal for the tandem cell, they calculated the top cell efficiency need depending its gap [38]. If we aim for a 30% tandem solar cell, a top cell with Eg~1.74 eV must provide around 20% efficiency (see Figure 1.12 b)).

1.4.3 III-V cells integration on Silicon

As developed earlier, tandem solar cells are of interest for the improvement of the efficiency of PV cells, especially III-V based tandem cells that currently give better yield and durability. Though, the integration of the III-V alloys of interest on Si is not trivial. In this section, we will describe the different methods to address this challenge.

The lattice difference challenge

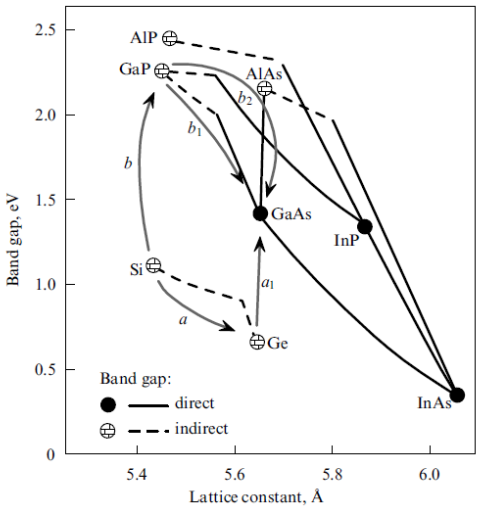

Figure 1.13: Lattice parameters and Bandgap of Si, Ge and III-V semiconductors. AlGaAs alloys have lattice constants close to GaAs, GaInP is lattice matched to GaAs at one composition. Direct growth of III-V on Si requires the use of buffer layers, based on GaP alloy (path b on the graph) or SiGe (path a).

This problem is related to lattice differences. Silicon has a 0.543 nm, which does not correspond to any of the lattice parameters of III-V compounds of interest (Figure 1.13). Growth of III-Vs on Si has a long history and yet, no ideal solution has been proposed to solve all the underlying difficulties: lattice-mismatch, polar on non-polar interface, thermal expansion coefficient mismatch. Considering just the lattice-mismatch issue, coherent epitaxy of planar layers can only be obtained for relatively small lattice-mismatch (typically < 1 %) and layer thickness below a critical value. Above this critical thickness, the layer relaxes the accumulated strain energy by creating dislocations, in order to lower the total energy of the system.

Threading dislocations are detrimental for the optoelectronic properties of the layer as they act as recombination centers for the charge carriers. This phenomenon is amplified by the difference of thermal expansion of the material. As an example GaAs has a lattice constant of 0.565 nm, which leads to a 4% difference with Si lattice at room temperature. With expansion coefficient of $5.73.10^{-6\circ}C^{-1}$ for GaAs and $2.6.10^{-6\circ}C^{-1}$ for Si, this difference raises to 18% at MBE growth temperature.

Direct growth of III-V on Si:

In order to improve the quality of mismatched layers, 2 µm thick buffers and thermal cycle annealing (TCA) were used. The dislocation density in the active III-V layers was reduced and a 16.6% efficiency for a GaAs cell under AM1.5G illumination was obtained[39]. Note that the whole structure (cell and buffer) was 6 µm thick and that complete elimination of dislocations was not possible. Indeed, the same structure grown on GaAs have a 24.7% efficiency and its carrier diffusion length is around twenty times the diffusion length measured for the cell grown on Si substrate. Dislocation filter layer (complex superlattice succession) and TCA were also used to grow AlGaAs cells on Si [40].

Other type of buffers consists in graded layers to change the lattice constant progressively. Figure 1.13 highlights the paths from the Si lattice parameter to the one of GaAs. Either SiGe alloys can be used or the

growth can start with GaP and continue with GaAsP alloys to finish with the growth of GaAs. With a SiGe graded buffer, a GaAs cell with 18.1% efficiency was obtained on a Si substrate [41].

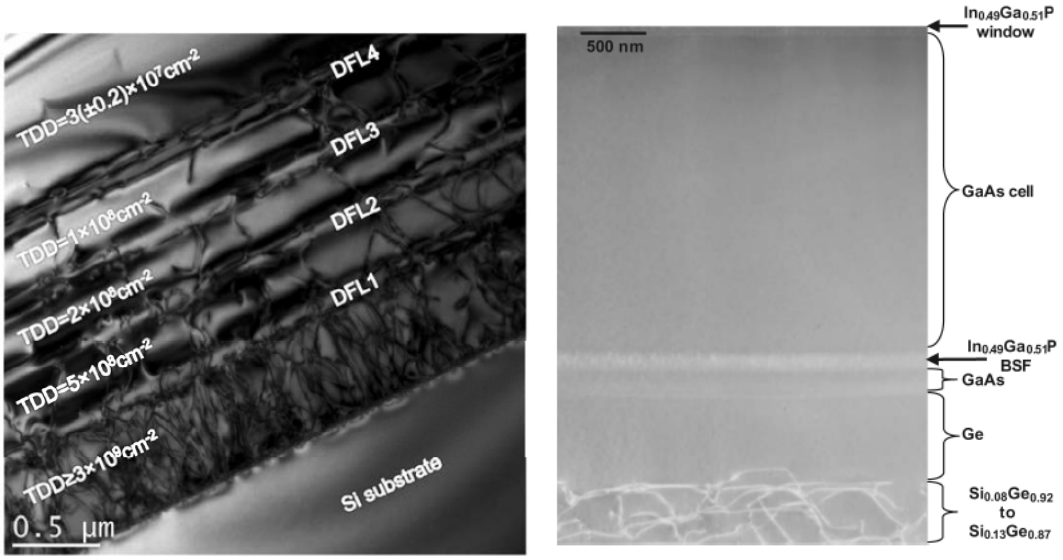

(a) (b)

Figure 1.14: a) TEM image showing how the dislocation filters and TCA allowed to reduce the dislocation density before the active layer [40]. b) TEM image of GaAs cell grown on Si using a SiGe buffer. [41].

If those methods offer convenient solution for III-V integration on Si, they are not compatible with a tandem use. Indeed these thick buffer layers are not transparent to the spectrum absorbed by the Si and their growth represents an additional cost. They would cause a significant parasitic absorption that reduces the photocurrent of the Si bottom cell.

Another solution is the use of nanowires which solve the lattice difference issue[42]. Indeed, with their geometry the strain is elastically relaxed at the nanowire free surfaces. But their growth is complex and requires patterned substrate, a process that is for now hard to imagine at industrial scale. Finally another interesting solution is to reverse the process and grow the Si on the III-Vs, taking advantage of the lower growth temperature enabled in plasma enhanced chemical vapor deposition (PECVD) [43].

Remote growth and bonding:

A more rational method is to grow the III-V cell on a GaAs substrate and to bond it onto the Si sub-cell in a second step. The active III-V layers can be separated from their GaAs substrate by an epitaxial lift-off (ELO) and the substrate can be used again. This approach can be cost effective and the lattice matching issues are avoided.

For this wafer bonding method, the surfaces of the two samples to be bonded are brought into contact under specific conditions: high vacuum, low mechanical pressure applied, the process sometimes also includes plasma treatment [44]. A thin amorphous layer forms at the interface, ensuring the permanent bonding of the two pieces while allowing conduction from one cell to the other. This method requires smooth interfaces and is really sensitive to the sample roughness or the presence of impurities. A roughness root means square as small as 1 nm can cause voids between the samples, which is of course detrimental for the tandem solar cell[45].

All the methods listed above are used to fabricate 2T tandem cells. Mechanical stacking is another bonding method that permits the assembly of 4T tandems. The cells are stuck with an epoxy glue on each side of a glass slide. The bonding resist has to be transparent, and the alignment of the top cell contacts with the front contacts of the bottom cell is important to minimize cell shading. The major advantage of this method is that the two cells can be processed separately. Moreover there is no constrain on the surfaces

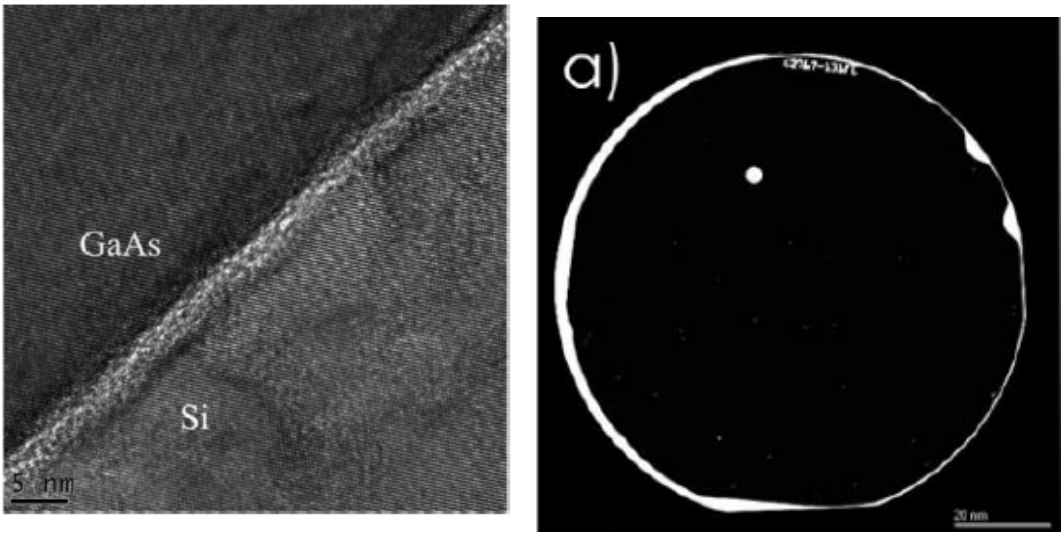

(a) (b)

Figure 1.15: a) High definition TEM image of the interface of wafer bonded III-V cell on Silicon cell [44]. b) Scanning Acoustic Microscopy image of III-V cell bonded on Si. Black area are properly bonded, white areas are voids due to surface contamination. [46].

morphology, which can be textured since it will be planarized by the bonding resist. Thus no specific design for the Si cell is required (besides the sizing) and any of the current market Si technologies are suitable for this kind of tandem.

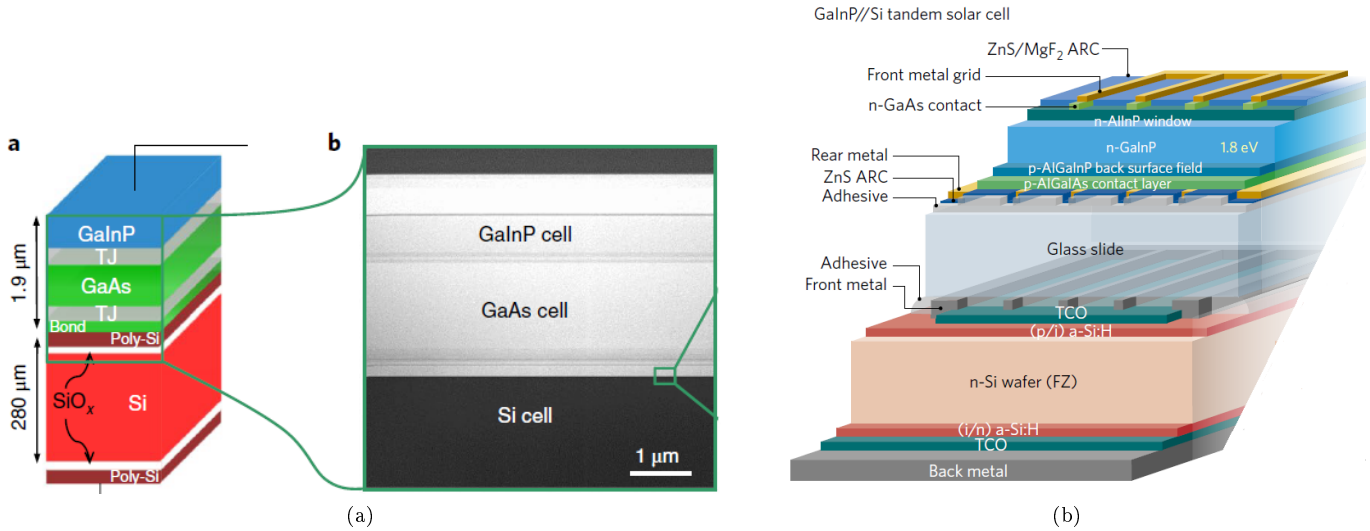

(a) (b)

Figure 1.16: Illustration of two possible bonding methods. a) Scheme and TEM image of the record 3 junction wafer bonded cell [33] b) Architecture of a mechanically stacked tandem cell. [47]

1.5 Aim of the thesis

This doctoral work aims to progress on the elaboration of tandem solar cells combining III-V and Silicon. This objective is part of the task of partner *Total* in the "Institut Photovoltaique d'Ile de France" (IPVF) among other problematics linked to PV. More precisely, the thesis focuses on the elaboration of a III-V top cell.

1.5.1 Choice of the top cell architecture

For this kind of project, the type of architecture chosen for the top cell determines many constraints on the task to be addressed. Our work is conditioned by the choice of a 4T design. This configuration does not request the complex equipment needed for wafer bonding and gives more flexibility on the Si cell design. As mentioned earlier, this method allows one to process the two cells separately. Therefore, we plan to collaborate with another IPVF's project that focuses on Si cells fabrication.

Regarding the choice of the material, the ideal bandgap combination with Si request a high bandgap III-V alloy. If GaAs is currently the most performant III-V alloy for PV application, its 1.42 eV bandgap limits the maximum theoretical efficiency of a tandem cell with Si. As an example, despite its 28.8 % efficiency in single junction configuration (7% more that best GaInP cell), the best GaAs and GaInP tandem cells with Silicon have almost identical efficiencies. [34]

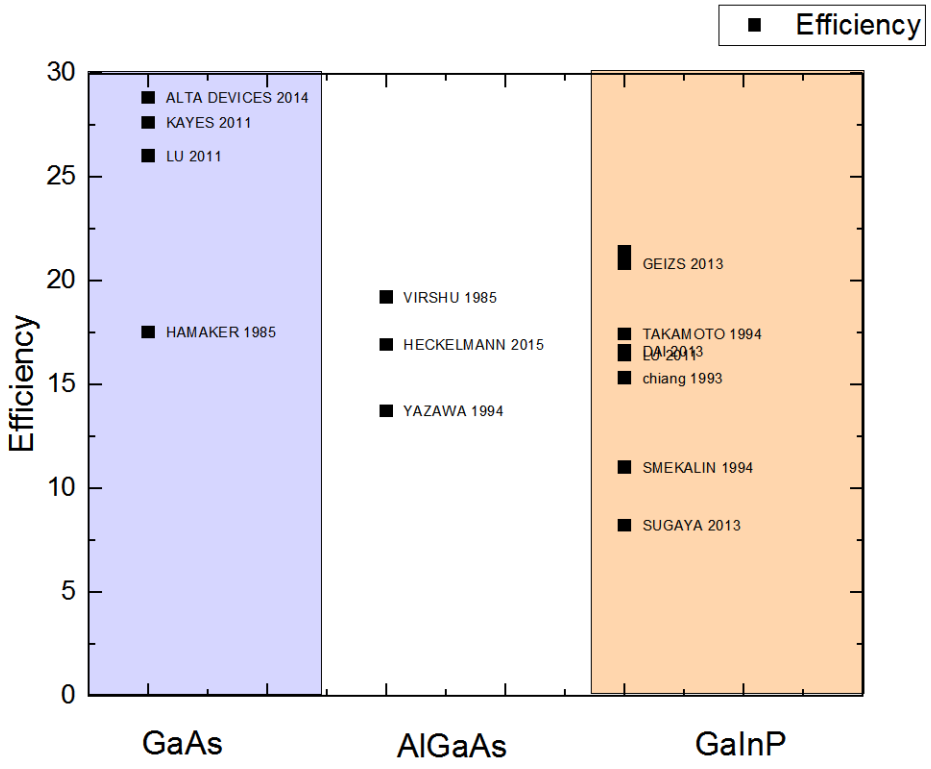

Figure 1.17: Notable cells results for GaAs, AlGaAs and GaInP.

Then the AlGaAs alloy, with a 1,74 eV bandgap and which has a good lattice match to GaAs growth substrates, is an interesting candidate. However it has been observed that its sensitivity to oxygen and its tendency to oxidize limit the performance of the AlGaAs compound.

Therefore the goal of this work is to elaborate performant GaInP top cells. This alloy is less sensitive

to oxidation and the previous research studies on the GaInP cell have proved that good efficiencies can be obtained with this III-V ternary.

Note that this work compose the first work package of IPVF's Projet E. Other solutions for the elaboration of a III-V/ Si tandem cell are explored in the two other work packages of the project. Direct growth of nanowire cell on Si in the second work package and elaboration of low-cost growth substrate in the work package three.

1.5.2 Plan of the manuscript

This manuscript will detail the different building blocks that were addressed during this PhD.

In Chapter 2, we will detail the optimization and calibration of the growth of the phosphide alloys composing our top cell. We will explain the specificities of GaInP epitaxy using molecular beam epitaxy (MBE), we will highlight how the growth conditions impact its physical properties, then we will study the doping of phosphides and how their composition influence the doping efficiency.

Chapter 3 will focus on the top cell structure and its impact on the conversion efficiency. We will explain the role of each layer and illustrate the improvements provided by their optimization. Later, we will emphasize the limitations identified in the cells. We will also detail additional work on the bonding and transfer of the cells.

Finally in Chapter 4, the aspect limiting the cell performance will be further investigated. With material characterization on p-doped GaInP we will highlight precisely the factors limiting the solar base quality. We will propose a solution to improve GaInP alloy and show a practical solution that leads to satisfying photoconversion efficiency. Finally we will develop improvements on the top cell process that aim to facilitate the top cell contacting and bonding.

Chapter 2

MBE growth of III-V alloys

2.1 Choice of the growth method

III-V cells are grown with two methods metalorganic vapor phase epitaxy (MOVPE) and molecular beam epitaxy (MBE). MBE involves physical processes such as adsorption, surface diffusion, desorption and incorporation of simple molecular or atomic species on the substrate surface while MOVPE is based on more complex precursors which involve many chemical reactions before incorporation of the constituents in the solid.

With MOVPE, the III-V elements (Ga, Al, In, As, P) are contained in gaseous precursors. The precursors are injected in the growth reactor, where they reach the surface of the heated growth substrate. At growth temperatures superior to 600°C, the gas precursors decompose at the substrate surface and the III and V species react with the solid III-V surface. The composition of epitaxial layers is adjusted with the precursor pressure in the reactor and the temperature. MOVPE is performed at relatively high pressure (several Torrs) while MBE is a ultra-high vacuum method. In MBE the elements of interest are produced from ultra-pure elemental solid sources. They are placed in crucibles, during the growth the crucibles are heated so that the elements evaporate and impinge on the growth substrate.

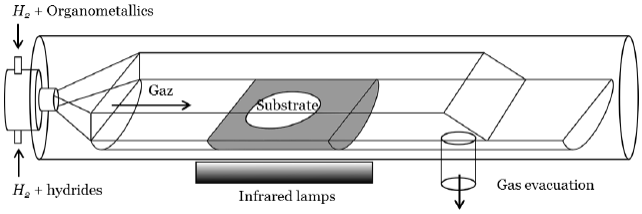

Figure 2.1: Sketch of a MOVPE reactor.

Over the years, GaInP cells grown with both of those method were reported. MOVPE cells perform better than cells grown with MBE, with a record photoconversion efficiency of 20.8% [48]. MBE method led to scattered results with best cell at 16.6% efficiency [49].

MOVPE benefited from much interest in the 90's. It was developed for industrial purposes, research on LEDs, lasers and solar cells applications. This allowed to enhance the optoelectronic properties of the semiconductor grown by this method. MBE is currently regaining interest as the solid sources gain in purity.

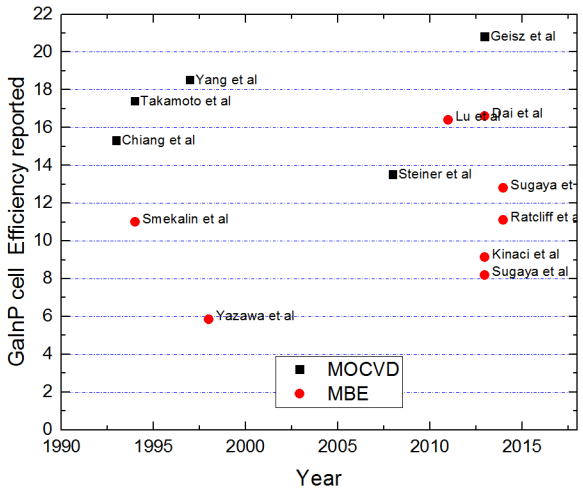

Figure 2.2: Photoconversion efficiencies reported for GaInP single junction solar cells. In black cells grown with MOVPE, in red MBE grown cells.

Generally, MOVPE offers the possibility to reach better production yield than MBE. But it operates with dangerous gas precursors, such as arsine (AsH3) and phosphine (PH3). Once used for the growth, the gas are pumped and toxic substances are trapped in adsorbers before purified for release for release. MBE offers more safety because the sources are confined in the vacuum chamber. The risk for lethal gas release is limited to rare maintenance operations.

For those safety reasons IPVF chose the MBE method. This choice is also compatible with another work package of IPVF project based on nanowires for which the C2N laboratory has a strong know-how.

2.2 The Molecular Beam Epitaxy technique

2.2.1 Definition of Epitaxy

Epitaxy refers to the coherent deposition of crystalline material on top of a crystalline substrate. To be labeled "epitaxy", a method has to enable the growth of single crystal layers on top of a chosen substrate. The choice of the substrate is essential. In most cases, alloys of similar crystalline structures and similar lattice characteristics can be properly grown on top of it.

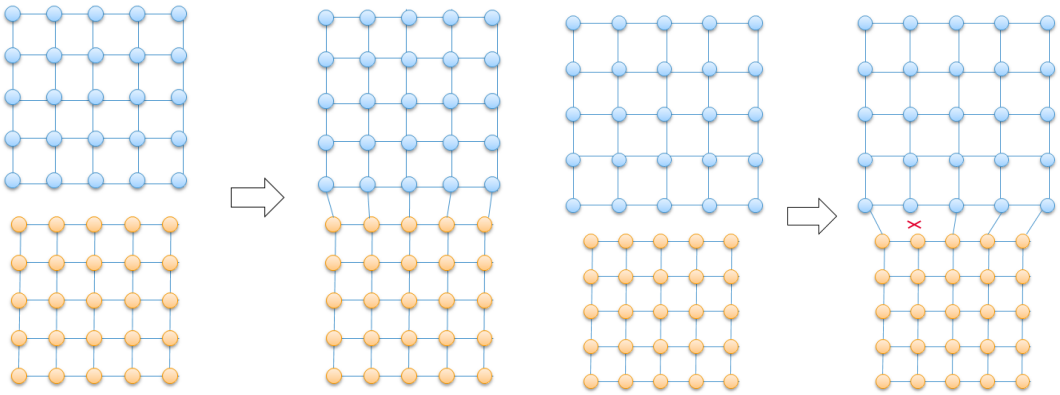

(a) strained (b) relaxed through dislocation

Figure 2.3: Sketch of the assembly of materials with different lattice parameters. a) layer grown strained on substrate b) apparition of dislocation due too important lattice mismatch.

Every alloy has a specific lattice parameter, arising from the atomic size and the structural arrangement of the lattice. When an alloy is deposited on a substrate with a different lattice parameter, strain energy accumulates in this epilayer. Above a critical thickness, the strain is relaxed plastically by strain generation of interfacial dislocations which can propagate in the epilayer. Figure 1.13 in Chapter 1 highlights that it is a challenging constraint and that only few alloys are compatible with each other. These dislocations act as carrier recombination centers which are detrimental for the photovoltaic conversion efficiency. In his thesis Romain Cariou illustrated the impact of the threading dislocation density on the property of a GaAs solar cell [50]. Below a 2 µm spacing between dislocations, the diffusion length of carriers reduces and causes the open circuit voltage Voc to decrease as well.

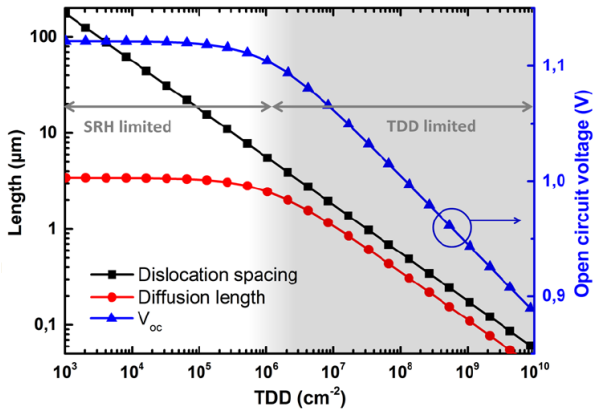

Figure 2.4: Effect of Threading dislocation density on the dislocation spacing in black, the diffusion length of minority carriers in red and the cell's Voc in blue. From [50] calculated using [51, 52]

As a reminder, we exposed in Chapter 1 several methods which can reduce the dislocation concentration in mismatched solar cells. Onno et al [40] reported AlGaAs cells grown on Si with a conversion efficiency of 3.64%, due to the dislocations present in the AlGaAs.

When the lattice mismatch is small enough to avoid the formation of misfit dislocations, remarkable material quality can be achieved by epitaxial growth. Many applications have benefited from the development of epitaxial techniques. In particular, MBE is very popular for HEMT and HBT transistors [53]; and other applications such as quantum well lasers and diodes [54], single photon sources [55]...

2.2.2 Modern MBE set-up

During this PhD two identical MBE machines were used for the growth, they are RIBER Compact 21 models. First half of my PhD work was performed with the C2N machine, second half in the IPVF machine which is fully dedicated to Project E experiments. In this section, the configuration of the tool is briefly explained.

The most important part of a MBE machine is the growth chamber, schematically shown in Figure 2.5. In this chamber, many elements insure appropriate growth conditions and in-situ monitoring. It is made of stainless steel and remains under ultra high vacuum (UHV). A combination of pumps (cryogenic, ionic and turbo molecular pumps) maintains a vacuum of 10^{-10} Torr (1 Torr=1.3 mbar=$1.3.10^2$ Pa).

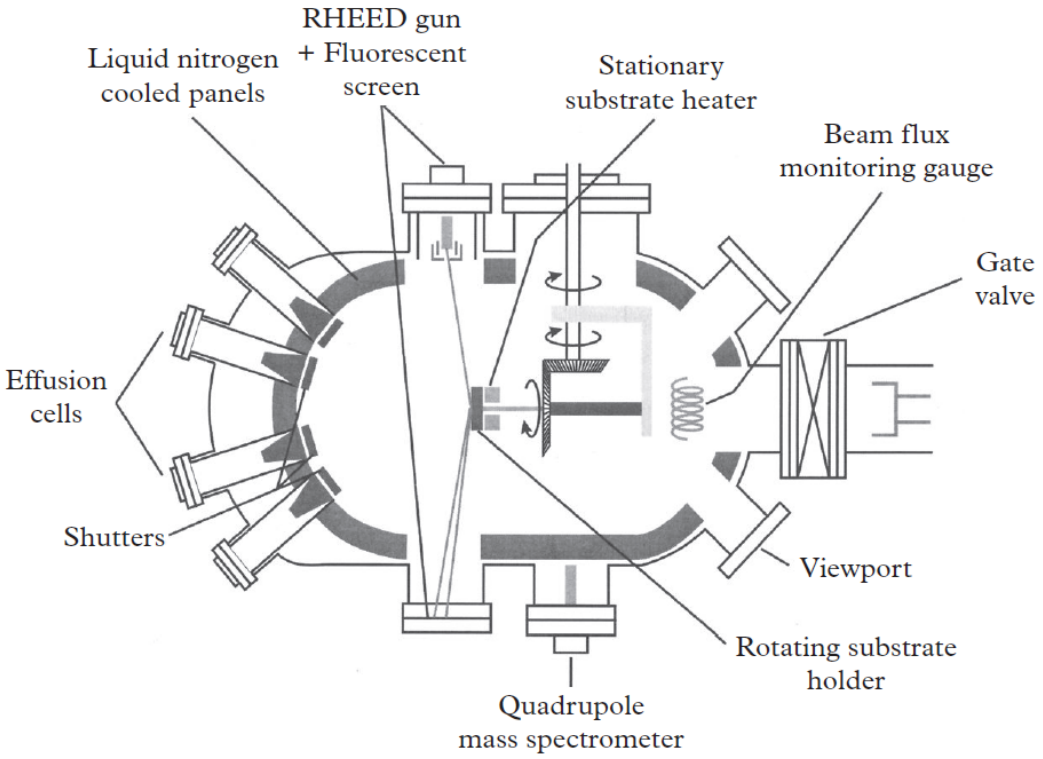

Figure 2.5: Sketch of the growth chamber of an MBE machine. From [56]

The material sources are effusion cells for elements III and dopants, and cracker cells for elements V (phosphorus and arsenic). In the effusion cell, a pure material source is placed in a crucible. It is heated so that the source material can melt and the elemental vapor pressure produces a molecular beam flux in the high vacuum environment. Because of the UHV the beam elements propagate without collision to the growth substrate. Temperature control of the effusion cells is a crucial aspect as it determines the beam pressure. A shutter allows to control the aperture of each effusion cell and therefore the elemental beam flux can be stopped at will. In this work we use **Ga**, **In**, **Al**, **P** and **As** for the semiconductor alloy growth and **Be** and **Si** for doping purposes.

The growth substrate is placed on a rotating holder, comprising a heating filament that brings the substrate to the growth temperatures (typically 500 to 600 °C). A cryo-panel cooled by liquid nitrogen surrounds the substrate holder and the top of the effusion cells for thermal insulation and further pumping by trapping the residual gas species.

As UHV is essential to prevent the oxidation of the material sources and minimize the presence of impurities in the growth chamber, a load-lock chamber and an outgassing chamber permit the introduction and preparation of new substrates without exposing the growth chamber to the atmosphere.

Other major components are in-situ calibrations tools. An ionic gauge enables the measurement of the beam equivalent pressure produced by each effusion cell and to calibrate the atomic or molecular fluxes impinging on the growth substrate. Then the Reflection high energy electron diffraction (RHEED) allows to directly measure in real time the surface reconstruction and the surface morphology of the growing sample. It consists of an electron beam which has a grazing incidence on the substrate. The diffraction pattern is observed on a phosphorescent screen. The aspect of the diffraction pattern is characteristic of the surface roughness, a streaky pattern refers to a smooth surface while a spotty pattern corresponds to a rough surface (see Figure 2.6). RHEED is really useful to follow the substrate deoxidation before growth and then to evaluate in-situ the growth front.

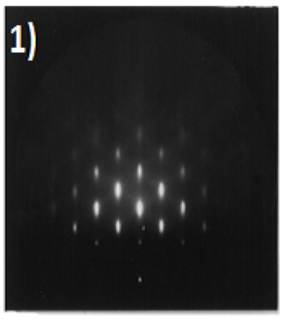

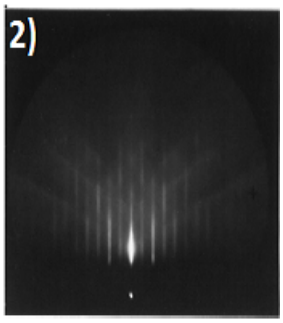

(a)

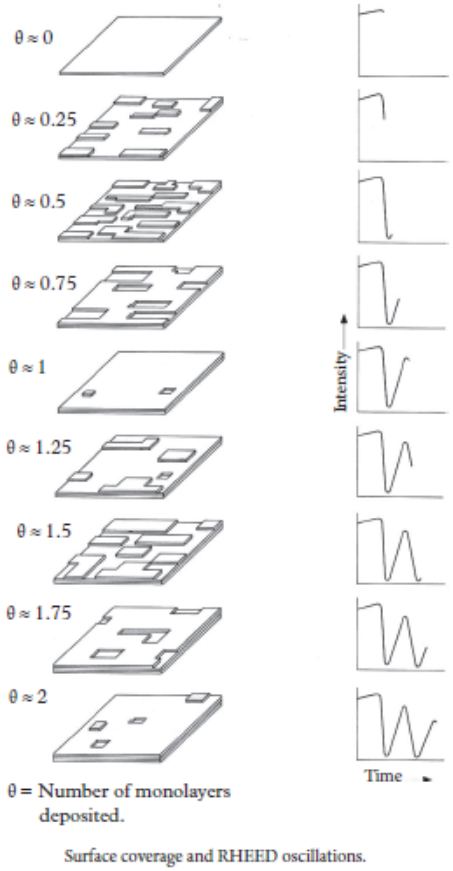

(b) From [56]

Figure 2.6: Details on the use of RHEED for growth assessment. a) RHEED diffraction pattern of a rough surface in 1) and smooth surface in 2) from [57]. b) Use of RHEED oscillations for growth rate calibration, how the sample surface changes the RHEED streaks intensity.

When growth occurs by island formation and extension, the intensity of the streaks of the RHEED pattern

varies in time. In certain conditions, the growth of a monolayer starts with the formation of small islands. The adsorbed atoms then diffuse on the sample surface, until they reach an "island step" allowing the islands to grow and to coalesce to form a full monolayer. This process replicates for the formation of the next monolayer. The streak intensity is maximum when a monolayer is completed and minimum for half layers (Figure 2.6). The operator can then measure the growth speed in $monolayer.s^{-1}$. Growing binary alloys in element V excess (GaAs and AlAs for example), the growth speed is dictated by the element III. One can calibrate the deposition rate associated with each group III elements. Then, supplying simultaneously the two group III elements, one can control the ternary alloy composition, AlGaAs in this case.

2.3 GaInP particularities

Contrary to AlGaAs, there is a very limited range of GaInP compositions which can be grown on GaAs with a reasonably low lattice mismatch. At the lattice-match condition, the composition is 51.6% of Ga and 48.4% of In. Nevertheless GaInP presents some specific arrangements, referred to as ordering effects, that influence its properties, in particular its bandgap. Controlling these effects is another degree of freedom to adjust the GaInP properties for the desired use.

Like GaAs, GaInP assembles in zinc-blende configuration (see Figure 2.7). The group III elements (Ga and In) randomly occupy the cation sites in the zinc-blende lattice. This normal arrangement is called disordered as the distribution of group III elements is random.

2.3.1 Ordering effects

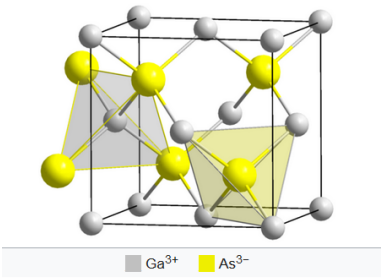

(a) [58]

Figure 2.7: The zinc-blende structure a) for GaAs, grey spheres are group III elements sites, yellow spheres are for group V.

Ordering is a well-documented mechanism that provokes a specific arrangement of the phosphide ternaries. More common with MOVPE growth, it consists in a superlattice-like assembly of Ga-rich and In-rich planes. For the ordered alloy, the Ga and In distribution is no longer random, the two species tend to incorporate in distinct and consecutive atomic planes. Figure 2.7 shows, the difference between a disordered alloy and an alloy presenting ordering.

This effect can be more or less pronounced. In other words, different degrees of ordering are possible and correspond to the importance of the segregation of Ga and In.

As evoked earlier, ordering influences the bandgap of the alloy: thus values from 2 eV to 1.83 eV were reported for GaInP lattice matched to GaAs[59, 60]. The gap decreases with the degree of ordering as the structure resembles a superlattice. It was also noted that ordering degrades the electrical properties of GaInP, due to the presence of traps at the limit of ordered and disordered domains, and therefore reduces solar cell efficiencies [61, 62, 63].

Ordering degree is affected by the growth conditions. In MOVPE, high growth temperatures (Tg$>$ 700°C) inhibit ordering while lower temperatures tend to favor it. Figure 2.8 illustrates the impact of the growth temperature on the ordering of AlInP. In this case, active and cladding layers are of same alloy the difference of bandgap due to ordering permits the confinement of the carriers in the active layer. Miscut of the GaAs substrate surface also impacts ordering, it increases with a misorientation toward [-110] [66]. Finally the V/III ratio is another lever to tune the degree of ordering. Figure 2.8 summarizes the influence of V/III ratio and growth temperature on the bandgap change related to the degree of ordering.

With MBE growth, V/III ratio diminution and decrease of growth temperature promotes ordering [63, 67]. Ordering effects are less pronounced with MBE since the lowest bandgaps reported are above 1.86 eV, against 1.83 eV for MOVPE growth.

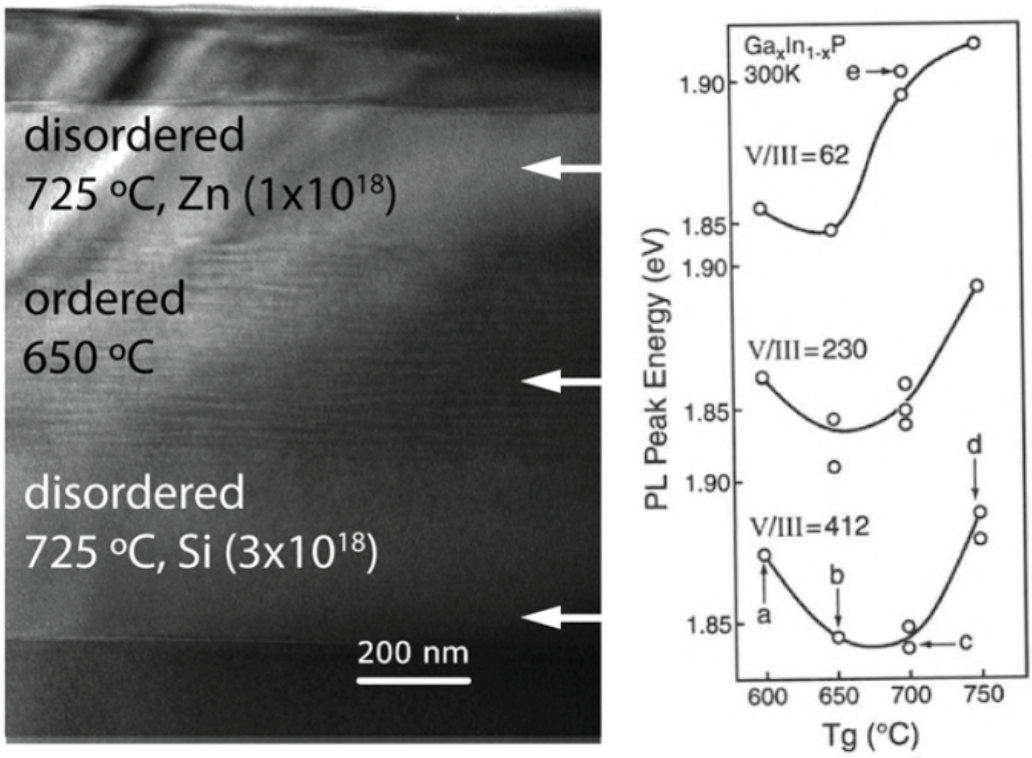

(a) From [64] (b) From [65]

Figure 2.8: a) Tg influence on AlInP ordering. STEM image of a LED structure, area grown at 650°C exhibits a layered contrast revealing the ordering. b) Effect of the MOVPE growth conditions on GaInP bandgap.

2.3.2 Lateral composition modulation

Another type of structured inhomogeneity is possible in GaInP alloy, the so-called lateral composition modulation (LCM), that is a sort of horizontal ordering. It consists of a similar layered pattern of Ga rich and In rich bands, although the bands are perpendicular to the (001) growth axis. With LCM the modulation period is larger than with the previous ordering effect, 10-50 nm period for LCM while the period of vertical ordering corresponds to the thickness of a few atomic planes of the order of 1 nm. Figure 2.9 shows three examples of LCM occurring in GaInP samples.

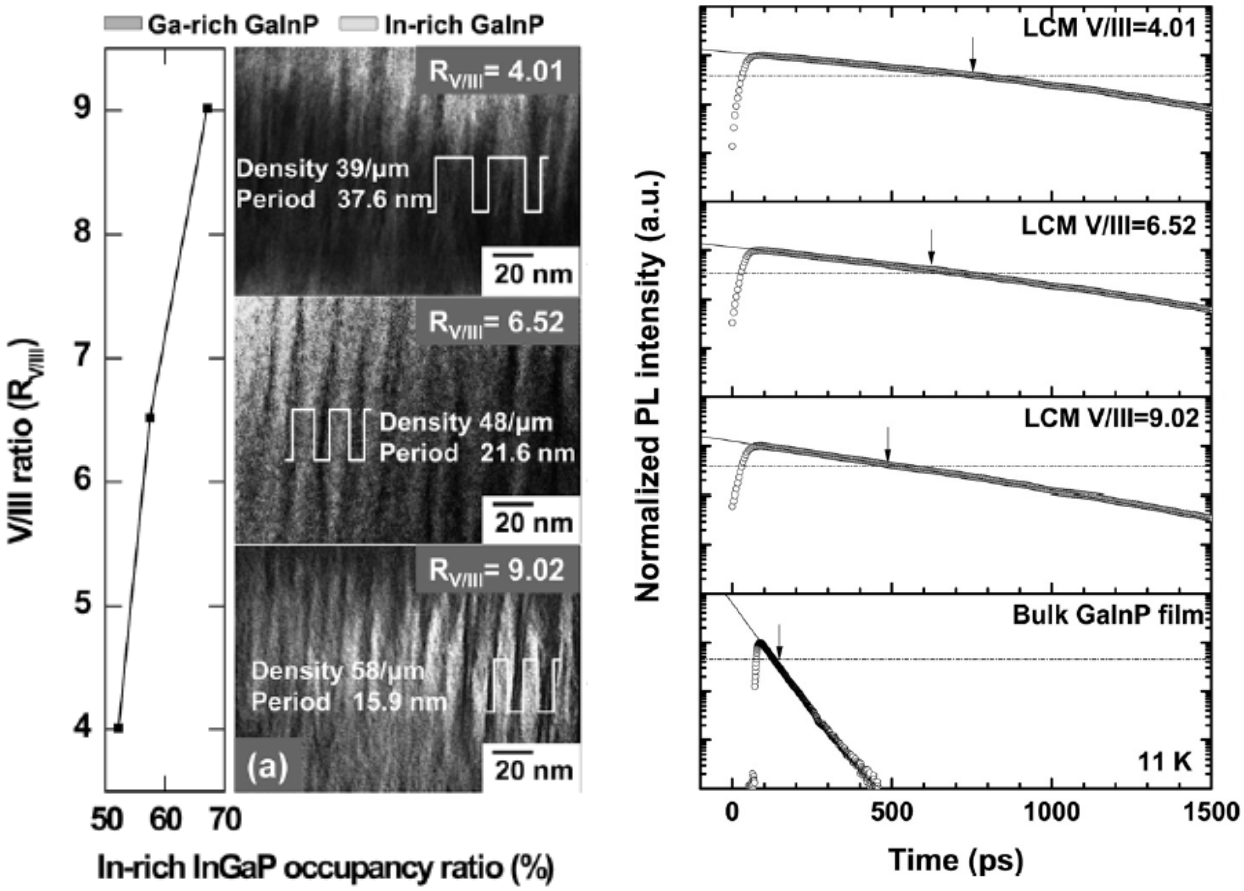

(a) From [68]

(b) From [69]

Figure 2.9: Illustration of the V/III ratio influence on the LCM properties. a) Increase of the modulation width when the III/V ratio is reduced, In rich bands occupy more space when modulation period increases. b) Carrier lifetime decrease with the LCM width (ie) while increasing V/III ratio.

The reported GaInP layers presenting LCM result from the growth of short period of GaP/InP superlattices. It is believed that the strain between the superlattice layers and differences in the surface diffusivity of the species provoke the diffusion of the elements the formation a ternary layer presenting LCM[70]. Moreover Dorin et al suggest that a layer by layer growth regime results in an homogeneous growth while 3D island growth regime implies the apparition of LCM [71].

Like ordering, LCM is influenced by the growth temperature and the V/III ratio. Figure 2.9 a) shows that reducing the V/III ratio increases the modulation width [68]. The LCM provokes a reduction of the effective bandgap of the alloy, the larger the modulation, the smaller the bandgap since In rich regions fill more and confine the carriers space (see Figure 2.9) . It also improves the carriers lifetime due to their spatial separation [69].

2.4 MBE growth optimization

2.4.1 Varying growth conditions

The first study of this work aimed to find best growth conditions for GaInP, our key material. As seen in the previous part, the operator has a few levers to play with to influence the growth in a MBE machine: growth rate, substrate temperature, V/III ratio, or type of substrate. In this work, we chose to fix the growth rate to 1 µm/h, a reasonable value regarding the fabrication cost. For similar reasons, no off-cut substrates were tested as their impact in MBE growth does not seem to justify an increase of production cost.

Therefore, we focused on the effects of the growth temperature and phosphorus BEP (V/III ratio). As seen in section 2.3 growth temperature impacts the structure of GaInP. In order to find the best growth temperature (Tg) in our MBE a batch of six samples was grown, at 450, 480, 495, 510, 540 and 580 °C. A 1 µm thick GaInP was deposited on a (100) GaAs substrate.

Standard growth procedure consists in degassing the GaAs substrate at 400°C for an hour in the loadlock, de-oxidation in the growth chamber around 620°C under As flux. Then a GaAs buffer is grown until smooth surface is obtained, and finally we start the growth of the "proper" structure of the sample in the desired conditions.

The GaInP samples grown at 540 and 560°C, produced a spotty RHEED pattern and their surfaces have a milky aspect. At those temperatures, In and P desorb from the sample surface resulting in a roughening of the surface which is detrimental for the sample quality. The results from section 2.4.2 to section 2.4.4 are based on the study of the rest of those samples.

Then, we investigated the influence of the V/III ratio by changing the BEP of phosphorus during the growth. This batch of sample is passivated with AlGaInP, thus a 500 nm GaInP layer is sandwiched between AlGaInP layers: 200 nm at the rear and 20 nm at the surface. The phosphorus pressure tested were $1.4.10^{-5}$, $8 .10^{-6}$, $5 .10^{-6}$ torr. Table 2.1 summarizes the growth conditions of each sample of the study.

Sample	Tg(°C)	BEP (P) (Torr)	V/III ratio	Passivated
GCY010	450	$1.4\ 10^{-5}$	12	-
GCY009	480	$1.4\ 10^{-5}$	12	-
GCY013	495	$1.4\ 10^{-5}$	12	-
GCY008	510	$1.4\ 10^{-5}$	12	-
GCY011	540	$1.4\ 10^{-5}$	12	-
GCY012	580	$1.4\ 10^{-5}$	12	-
H6Z063	500	$1.4\ 10^{-5}$	12	yes
H8Z118	500	$8\ 10^{-6}$	7.3	yes
H8Z119	500	$5\ 10^{-6}$	4.5	yes

Table 2.1: Summary of the samples grown for the optimization of growth conditions.

2.4.2 Low temperature photoluminescence

The photoluminescence (PL) of the samples was measured at 8K. The sample is placed in a cryostat, cooled with liquid helium. The sample is illuminated with a green laser (520 nm) and its luminescence is measured with a CCD camera.

Figure 2.10 shows that a red shift of the PL wavelength occurs with an increasing growth temperature. The PL peak intensity also varies from sample to sample. In particular, the PL is one order of magnitude less intense for the sample grown at 450 °C as compared to the other samples. Looking at the PL spectra in log scale Figure 2.10 b), several peaks can be discriminated. Two peaks for the samples grown at 480, 495 and 510 °C and at least three in the sample grown at 450 °C.

X-ray diffraction Omega-2theta rocking curves were performed on the samples. This method allows to measure the lattice mismatch between the epitaxial layer and the GaAs substrate. From this mismatch, one can deduce the lattice parameter of the layer and compute its composition. Thus, we measured the indium content of each sample. The composition of the samples varies slightly. We use Adachi's model [72] to

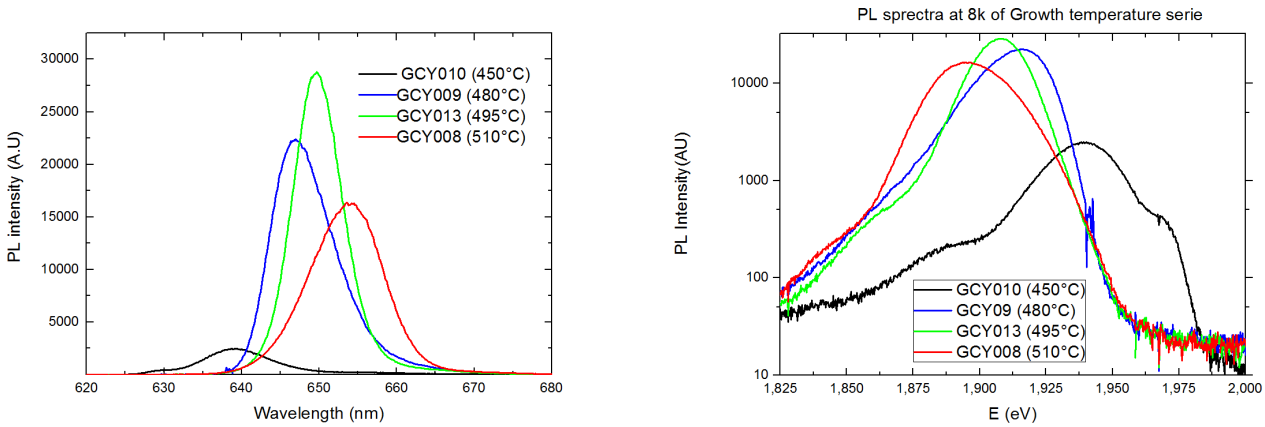

(a) (b)

Figure 2.10: Low temperature PL spectra of the Tg batch. a) in nanometers scale b) in eV and logarithmic scales.

calculate how the bandgap is impacted by such changes. The samples composition varies from an In content of 47.2% to 48.1% (shaded range Figure 2.11), in this range the theory predicts a bandgap variation of 9 meV while the experimental PL peak shifted by 44 meV. Therefore the differences in PL emission do not result only from the differences of the average composition of the GaInP layers.

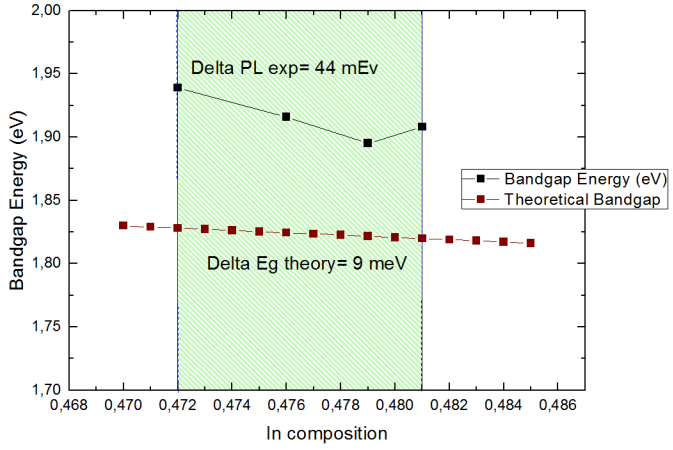

Figure 2.11: Comparison of the bandgap variation predicted from the average composition changes (in red) and with the PL position of the samples in black.

2.4.3 Effect of the excitation power on the photoluminescence

Then, we compared the sample having best PL properties, i.e. the sample grown at 495°C, and the sample having weaker PL intensity grown at 450°C.

The evolution of photoluminescence with the laser excitation power was investigated. Maintaining the sample at 5 K, the PL spectra of the two samples were measured for excitation varying from 1 µW to 50 µW. The PL of the sample grown at 495°C increases with the laser power, no change in shape is observed.

However, for the sample grown at 450°C a change of the PL spectrum shape is noted in addition to the intensity increase. Peak labeled A, in Figure 2.12 b) prevails at 1 µW (Peak B intensity is only one tenth of peak A intensity). While increasing the excitation power, the intensity of the PL peak at higher energy, labeled B, increases more than that of PL peak A. Finally, peak B dominates at 50 µW. Figure 2.13 shows in red the ratio of the two peaks and its variation with the excitation power. This reveals that peak A corresponds to a lower density of states than peak B. Increasing the flux of incident photons, peak A tends to saturate and the probability of peak B transition become the highest one. This indicates that peak A is related to carrier recombination from localized states, those states are in limited numbers and get filled while rising the excitation. On the contrary, delocalized states do not saturate.

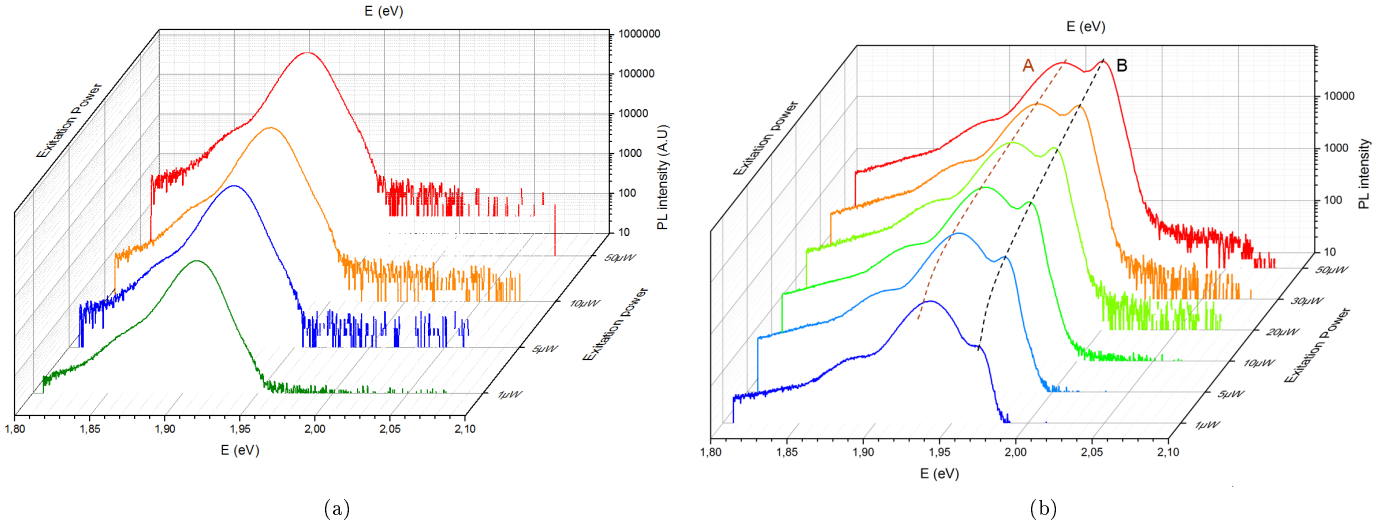

Figure 2.12: Evolution of the PL spectra with excitation laser power increase, measured at 10 K. a) Sample grown at 495°C b) Sample grown at 450°C, two distinct peaks: low energy peak labeled A and high energy peak labeled B.

Figure 2.13 a) shows the PL intensity maximum for samples grown at 450°C (in red) and 495°C (in black). PL intensity of sample grown at 495°C increases much faster with the excitation power. As the samples are not contacted by any mean for those measurements, all the carriers generated by the light absorption eventually recombine. Therefore, Figure 2.13 suggests that the sample grown at 450°C contains much more non-radiative centers, resulting in lower PL intensity and slower PL increase with the excitation power than for the other sample.

2.4.4 Temperature dependent photoluminescence

Fixing the excitation power to 50 µW, the PL spectra of the sample were measured for temperatures varying from 5 K to 300 K. Figure 2.14 displays the results.

For the sample grown at 450°C, the peaks A and B are found in the low temperature spectra. The PL intensity decreases with temperature and the intensity of peak A quenches at temperature higher than 70K. Only peak B remains above 150K.

For the best sample (grown at 495°C), PL emission is around 1.91 eV and the intensity of the luminescence decreases slowly with increasing temperature (peak labeled 1 in Figure 2.14 b). Above 70 K, another emission appears at higher energy and its intensity decreases more slowly when the temperature is increased.. Both peaks have a similar intensity at room temperature (56 A.U for peak 1 and 76 A.U for peak 2) leading to broad PL emission.

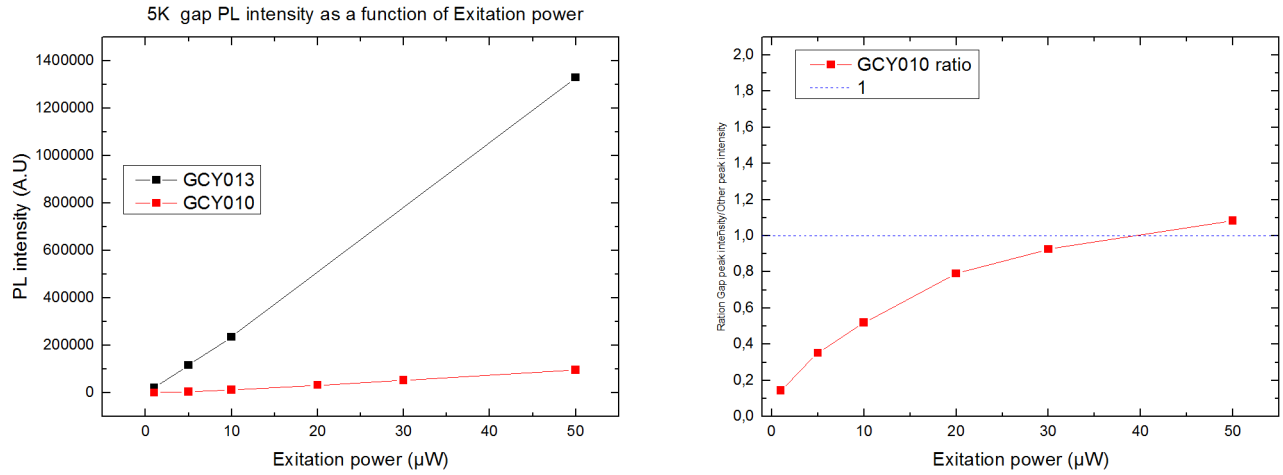

(a) (b)

Figure 2.13: Evolution of PL intensity with the excitation power. a) Comparison of maximum PL intensity between samples grown at 450°C and 495°C.) Comparison of the PL intensity of the two peaks visible in the spectra of sample grown at 450°C: $I(PeakB)/I(PeakA)$.

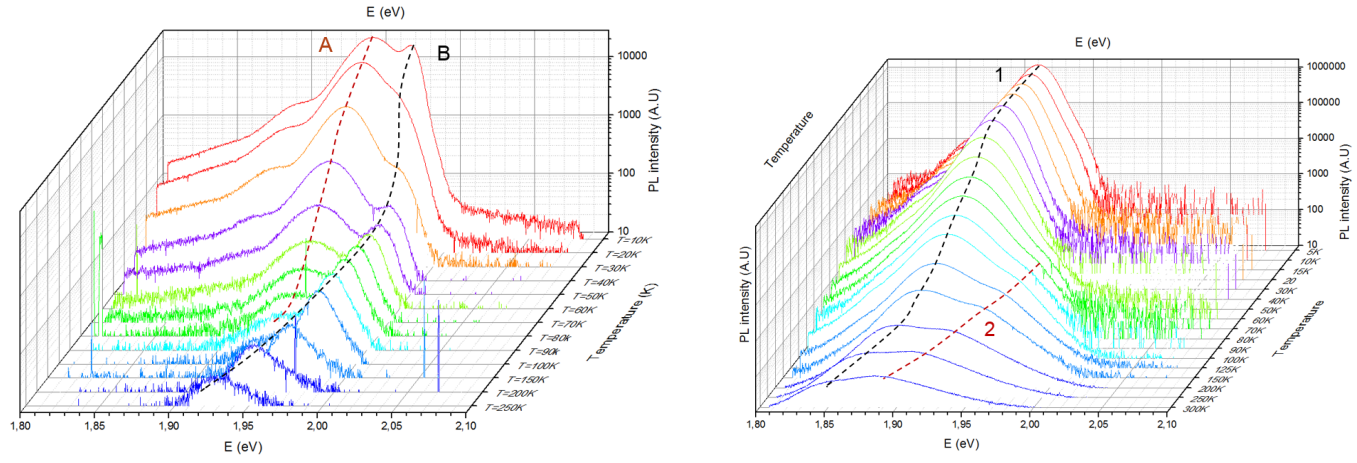

(a) (b)

Figure 2.14: Evolution with temperature of PL spectra of two samples. a) Tg=450°C, one can discriminate peak A and B and follow their evolution with temperature. b) Tg=495°C, apparition of a second peak when T is above 70K.

PL intensity with temperature

In order to analyze the information given by those spectra, we consider now the integrated PL intensity, I_{ph}, and its variation with the temperature. For semiconductors, the temperature dependence of the PL intensity is often described by the following empirical law:

$$I(T) = \frac{I_0}{1 + A * exp(\frac{-Ea}{kT})} \tag{2.1}$$

Where I_0 is PL intensity at 0 K, k is Boltzmann constant, A is a constant specific to the sample and E_a is an activation energy. The law describes how thermal energy depletes the emitting states by the activation of a non-radiative recombination channel. The activation energy E_a represents the energy needed to trigger these non-radiative losses. With the Equation 2.1 law, the PL intensity is almost constant in the lowest temperature range. When T becomes comparable to Ea, the PL intensity decreases since carriers have access to the non-radiative centers.

Figure 2.15 shows the evolution of the integrated PL intensity with temperature for the samples GCY013 (Tg=495°C) and GCY010 (Tg=450°C). The samples grown at 495°C exhibits an a behavior described by Equation 2.1, with a plateau at low temperature. Good agreement is obtained with an this law with I_0= 39129 and Ea=22 meV. However one notices that the experimental intensity decreases faster than the fit at high temperature, data "unhooking" from the fit above 70K, indeed. Adding another canal for non-radiative recombination, with activation energy E_{a2} improves the fit at high temperature.

$$I(T) = \frac{I_0}{1 + A * exp(\frac{-Ea}{kT}) + B * exp(\frac{-Ea2}{kT})} \tag{2.2}$$

The fit using Equation 2.2 is shown in red Figure 2.15. It indicates that two non-radiative recombination canals are present in the sample with activation energy of $Ea = 12$ meV and $Ea_2 = 39$ meV and causes the important reduction of the integrated PL intensity with the temperature.

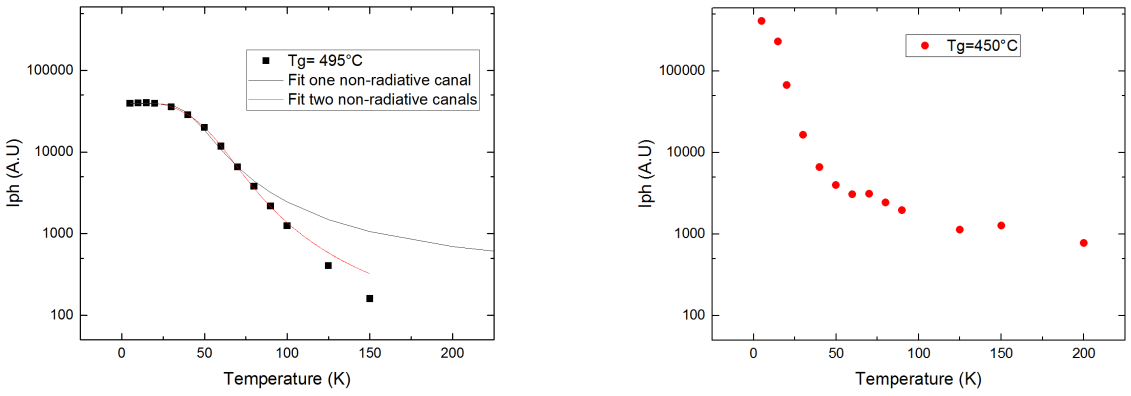

(a) (b)

Figure 2.15: Evolution of PL intensity with temperature for both of the studied samples. a) Integrated PL intensity of sample grown at 495°C and fit with Equation 2.1 b) Integrated PL intensity of sample grown at 450°C.

For the sample grown at 450°C no PL intensity plateau is present at low temperatures. On the contrary, a strong intensity decrease occurs from the lowest temperatures. Such behavior has been reported in material having strong localization effects, like amorphous semi-conductors [73]. The intensity at low temperature is well described by the following expression:

$$I(T) = \frac{I_0}{1 + B * exp(\frac{T}{T0})} \tag{2.3}$$

Where B is a constant related to the sample and T0 is specific to the loss process. In this case, the intensity reduction is thought to result from localized carriers tunneling toward non-radiative traps and T0 indicates how easy the localized carriers get trapped.

GCY010 behavior is well described by Equation 2.3 law at low temperature. At higher temperature the PL intensity decreases more slowly and is in agreement with a more classic behavior described with Equation 2.1 . As shown in Figure 2.16, the photoluminescence of this sample is well described by the combination of the two laws.

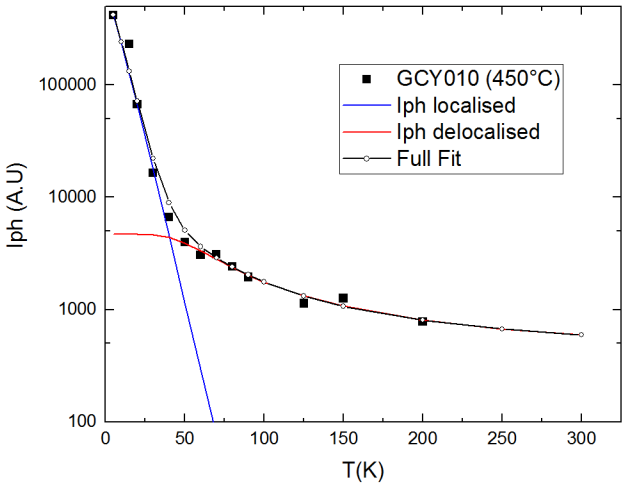

Figure 2.16: Fit of the evolution of the PL intensity of the sample grown at 450°C. In blue, fit of localisation PL effect with Equation 2.3, in red fit of delocalised effects with Arrhenius law *E*quation 2.1.

Sample	Arrhenius activation				Localised recombination centers		
	Ea (meV)	Io	A	B	To (K)	Io	B
Tg= 495°C (first recombination canal)	12.3	39809	13	-	-	-	-
Tg= 495°C (second recombination canal)	39	-	-	2571	-	-	-
Tg= 450°C	18.4	4681	14	-	7.3	$1.7.10^6$	1.65

Table 2.2: Fit parameter for samples modeling with Equation 2.1(Arrhenius activation of non-radiative channel) and Equation 2.3 (localization effects).

PL peak position with temperature

Finally we can use Figure 2.14 to study how the different PL peaks energy evolves with the temperature. The shift of the PL emission with temperature is related to the bandgap variation with temperature. This variations is well described by the empirical law developed by Varshni and al [74]:

$$Eg(T) = Ego - \frac{\alpha * T^2}{T + B} \tag{2.4}$$

Where Ego is the bandgap at 0K, α and B are constants related to the material.

Focusing on the sample grown at 450°C, (blue triangles Figure 2.17), one notices:

- Peak B position follows a Varshni trend at high temperature, but it is red-shifted at lower temperature.
- Peak A emission is only visible at temperatures below 100 K and its position has an inverse S shape. Peak A emission is about 30 meV lower than peak B.

Peak B behavior corresponds to a well-known trend in III-V alloys [75], which was often associated to ordering effects in the GaInP when emission at low temperatures is below 1.9 eV[76, 77]. At low temperatures, carriers are "frozen" in shallow localized states. This results in a PL emission red shift in comparison to the bandgap value. When the temperature is increased, the carriers can escape from these localized states and reach the delocalized states of the conduction band. The PL emission then corresponds to the conduction to valence band transition and the peak position follows a Varshni trend.

Peak A is the emission form deep localized states. Its inverted S shaped with temperature also corresponds to a "freezing" effect. At lowest temperature, carriers are frozen and emit from their localized state. Increasing the temperature slightly, allows spatial carrier motion and thermalization to lower energy states localized close-by. Consequently the energy emission reduces slightly. Then, further increase of the temperature provokes a mixed regime and finally the quenching of the peak A emission in favor of peak B emission.

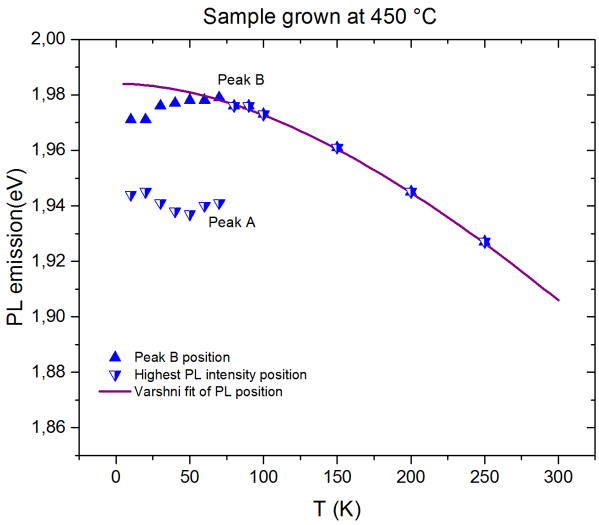

Figure 2.17: Evolution of peak positions in the PL spectra with temperature. Blue upright triangles show the position of the peak B, reversed triangle shows the position of the peak of highest intensity in the spectrum. Peak A quenches at 75 K.

Figure 2.18 gathers the positions of PL emission peaks of the sample grown at 495°C. Main peak (peak 1) exhibits a behavior comparable to that of the peak B in the other sample and corresponds to the bandgap emission. The second peak (peak 2) also behaves like a bandgap emission, but at higher energy. Note that the apparition of the peak 2 matches the temperature at which Equation 2.1 starts to fail in fitting the PL intensity of the sample.

2.4.5 Interpretation of the PL characterizations

The PL characterizations allows to discuss the impact of the growth temperature on the optical properties of the GaInP layers.

Low growth temperature results in a higher effective bandgap, but the sample suffers from the presence of localized states in the bandgap. Indeed the temperature dependences of the peak A intensity and energy indicate that this emission can be attributed to localized states. The evolution of the PL spectra of the sample with excitation power also confirms it. The density of states related to peak A is lower than that of

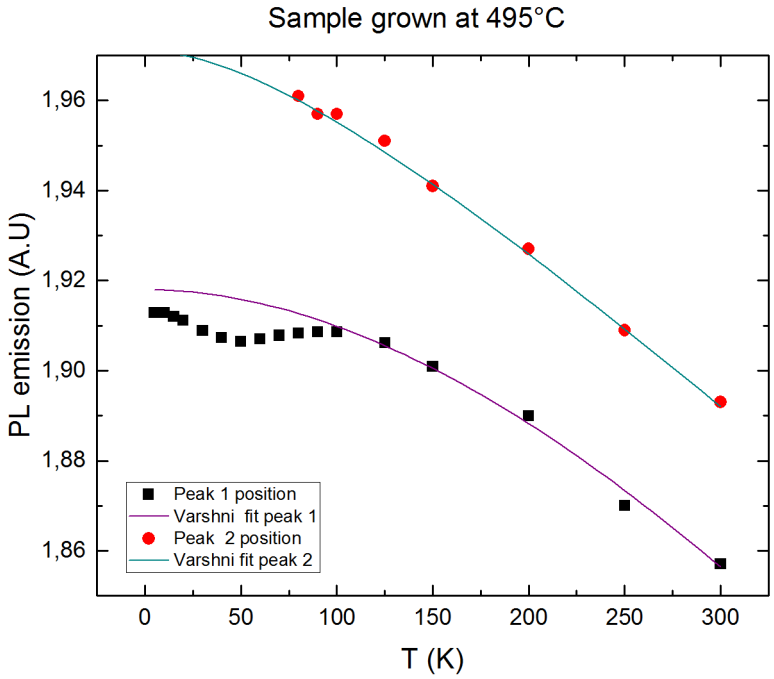

Figure 2.18: Focus on sample grown at 495°C, in black peak 1 position in red peak 2 position.

peak B, resulting in lower increase of peak A intensity with laser power increase, a classic evolution of PL spectra for localized state emission.

When grown at 495°C, the GaInP alloy does not show a PL contribution similar to peak A which is associated to localized states 30-40 meV below the bandgap energy. Nevertheless it does exhibit shallower localized states that disrupt its bandgap emission at low temperature. Surprisingly another emission appears at higher temperatures. The temperature dependence of this emission also corresponds to a "bandgap like variation". This emission indicates local variations of the alloy composition. At low temperature, the PL is dominated by the emission of In-rich regions, whereas the Ga-rich regions start to emit at higher temperature (near 75 K).

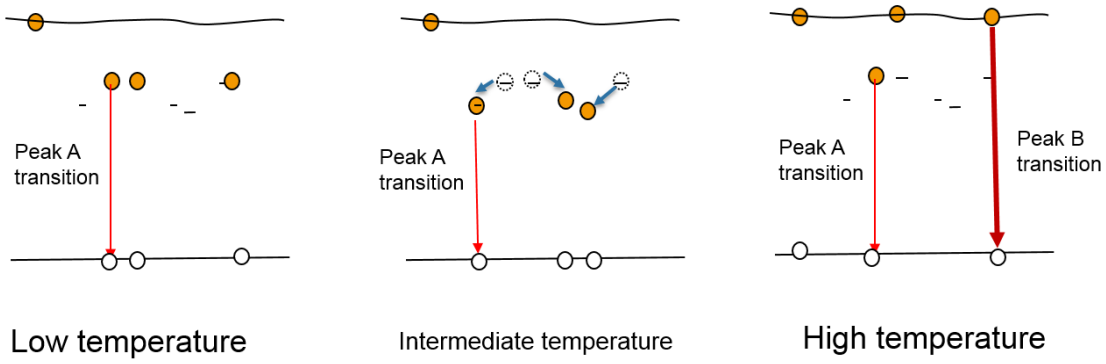

Figure 2.19: Schematic of the PL processes observed for the sample grown at 450°C. PL emission results mainly from a near-band-edge transition and transitions from 30-40 meV deep states.

As a conclusion rising the growth temperature reduces the effective bandgap of GaInP, probably because

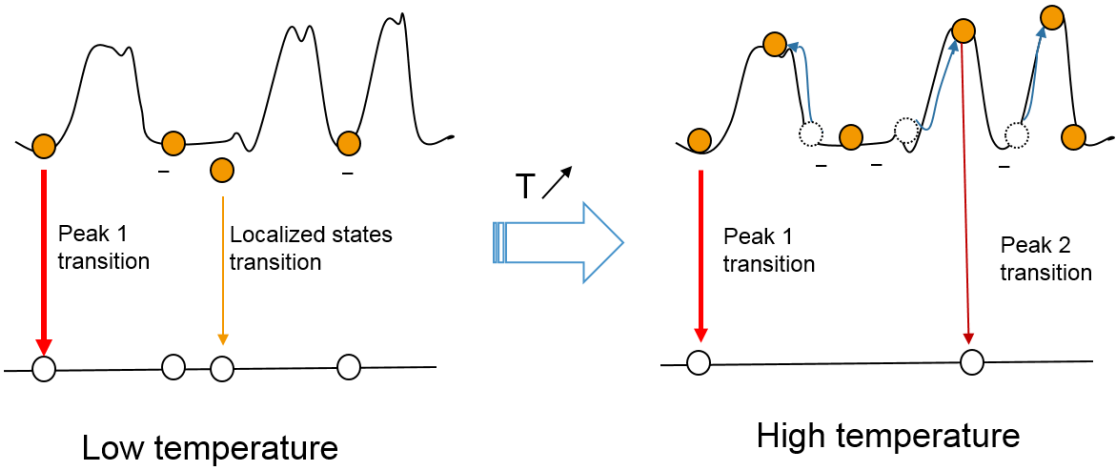

Figure 2.20: Schematic of PL transitions observed for the sample grown at 495°C. Presence of shallow states and of bandgap spatial fluctuations.

of some alloy ordering effect as described in section 2.5.1. The optical quality (PL efficiency) is the best at Tg=495°C. For this growth temperature, the sample does not suffer from deep states in its bandgap.

2.4.6 Effect of the V/III ratio on GaInP

Finally, the influence of the V/III ratio on the luminescence was briefly studied. As mentioned in Table 2.1, passivated samples were grown at a fixed temperature of 500°C and with different phosphorus fluxes.

The samples were characterized by cathodoluminescence.

Cathodoluminescence principle and experimental set-up

Cathodoluminescence is an alternative method to study sample luminescence. With PL the sample is excited with light (usually a laser beam) while with cathodoluminescence it is a high energy electrons beam that provides the excitation. Figure 2.21 illustrates the experiment set-up. In a continuous regime a tip is heated to produce electrons, the generated electrons are accelerated by to a tension applied between the tip and the sample, the beam is focused on the sample with lenses.

The electrons enter the sample and excite a finite volume, free carriers are thus generated. They eventually recombine radiatively and produce a luminescence signal that is collected and passes through a spectrometer. The spectrum is directed to a CCD camera that records the luminescence.

For time resolved measurements, the electron beam is pulsed by a laser excitation. The laser beam is focused on the small tip and tears electrons off periodically, a streak camera is used to study the luminescence.

The sample is fixed to a stage of controllable position and temperature.

Experiment:

During the measurement, the temperature was 10K, the three samples were placed on the same stage and measured one after the other to ensure same measurement conditions.

The CL spectra show that the luminescence intensity decreases with the V/III ratio. Figure 2.22 displays normalized CL spectra of the samples, the sample grown at highest phosphorus flux is the most intense, and as the smaller full width half maximum (FWHM).

Then the cathodoluminescence energy can be compared with the position reported in the previous PL study. In Figure 2.23 , the PL peak position of the sample grown at different temperatures are plotted in black and effect of the V/III ratio on the PL energy is plotted in red. One can notice that the reduction of the phosphorus pressure produces a 18 meV red shift of the PL peak. This suggests a reduction of the alloy bandgap which will be confirmed by the structural study developed in the next section.

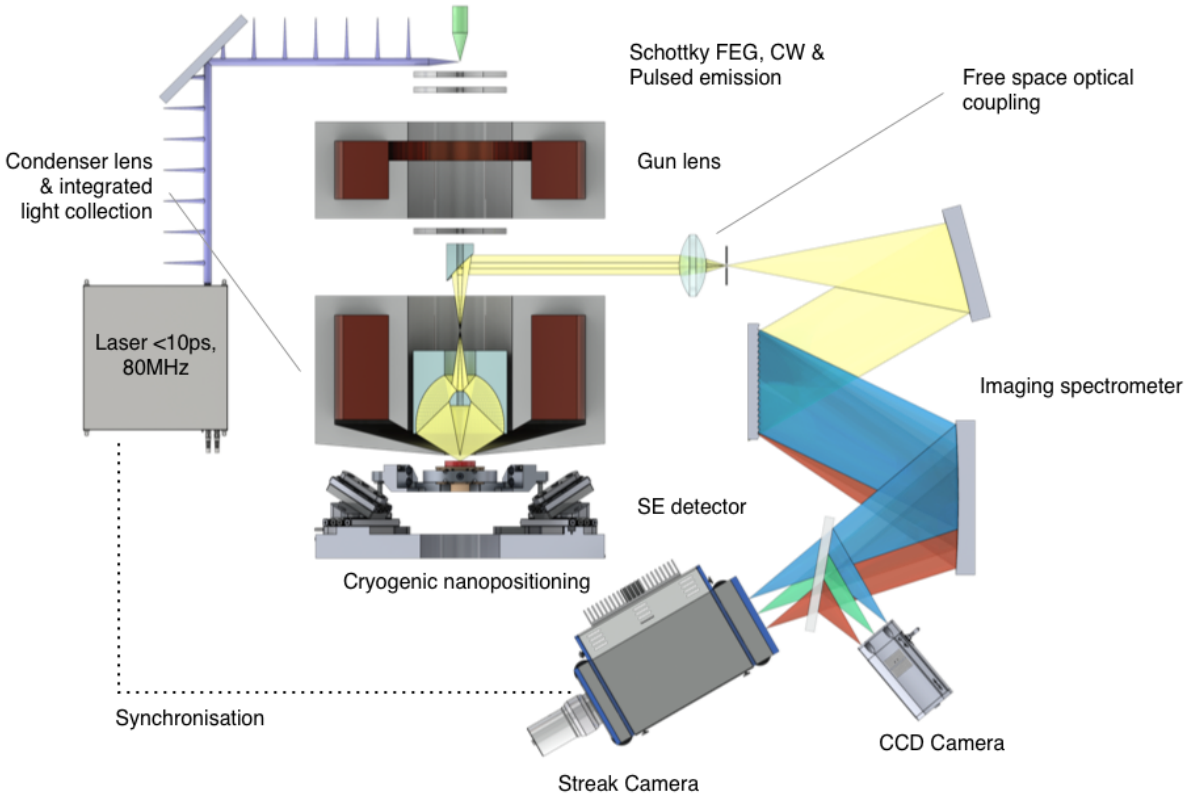

Figure 2.21: Scheme of Cathodoluminescence set up. From [78].

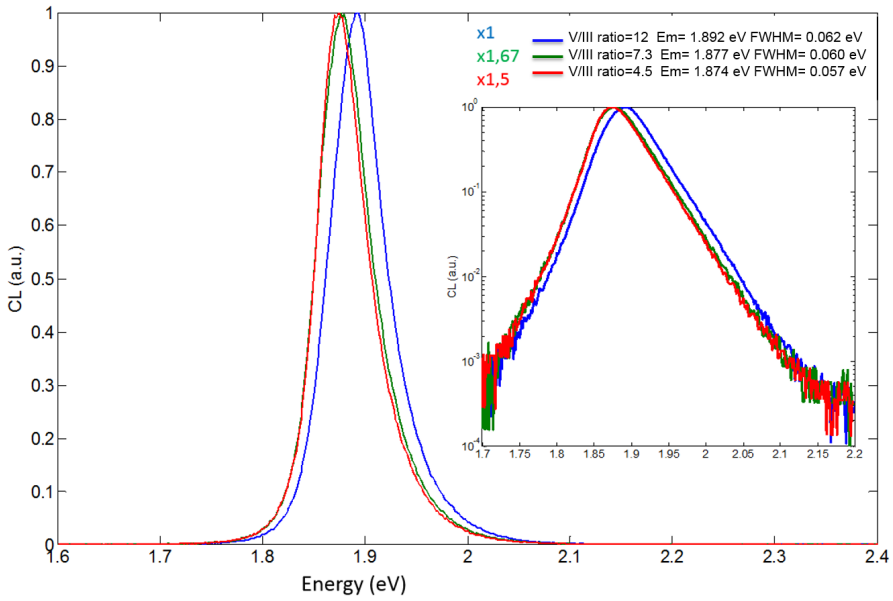

Figure 2.22: Cathodoluminescence of the samples grown at different phosphorus pressures.

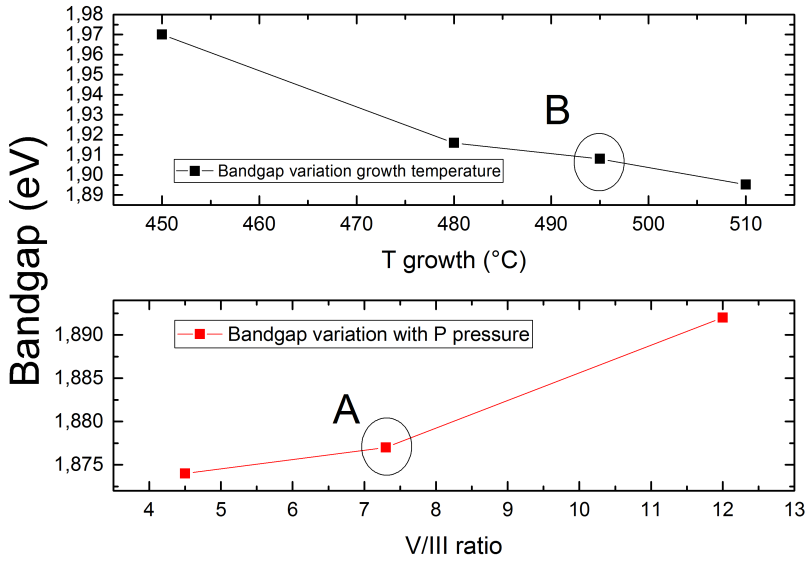

Figure 2.23: Bandgap of all the samples of this study. Samples grown at different temperatures and a 12 V/III ratio in black, samples grown with different phosphorus pressures and at 500°C in red. The band gap reduces when the growth temperature is increased and when the P flux is decreased. Growth conditions A and B are further investigated in the next section.

To conclude on the luminescence data, the optimal GaInP quality is obtained for a growth temperature around 495-500 °C and for a phosphorus pressure around $1.3.10^{-5}$Torr (V/III ratio of 12). Indeed, these conditions produce the highest PL intensity, they maximize the radiative recombination of the generated carriers. Though the lower P flux leads to bandgap closer to the ideal value for the Si-based tandem cell (1.74 eV), we opted for a high P flux which gives the highest PL efficiency.

2.5 Specific crystal configuration

2.5.1 Scanning transmission electron microscopy

In order to investigate the lower bandgap energy observed when decreasing the phosphorus pressure during the growth (Figure 2.23), scanning transmission electron microscopy (STEM) was used. With this technique an electron beam is focused on a thin sample. Passing through, electrons are scattered by atoms and are collected by detectors at the back of the sample. This annular dark filed imaging technique is sensitive to the atomic mass of the scanned atoms and a chemical contrast is obtained, allowing to image the atoms arrangement in the crystal and characterize their concentration. Thus STEM technique will allow to investigate the structural and chemical properties of the samples. We have performed High angle annular dark field imaging (HAADF) configuration in order to obtain best chemical contrast, by using a TEM/STEM Titan Themis equipped with a probe aberration correction which allows atomic scale resolution. (Heavier atoms deflect more electrons at high angles.)

A thin cross-section of sample H8Z118 (grown at 500°C , BEP(P)= 8 10^{-6} Torr) and of a solar cell grown in same conditions as sample GCY013 (495°C, BEP(P)=1.4 10^{-5}Torr) were prepared with a focused ion beam (FIB) set-up. It allows to obtain a few nanometers thick lamella with homogenous thickness and parallel sides: the requirements for good STEM imaging.

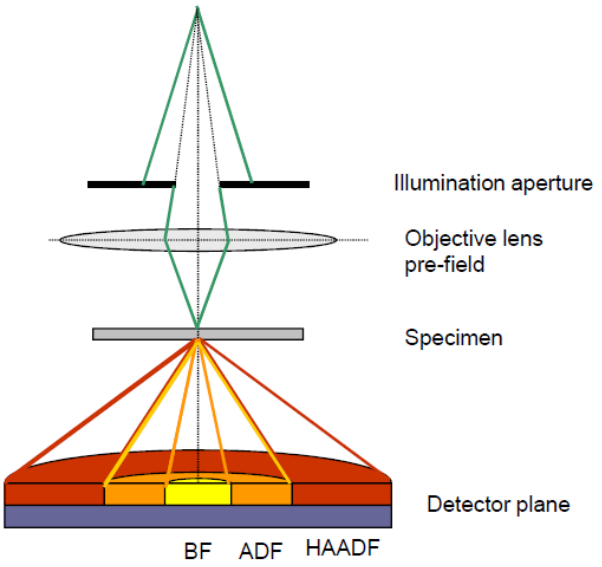

(a) From [79]

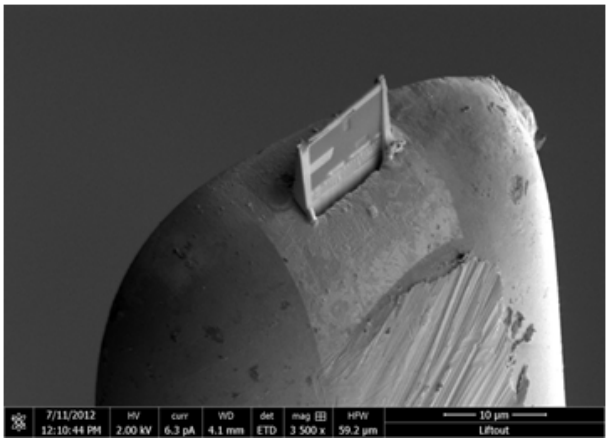

(b) From [80]

Figure 2.24: a) Sketch of the STEM principle to focus and collect the electron beam. b) Image of a sample slice prepared with FIB for STEM imaging.

From HAADF images of the solar cell sample, the different layers can be distinguished due to their different chemical compositions. GaAs appears bright, GaInP also, as heavy In compensates for phosphorus which is smaller than As (atomic number Ga(31), As (33), In(49) and P(15) indeed). Passivating layers appear darker since they contain Aluminum (Al(13)) smaller than Ga. Indeed, in the Rutherford scattering approximation, the HAADF intensity is proportional to the square of the atomic number. We observe a uniform HAADF intensity within each layer, even at the highest magnification, (Figure 2.25). This indicates a homogenous composition.

The situation is different for the sample grown at lower phosphorus pressure. Figure 2.26 displays HAADF images of this sample: the GaAs layer is homogenous but the two phosphides layers show pronounced variations of intensity along the direction perpendicular to the (100) growth axis. The intensity fluctuations start at the AlGaInP/GaAs interface and propagate through the AlGaInP and GaInP layers. They correspond to short and quite regular chemical modulations in these layer. The modulation period appears larger in the GaInP layer.

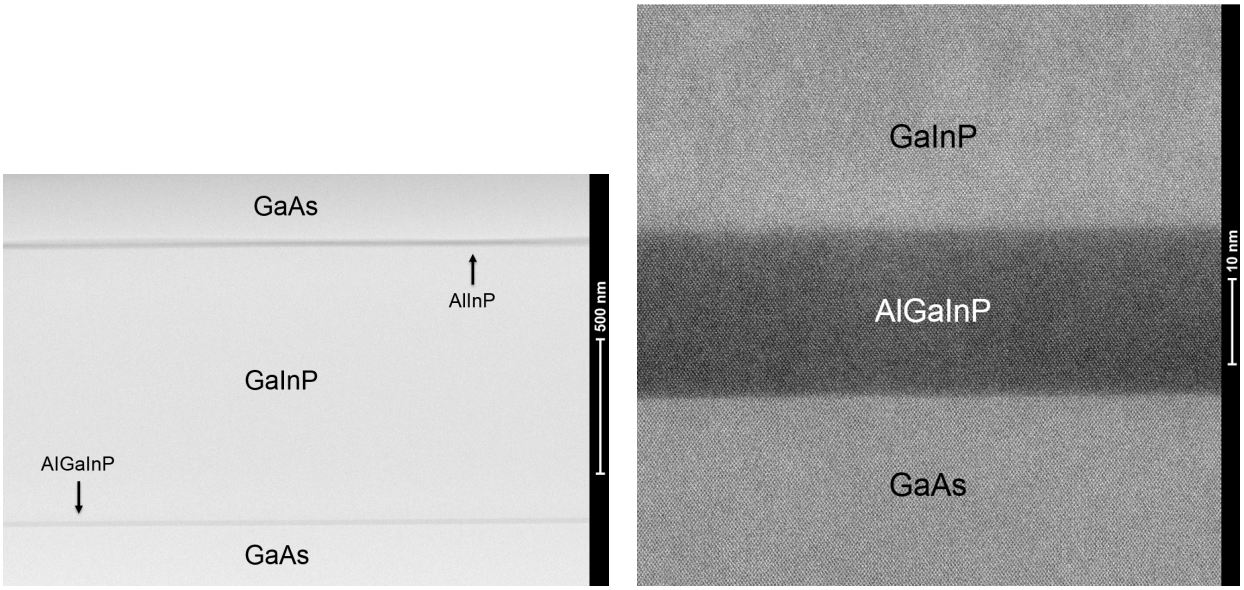

(a) (b)

Figure 2.25: STEM images of solar cell sample grown in "A conditions" a) image of a whole cell structure b) higher magnification of the back of the cell: GaAs, AlGaInP and GaInP layers appear homogenous.

Selected area electron diffraction (SAED) patterns collected attest that the observed modulations are periodic. Figure 2.27 a) is a diffraction pattern taken in the uniform GaAs buffer. This diffraction pattern is composed of circular spots related to each family of crystalline planes. The diffraction pattern produced by the GaInP layer is shown in Figure 2.27 b). The spots are now extended horizontally (along the <110> in plane direction) as a result of the periodic modulation presents in the layer. This proves that the contrast modulation is not related to thickness inhomogeneities which could be due to FIB preparation.

HAADF intensity profiles were taken from the images to quantify the period of the modulation in AlGaInP and GaInP. With this method, we measured a period of 18.8 nm in the GaInP and 6 nm in the AlGaInP.

As explained earlier, the contrast observed in STEM is related to the atomic number of the atoms interacting with the incident electrons. Modulations are observed in both AlGaInP and GaInP, but the contrast is more pronounced in $(Al_{0.3}Ga_{0.7})_{0.5}In_{0.5}P$ than in GaInP. This can be explained by the higher difference in the atomic numbers of Al and In in comparison to the difference between Ga and In. Hence, this does not necessarily mean that the In composition modulation is larger for the quaternary alloy.

We attempted to confirm this by using EDX (Energy dispersive X-rays). This analytical tool, installed in our STEM microscope, allows to determine the relative concentration of each species in the alloy. The concentration of the species were in agreement with the nominal composition of the alloy, though the EDX signal did not permit to measure the modulation period. Composition changes are too small to be detected by this technique.

Therefore we used the HAADF image of the sample to evaluate the composition variation in the GaInP, indeed the HAADF intensity depends on the atomic number of the species. Empirical studies have shown that the intensity is proportional to $Z^{1.7}$, while Rutherford scattering theory predicts a Z^2 dependence. In Figure 2.28 is plotted in dark the HAADF intensity profile. The mean intensity varies slightly due to a drift of the lamella thickness. Around this baseline, the HAADF intensity fluctuates between maxima, indicating In-rich areas and minima corresponding to Ga-rich areas.

In GaInP, where P accounts for half of the atoms in the lattice and the other half is shared between Ga and In, the HAADF intensity follows the equation below:

$$I_{HAADF}(x) = \alpha.[\frac{1-y}{2}.Z_{Ga}^{1.7} + \frac{y}{2}.Z_{In}^{1.7} + \frac{1}{2}.Z_{P}^{1.7}] \tag{2.5}$$

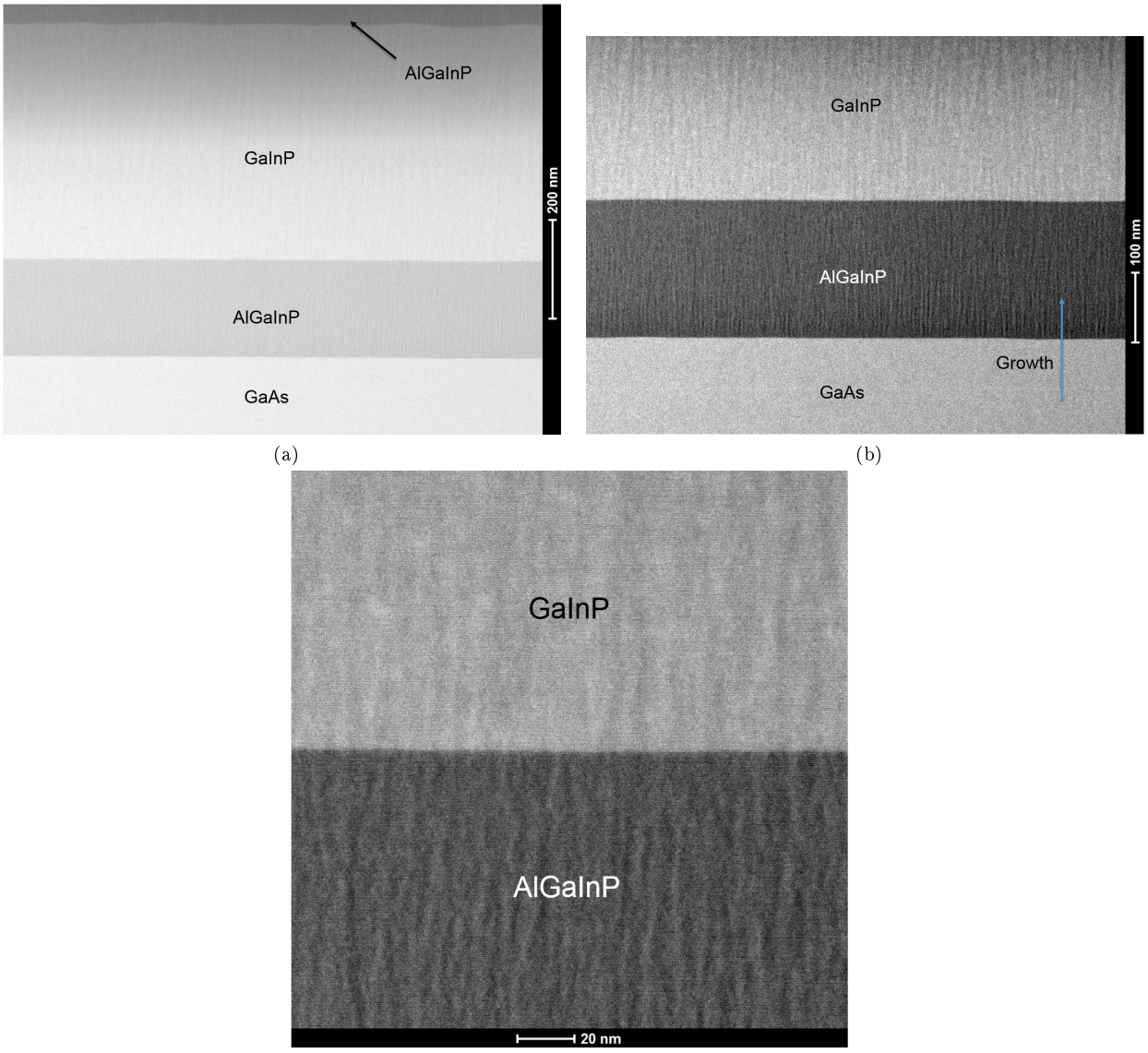

Figure 2.26: STEM images of the sample grown at low phosphorus pressure. a) view of the whole structure b) higher magnification of the GaAs buffer, AlGaInP and GaInP layers c) Focus on AlGaInP/ GaInP interface.

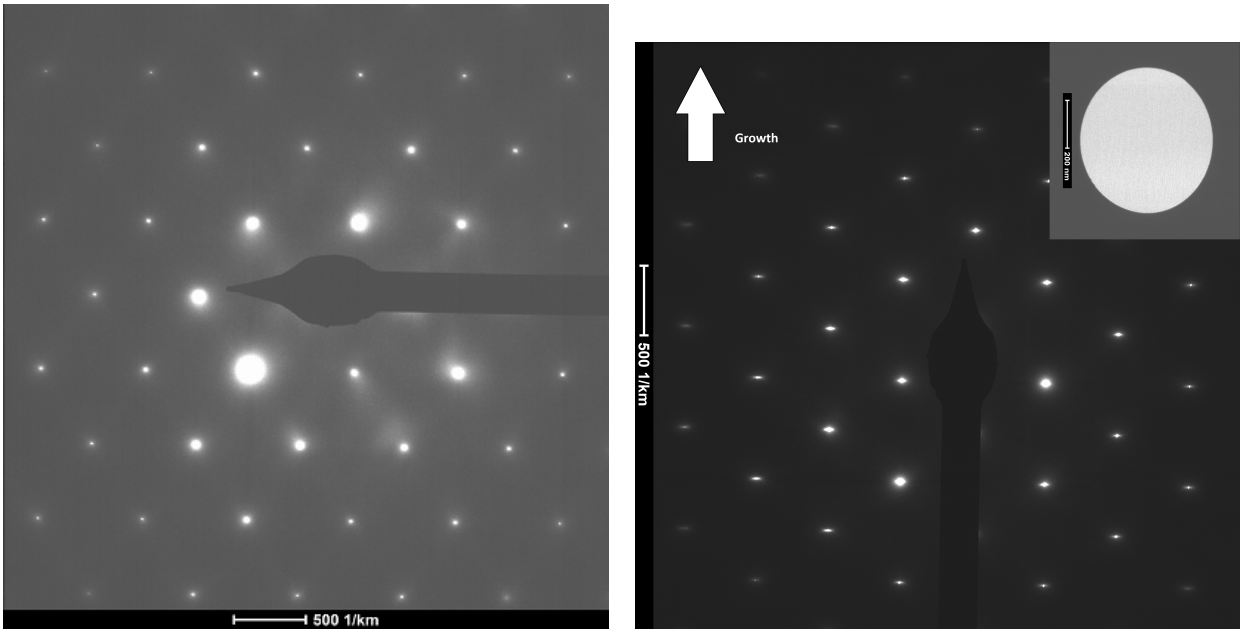

(a) (b)

Figure 2.27: STEM diffraction pattern for a) GaAs buffer layer b) GaInP layer.

Were α is a constant related to the lamella and its thickness, y is the In content, Z_{Ga} , Z_{In} and Z_P are the element atomic numbers (Z_{Ga}=31, Z_{In}=49, Z_P=15). α can be determined assuming that the average HAADF intensity corresponds to a lattice matched composition y(In)= 0.484. Then, the In content y can be determined for every x position in the HAADF profile using:

$$y_{In}(x) = \frac{1}{Z_{In}^{1.7} - Z_{Ga}^{1.7}} . [\frac{2.I_{HAADF}(x)}{\alpha} - (Z_{Ga}^{1.7} + Z_P^{1.7})] \tag{2.6}$$

Figure 2.28 shows in red the In content variation in the layer deduced from the HAADF profile. There is a variation of about 2.2% of the In content around the baseline intensity, with $y(In)_{max}$= 0,495 and $y(In)_{min}$=0.473 in the center of the curve (which corresponds to the position where alpha was determined).

Using the Adachi model, this difference leads to a 32 meV difference in bandgap between In rich (Eg=1.899 eV) and In poor areas (Eg=1.931 eV).

2.5.2 Grazing incidence X-ray diffraction

We also analysed the sample presenting inhomogeneities with Grazing Incidence X-ray Diffraction (GIXRD) which allows to measure the in-plane lattice parameters. This is a more statistical approach as the measured area is of the order of the centimeter. The change in composition induces slight periodic changes in lattice parameter. Like in a superlattice, it results in the apparition of satellite peaks in the XRD scan.

The use of non-coplanar GIXRD allows to probe the plans perpendicular to the sample surface. During the scan, X-rays arrive at fixed incidence, the detector spans a range of angles around the (400) Bragg angle of GaAs. Like in the diffractogram of Figure 2.29, the recorded scan presents an intense peak close to the GaAs Bragg peak position and two satellite peaks due to the periodicity of the modulation.

Having θ_{GaAs}, θ_{sat1} and θ_{sat2} for the peak position, the modulation period is determined with:

$$m = \frac{\lambda_{cu}}{2 * [sin(\theta_{GaAs}) - sin(\theta_{sati})]} \tag{2.7}$$

Where λ_{Cu} is the x-rays wavelength, and m the modulation period in nanometers.

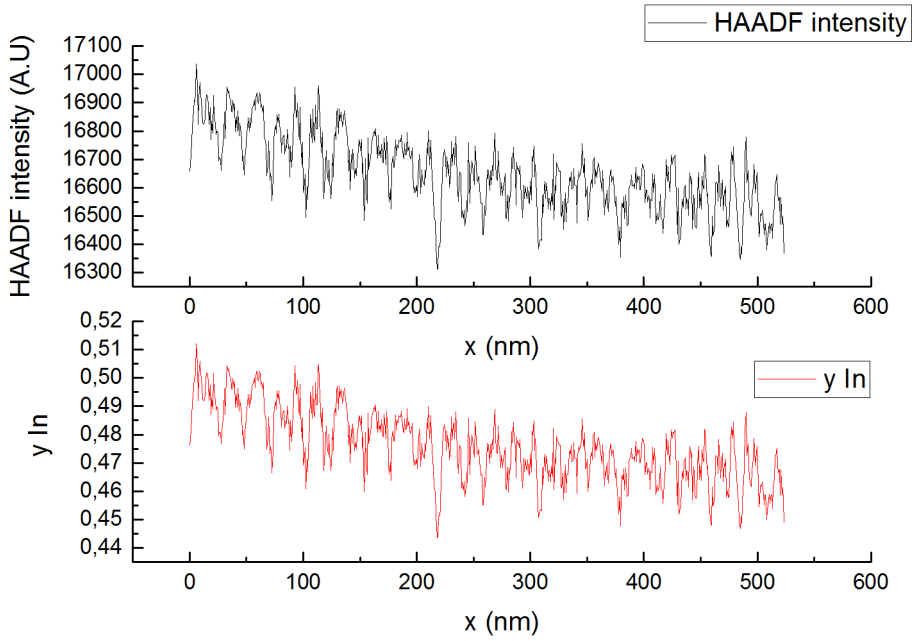

Figure 2.28: In black HAADF intensity profile measured in the GaInP. In red In content (y) deduce from the HAADF data.

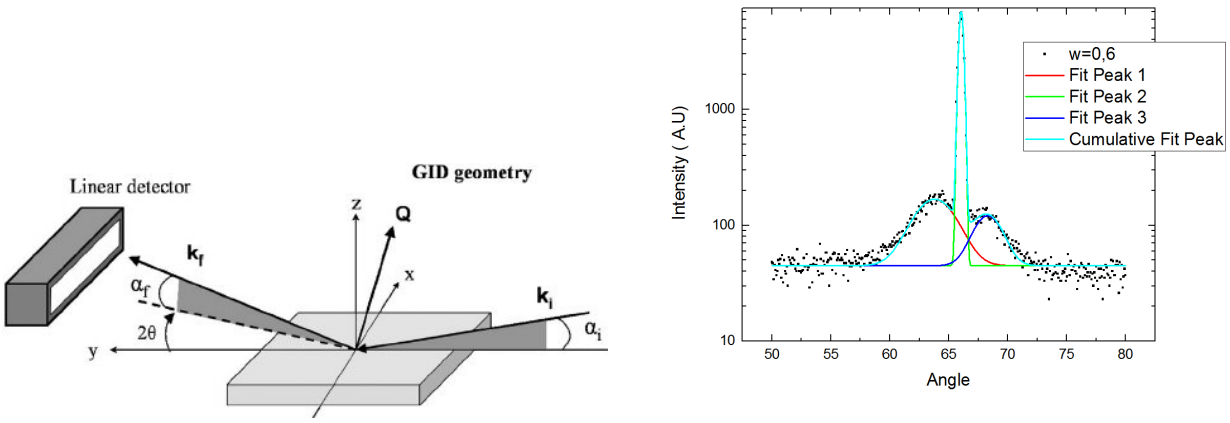

(a) from [81] (b)

Figure 2.29: Determination of the modulation period with GIXRD a) GIXRD scan configuration b) Diffractogram measured at an incidence angle w=0.6° (black dots) and fit for period determination.

Interesting point with this experiment is that the angle of incidence, w, determines the depth probe in the sample. Increasing the incidence angle, the operator investigates the modulation deeper in the sample. Thus GIXRD scans were measured at incidence varying from 0.3° to 0.6°, the peak positions were fitted to extract the modulation period. Table 2.3 gathers the modulation period calculated for each angle. The period decreases while probing deeper, it is consistent with the trend seen in the STEM images.

The GIXRD scan does not measure the modulation in the same direction as the axis seen in the STEM images. In STEM images, the modulation is probed along the (01-1) axis while the modulation measured with GIXRD is probed along the (100) axis.

Therefore, the two methods confirm the presence of lateral periodic compositional fluctuations in two directions of the sample grown at lower phosphorus pressure.

Incidence angle (°)	Modulation measured (nm)
0.3	7.7
0.4	6.2
0.5	5.2
0.6	4.6

Table 2.3: Modulation periods calculated from GIXRD data.

2.5.3 Conclusion on the impact of growth conditions on the phosphide alloys

Combining STEM imaging and GIXRD results give further information on the composition modulation observed in the GaInP sample. The two methods reveal composition modulation in two directions: [100] and [1-10]. This suggests that the GaInP layer contains structures resembling columns of different compositions.

This information indicates that with the STEM imaging, the composition obtained from the HAADF intensity results from the averaging of several "columns" comprised in the 100 nm thick GaInP lamella. Therefore, the 2.2% composition fluctuation measured is lower than the real composition difference between In rich and In poor areas, and as a consequence the 32 meV bandgap difference is underestimated too.

Let's put this characterization in perspective with the PL study led earlier in the chapter. The sample grown at 495°C and a 12 V/III ratio appears homogenous in the HAADF images. However two "bandgap-like" PL peaks were observed during the PL characterization in Section 2.4.4. A difference of 30 meV is seen between the two PL peaks in Figure 2.18. This is of same order as the "underestimated composition modulations" determined with HAADF for the sample grown at V/III ratio of 7.3.

Small composition variations in the GaInP, grown at 495°C and V/III ratio of 12, may be the cause of the apparition of a higher energy transition in the PL spectra when rising the temperature. However the modulations originating for those growth conditions, which are thus lower than 2%, were probably not visible in HAADF images due to the "averaging effects" discussed above.

.

2.6 Doping of the III-V phosphides

In this section, we will address a few doping problematics that emerged during our calibrations. In our MBE set-up, we use Si as n-type dopant and Be as p-type dopant. Si is a column IV element and as such, it is an amphoteric impurity in the III-V alloys. This means that it can be both p and n type dopant for III-V alloys. The preferential Si configuration is donor-like (it substitutes Ga in GaAs), i.e. it is a n-type dopant. However at high concentration, it starts to incorporate as a p-dopant (As substitution) and this lead to self-compensation of the doping [82, 83]. Therefore, a cautious doping characterization is needed for the alloys used in the solar cells.

In general, in MBE, the concentration of dopants incorporated in a layer is fixed by the flux of dopant atoms which can be controlled by the temperature of the dopant effusion cell, and the growth rate of the matrix alloy (the slower growth rate, the higher dopant concentration for a fixed dopant flux). Then, to be active, the doping impurity must be ionized in order to provide a free carrier (electron or hole). Good dopants produce a shallow energy level, just below the conduction band (donors) or just above the valence band (acceptors). If the energy level is too deep, a significant fraction of dopants may not be ionized, even at room temperature. This results in a difference between the concentration of doping impurities in the material and the carrier concentration measured by Hall effect.

For this purpose, 1µm thick samples were grown. They were contacted with In and annealed at 400°C for one minute. This annealing provides local diffusion of In in the sample resulting in good ohmic contacts. Van der Pauw method is used to measure the doping in the layer. This method, based on Hall effect, quantifies the active dopant concentration in the layer and the charge carrier mobility. A charge current is injected in the layer plane, with a magnetic field applied perpendicularly to the sample. The measurement is based on the Lorentz force acting on the charge carriers. The carriers are deviated to one side of the sample and thus a voltage, which depends on the carrier mobility, appears in the direction normal to the current flow. The measure of this Hall voltage permits to quantify the dopant concentration in the sample.

2.6.1 GaInP doping

Up to the concentration needed for our devices, we did not observe any compensation effect for Si-doped GaInP. Thus Si doping calibrations have been straightforward. P-doping has been more challenging.

Two points have to be mentioned. First the lowest p-doping that we could obtain reproducibly is of the order of $10^{17}cm^{-3}$. This is an issue since the p-concentration of interest for PV (often use for the base layer of solar cells) is in the range of $10^{16}cm^{-3}$. In this latter range, the lack of reproducibility is due to a significant n- type residual doping observed for III-P alloys in our growth chamber (an unintentional doping of the same order of concentration, i.e. $\simeq 10^{16}cm^{-3}$). Indeed, III-P samples are contaminated by impurities which are contained in the P source (most probably, sulfur). This non-intentional n-type doping needs to be overcompensated to get a p-type conductivity. This situation which conditions the lowest accessible p-type doping level, is not favorable, indeed too important impurity incorporation is needed to reach the p-doping concentration of $10^{17}cm^{-3}$.

The second point is related to the carrier motilities measured during the Hall calibrations. Figure 2.30 shows the mobility measured for p-type GaInP layer as a function of the carrier concentration (samples grown with the C2N MBE in red, with the IPVF MBE in green).Our results are compared with data from literature (also Be-doped GaInP layers grown by MBE ,in black) [84]. In the $10^{17}cm^{-3}$ range, the hole mobilities are comparable; it seems that the degree of doping compensation in our layers does not degrades significantly the hole mobility. . However, literature data show that mobilities 6 times higher should be accessible by reducing the doping concentration in the low $10^{16}cm^{-3}$.

2.6.2 Influence of the $(Al_xGa_{1-x})_{0.52}In_{0.48}P$ composition on the doping

Then we investigated how the composition of AlGaInP influences the carrier concentration in the sample. In the next chapter, more details will be given on the sought properties for the passivation layer. In this section we just mention that we aim for an AlGaInP material doped in the $10^{18}cm^{-3}$ range. We observed that the doping efficiency depends on the Al content of this quaternary alloy.

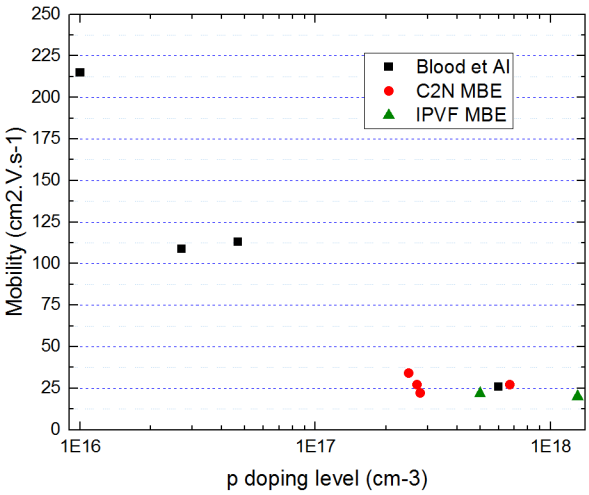

Figure 2.30: Mobility of majority carriers (holes) in Be doped GaInP depending on the dopant concentration.

We grew three different batches of 1-µm-thick $(Al_xGa_{1-x})_{0.52}In_{0.48}P$ samples with different Al compositions and otherwise identical conditions: same substrate temperature, same growth rate and same Be cell temperature in a given batch. The Al composition varied from x=0 to 1, the In content was adjusted to maintain growth rate and lattice match with the substrate.

We observe a strong decrease of the hole concentration when the Al content increases (Figure 2.31). With Be cell temperature of 790°C, the hole concentration is $5.2.10^{18}cm^{-3}$ in GaInP and decreases to $3.8.10^{17}cm^{-3}$ in AlInP.

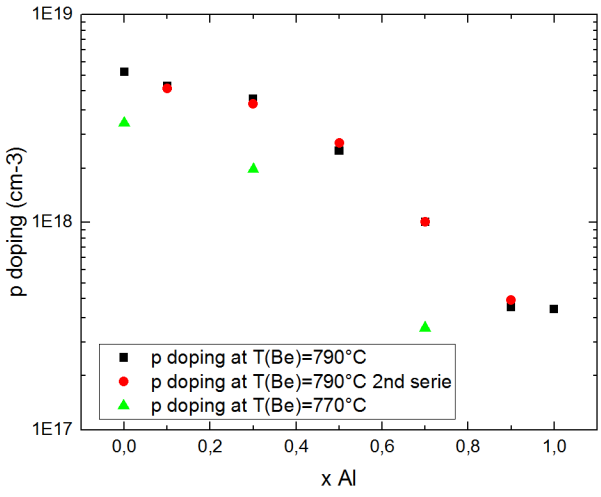

Figure 2.31: Evolution of the doping level in Be doped $Al_xGa_{1-x}InP$ with the Al content x.

When increasing the Al content in the quaternary, the bandgap of the alloy increases too. Thus the difference in energy between the acceptor level and the valence band increases and less carriers are ionized to the acceptor level resulting in a lower carrier concentration measured when increasing the Al content.

Other reason to explain the variation lies on Al and Be affinity with oxygen. Reports suggest that Be tends

to promote O incorporation in phosphide layers when they are grown with a solid phosphorus sources. Using GaP decomposition cell as a source for phosphorus, concentration levels as high as $1.10^{17} cm^{-3}$ in GaInP and $2.10^{17} cm^{-3}$ in AlGaInP was measured [85]. Al is also known for similar effect on Oxygen impurity incorporation, creating DX centers in AlGaAs alloys [86, 87]. The combination of both effect might result in an increasing incorporation of O in the layer with the Al content in the AlGaInP alloy.

In presence of Be, Oxygen forms Be-O complex that causes non radiative traps [88]. Those complex may stop the doping role of the Be atoms associated to Oxygen and therefore reduce the active dopant concentration. Indeed, Be-O are also known for creating deep donor state in GaAs[89] and AlGaAs[90], resulting in Be doping compensation, same effect was observed in MBE grown InGaAs[91].

Increasing incorporation O impurities in AlGaInP with Al concentration may thus cause increasing compensation of the p doping, resulting in the trend displayed Figure 2.31.

Take away messages from Chapter Two:

- MBE is a high vacuum deposition technique that relies on solid sources evaporation. In situ calibration tools ensure reproducible conditions allowing for epitaxy of III-V semiconductors.
- GaInP lattice-matched to GaAs presents various properties depending on the growth conditions. Three types of arrangement can be distinguished: disordered alloy where Ga an In atoms occupy the site III randomly in the crystal lattice; vertically ordered alloys where segregation mechanisms produce thin Ga- rich and In- rich layers alternatively, along the growth direction; alloys with lateral composition modulation (LCM) where surface diffusion and lateral segregation of In and Ga create a periodic modulation of composition.
- Vertical ordering and LCM can be more or less pronounced. They should result in carrier lifetime increase and bandgap reduction.
- Optimal growth conditions in MBE machines were established: a growth temperature around 500°C and V/III ratio of 12 produce good quality GaInP layers.
- GaInP bandgap decreases with increasing growth temperature or by decreasing the V/III ratio.
- When grown at low temperature (450 °C), GaInP exhibits degraded PL properties. PL intensity is weak and at low power, the spectrum is dominated by a transition 30-40 mev below the band gap.
- When grown at V/III ratio below 7, GaInP presents composition modulations of $\pm 1\%$ of In and Ga around the lattice-matched composition. These composition modulations reduce the effective bandgap of the alloy.
- The optimal conditions for GaInP growth in our MBE machine were found to be a growth temperature around 500°C and a phosphorus BEP of $1.4.10^{-5}\,Torr$ at 1 µm/h growth rate.
- STEM and GIXRD suggest that the composition modulations are columnar and periodic, with a period of around 8 nm in the [100] direction and 19 nm along [1-10]. In the AlGaInP quaternary, the modulation period is smaller, 5 nm along [1-10].
-
- In fixed growth conditions, p-type doping level varies with the Al content in $Al_xGa_{1-x}In_yP$ alloy. Assuming an incorporation of Be independent of the Al content in the alloy, we found that Be activation is reduced by increasing this Al content.
- Non-intentionally doped GaInP exhibits a n-type conductivity with a residual carrier concentration in the $10^{16}cm^{-3}$. This residual doping will constrain us to use a minimum level of $2.10^{17}cm^{-3}$ for p doping in our devices to ensure the compensation of the residual donors and thus the p-type conductivity.

Chapter 3

The GaInP single junction Top cell

3.1 Elaboration of the cell

3.1.1 Structure of a GaInP PV cell

A III-V solar cell is usually composed of a stack of different materials, each of them serving a specific purpose in the electrical carrier collection. In this section we detail the structure of cells and explain the use of each stacked layers.

The p-n junction

The core element of the cell is a thick p-n junction absorber. As explained in Chapter 1, for optimal combination with a Si bottom cell this absorber must have bandgap close to 1.73 eV. Therefore, we use GaInP (~1.85 eV) and $Al_{0.25}Ga_{0.75}As$ (1.73 eV) alloys for these layers. The absorber is composed of two layers of the same material, the emitter, n-doped, and the p-doped base.

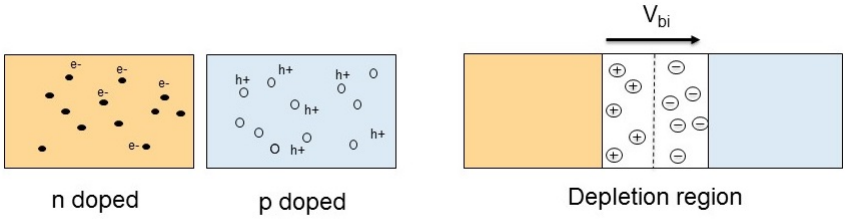

Figure 3.1: P-n junction

At equilibrium, the excess electrons in the n region, respectively the excess holes in the p region, diffuse to the opposite side and leave fixed charges behind. In this so called "depletion region" a difference of potential arises, bending the band structure of the material. The build-in potential (V_{bi}) creates a field driving the minority carriers toward the layer with their polarization (hole toward p-layer, electrons toward n-emitter).

As long as a minority carrier can reach the depletion region (DR), meaning it is generated within a diffusion length from the DR, it will be collected. Thus the electron-hole pairs generated with light absorption can be separated and collected.

As the mobility of minority carriers is usually higher in p-doped material, the emitter is usually thinner than the base. Moreover, in order to place the DR close to the cell surface, where most of the absorption occurs, the emitter is placed on the top of the cells.

The p-n junction thickness is a key parameter, as the performance of the cell will depend on:

- How much of the solar spectrum will be absorbed, inviting to increase the thickness of the absorber.
- The ability to collect the generated carriers, which is favored by maintaining the thickness of the neutrality region below their diffusion length.

Silicon for example has weak absorption and requires thick absorbers, but this is not an issue as the diffusion length in Si is more than twice as long as the required cells thickness (around 160 um)[92, 93, 94]. On the contrary, most of the III-V alloys have direct bandgap, leading to much lower carrier lifetimes and to carrier diffusion length of the order of the μm for GaInP for example [95, 96, 97], but also to much higher absorption coefficient.

Another critical aspect is the doping level of each layer as it determines the band bending. In one hand, low doping level of a given layer increases the thickness of its DR. On the other hand, high doping reduces the layer resistance but also the minority carrier mobility.

The passivation layers

In order to reduce the carrier recombination, especially at the front and rear of the cell, the absorber is sandwiched between higher bandgap passivation layers. The front passivation layer is called the "window"

layer while the rear layer is the "back surface field" layer (hereafter BSF). They both need to be highly transparent and conductive, to prevent undesirable absorption in these layers (because a large part of the generated carriers will be lost due to surface or band to band recombinations) and ensure lateral conduction to the cell contacts. Therefore, they are highly doped and relatively thin (20-30 nm). The band offset with the absorber presents a which impedes the minority carriers from accessing the contact layer, It also generates a local field that repel the minority carriers toward the p-n junction.

To satisfy the lattice matching with GaAs, the material used for the window and BSF can be $Al_{0.53}In_{0.46}P$ with a 2.35 eV bandgap, $(Al_xGa_{1-x})_{0.52}In_{0.48}P$ alloys (hereafter written $(Al_xGa_{1-x}InP$ for simplification) or $Al_xGa_{1-x}As$ alloys. The bandgap of the latter two materials are tunable with their composition [98, 99]. For phosphide based cell, III-V phosphide alloys are preferred because the introduction of AlGaAs requires a growth interruption to switch the group V element. Such an interruption can favor the incorporation of impurities at the critical passivation interfaces. Sometimes, ordering effects are also exploited in order to tune $Ga_{0.52}In_{0.48}P$ bandgap. Hence, alloys with the same average composition but different bandgaps can be used for the base and for the BSF layer [100].

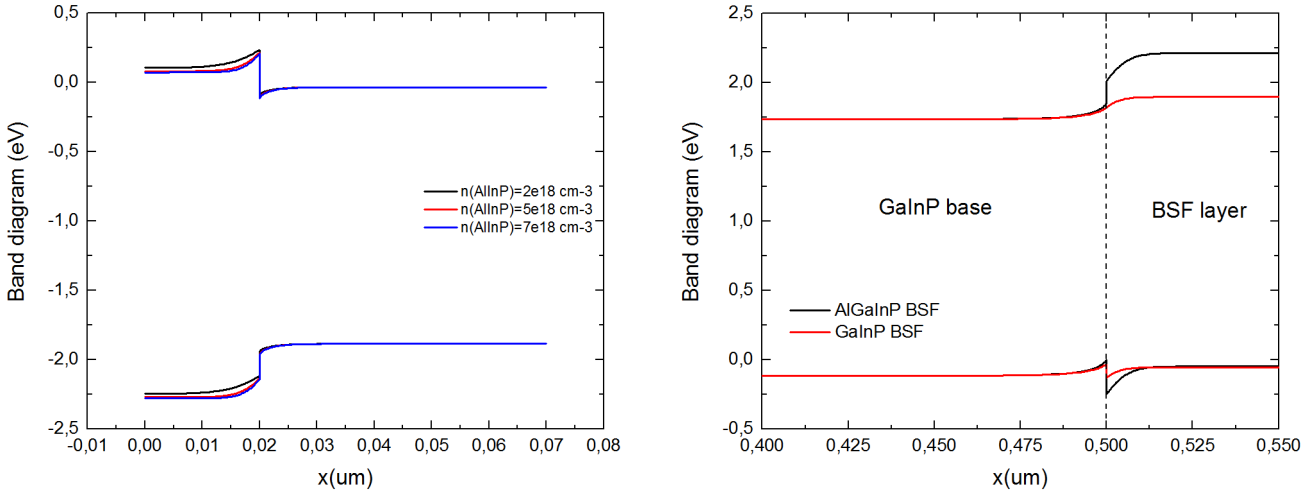

(a) (b)

Figure 3.2: Band diagram for passivation layers. a) Effect of the doping level for an AlInP window. b) band structure for AlGaInP and GaInP back surface field.

Figure 3.2 b) shows the band diagram at the base/BSF interface with a $(Al_{0.5}Ga_{0.5})_{0.52}In_{0.48}P$ BSF and with a completely disordered GaInP BSF. The band diagram were computed with SCAPS, a software for solar cell simulation [101]. The disordered GaInP provides a small potential barrier for electrons, while AlGaInP creates a higher barrier of 0.16 eV, which is more beneficial to the device performance. Ordering effects are weak with MBE growth (Chapter 2); therefore, it cannot be exploited to create an adequate base/BSF heterostructure. We thus decided to use the quaternary alloy.

On the left, the effect of the doping level in the AlInP window is presented. Potential barrier for holes at the emitter/window interface increases with the doping while the barrier thickness for electrons decreases, facilitating tunneling.

Contact layers

Finally highly doped GaAs layers allow the formation of ohmic contacts between the passivation layers and the metallization. It is important that no resistance arises from GaAs/ metallic interfaces. Ideally the work

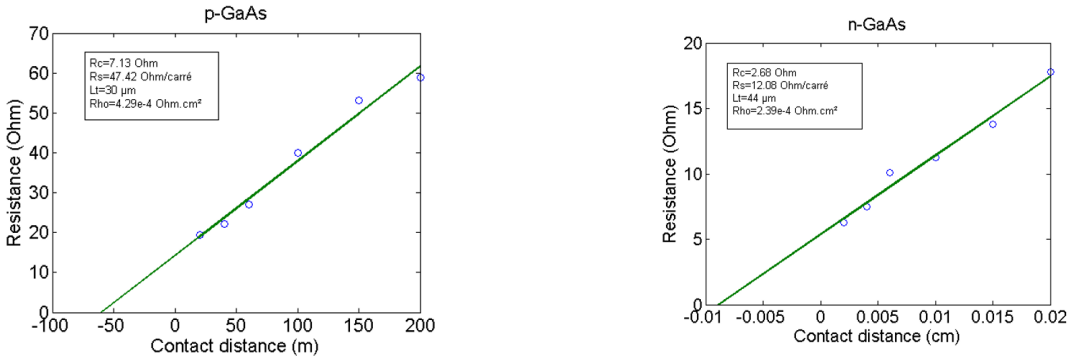

(a) (b)

Figure 3.3: Resistivity measurement for p and n contacts.

function of the metal used provides the required band bending. In our case, the band structure does cause a barrier for the carriers. It is the doping of the contact layers that makes this barrier so thin that the carriers simply tunnel through it for collection.

We will not study in details this aspect of the cells because it was developed prior to this project for GaAs solar cells and it is not a critical aspect of the cells anymore. Nevertheless, Figure 3.3 shows resistivity measurements for our metallic/GaAs contact. The measurements were performed on GaAs doping characterization samples, via Transmission Line Matrix method (TLM). The TLM method consists in evaporating several metal contacts on the GaAs with different spacing between each contacts. Measuring how the resistance varies with the contact spacing, the specific resistivity of the metal/GaAs interface can be extracted. Resistivity of $4.29.10^{-4}$ $\Omega.cm^{-2}$ for the Ti/Au p-contact and $2.39.10^{-4}$ $\Omega.cm^{-2}$ for the n-contact (Ni/Ge/Au based) were measured. If these values are two orders of magnitude above what can be achieved for metallic contacts on GaAs [102, 103], it is satisfying for us as this resistivity is negligible in comparison to the resistivity of the cells (around 0.1 $\Omega.cm^{-2}$).

Note that this conduction layer, which would cause detrimental absorption, is removed from the non-metalized area during the process.

Typical structure

Figure 3.4 displays the structure of usual III-V cells. In this section the absorber is made of GaInP. Typically composed of a thin emitter, around 100 nm, n-doped in the $10^{18}cm^{-3}$ range while a thick base completes the solar spectrum absorption with a thickness around 1 μm and a lower p-doping in the $10^{17} - 10^{16}cm^{-3}$ range.

They also comprise thin passivation layers 30-20 nm for the window, 50-20 nm for the BSF, doped in the $10^{18}cm^{-3}$ range.

Table 3.1 details some example from the literature. Note that the record GaInP single junction does not have a conventional structure: NREL could profit from a high material quality (high mobilities and lifetimes), hence they could grow a thick emitter. Reaching 20.1% with their rear junction solar cell with a gold back mirror.

As we do not benefit from such material quality for n-doped GaInP we focused on the more "classic" approach. Within this chapter, we will detail the work on the structure of the cell in order to obtain the best efficiency out of our material quality.

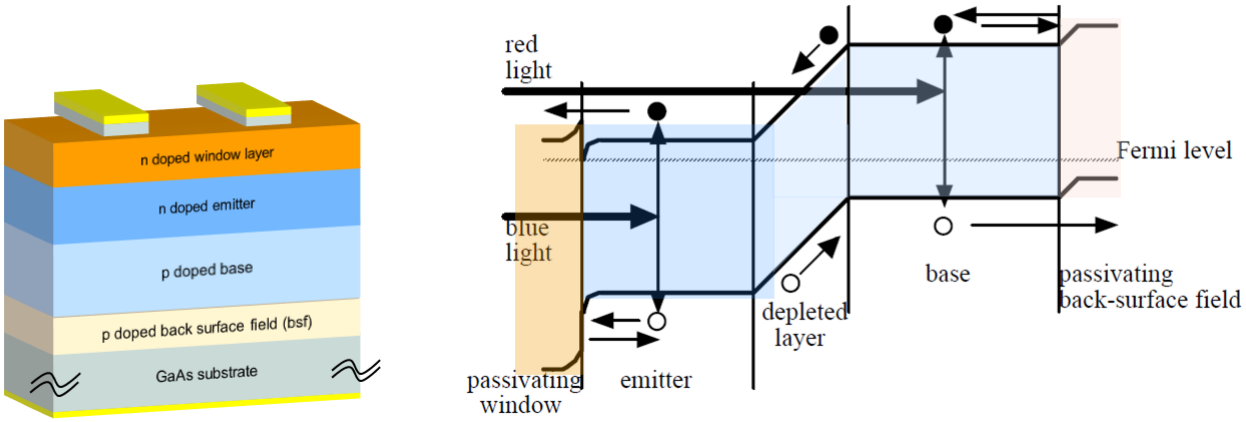

Figure 3.4: Structure of a III-V cell and associated band diagram detailing carriers path to contacts.

		BSF			Base		Emitter		Window		
section	Efficiency (%)	Thickness (nm)	p doping (cm^{-3})	Alloy	Thickness (nm)	p doping (cm^{-3})	Thickness (nm)	n doping (cm^{-3})	Thickness (nm)	n doping (cm^{-3})	Alloy
P.Dai et al	16.6	30	$2\ 10^{18}$	AlGaInP	750	$5\ 10^{16}$	80	$2\ 10^{18}$	20	$4\ 10^{17}$	AlInP
Masuda et al	-	300	$2\ 10^{18}$	AlGaInP	1500	$1\ 10^{17}$	100	$2\ 10^{18}$	30	$2\ 10^{18}$	AlInP
Ikeda et al	15.5	50	$3\ 10^{18}$	GaInP	700	$1.5\ 10^{17}$	50	$3\ 10^{18}$	30	$2\ 10^{18}$	AlInP
Geisz et al	18.4	20	-	AlGaInP	1000	$1\ 10^{16}$	100	$2\ 10^{18}$	20	-	AlInP
Geisz et al	20.8	20	-	AlGaInP	40	-	1000	$5\ 10^{17}$	20	-	AlInP

Table 3.1: Structure of the best GaInP single junction solar cells.

3.1.2 Process for cell fabrication

In this section, we describe the process flow from bare III-V stack to a functional solar cell. We will describe later the additional steps needed for the cell transfer, in the section 3.4.1 that dwells on the cell integration on Si. Figure 3.5 illustrates the different steps of the process.

First, the cell stack is grown by MBE on (100) GaAs p-doped wafer. The precise growth characteristics are detailed in Chapter 2. Phosphide layers are grown at 500°C, arsenide at 550°C. The two-inch wafer is then cut in smaller pieces, specific cleanroom process permits to make multiples cells on a single piece. The choice of the techniques used in the process are meant to reduce the process time and cost. Wet etching is therefore preferred to dry etching techniques (RIE, Plasma etching...).

The first process step consists in deoxidation in diluted HCl to remove native oxide from top GaAs contact. Negative photolithography allows to cover the surface of the sample and to leave only the front-contact grid free from the photo-resist. For this lithography, AZ 5214 resist is spin-coated on the sample and exposed twice to UV light, once through a mask patterned with the front-contact grid. Development in a MIF 826 solution completes this lithography step by removing the resist protected by the mask.

The metallic contact, a Ni/Ge/Au/Ni/Au (4/10/60/110/10/200 nm) stack, is deposited via metal evaporation. The patterned photo-resist is dissolved in acetone, allowing to lift-off the non –desired metal film covering the resist (step 4 Figure 3.5). The top GaAs contact layer, which is not protected by the metallization, is etched with citric acid (in order to avoid parasitic absorption before the GaInP absorber).

A second lithography step defines cells areas, and isolates one cell from the others. The AZ5214 resist is kept above the cells and removed from the zones in between them, it is then hardened with a hot plate curing (step 6). The sample, where all cells are thus protected, is soaked in a HBr based solution. The solution etches all phosphide layers and isolates the cells to prevent any shunt. The back contact Ti/Au (20/200 nm) is evaporated on all the back surface of the p-doped substrate.

When Anti-reflection coating (ARC) is added the first photo-lithography step is repeated to protect the top contacts and 70 nm of SiNx is sputtered on the cells. **If not stated otherwise, characterization results of the structures studied in the next section is based on the averaging of the measurement of 10 to 20 cells processed on a piece of 2-inch wafer.**

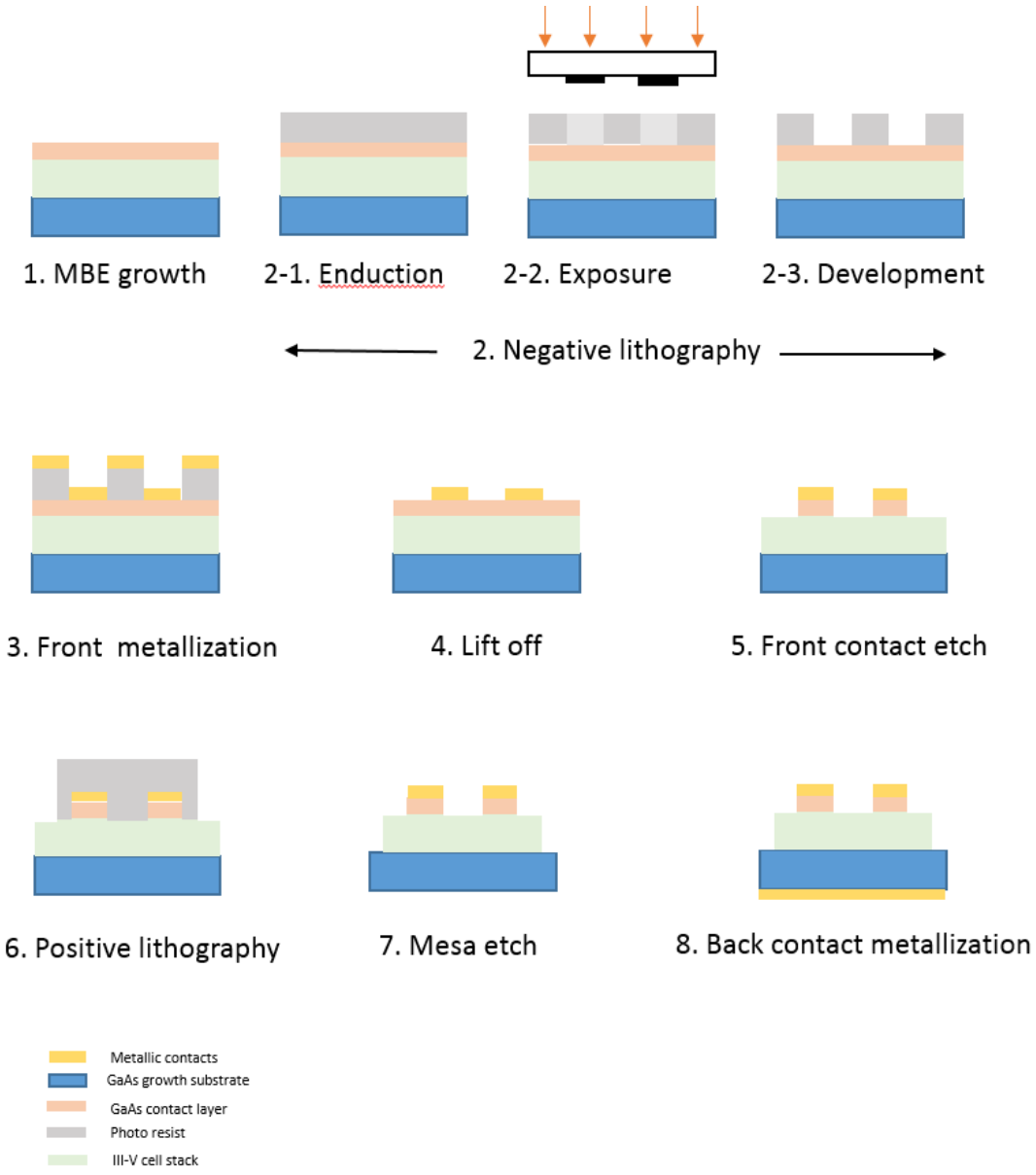

Figure 3.5: Process flow for cells.

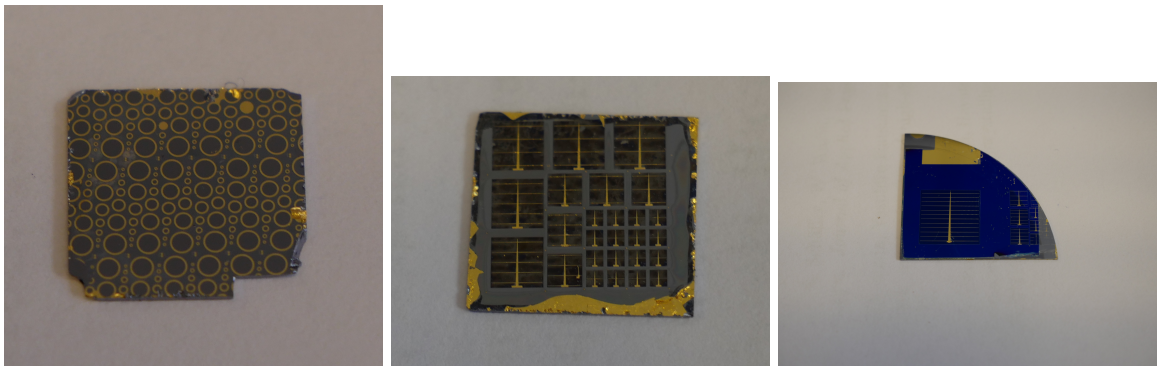

(a) (b) (c)

Figure 3.6: Examples of samples after process. a) Circle cells b) square cells c) 1 cm^2 cell with ARC.

3.2 Cell structure study

3.2.1 Cell characterization

In this section, the characterization that serves to evaluate the cells is briefly detailed. It relies on two methods, the determination of the I-V characteristic of cells (J-V when normalized with the cell surface) and the determination of their spectral response with the EQE.

P-n junction model is used to evaluate the cells. In the dark the Shockley equation gives a first relation between the current density J and the voltage V.

$$J = J_0[exp(\frac{qV}{nkT}) - 1] \tag{3.1}$$

Where k is Boltzmann constant, **q** elemental charge, **T** is the temperature, **n** the ideality factor of the diode and **Jo** the saturation current density. When exposed to light a photocurrent density **Jph** flows in the opposite direction of Jo. One must also consider parasitic resistance that arises from the non-ideality of the cells, giving:

$$J = J_0[exp(q\frac{V - JRs}{nkT}) - 1] + \frac{V - JRs}{Rsh} - J_{ph} \tag{3.2}$$

Here **Rs** is the series resistance, arising from resistive losses during the vertical conduction to the metallic contacts. It gives insight on the metal/semiconductor interface quality but also on conduction issues in the semiconductor layer. A too low doping level would increase the material resistivity, leading to a Rs increase. **Rsh** is a parallel resistance, it corresponds to leakage through the edges of the cell. For example, it can be impacted by step 7 of the cell process (in Figure 3.5) and it reveals the quality of the mesa etching or the ARC and its ability to passivate the edges.

A low Jo value measured with a J-V characteristic in the dark indicates a good quality of the p-n junction. Low Rs and high Rsh are also sought, they can be extracted from an IV measured under illumination or in the dark. Figure 3.7 show how these resistances impact the J-V characteristic of a solar cell.

The standard J-V characterization method consists in measuring the intensity delivered by the cells for given biases. The measure must be taken at 25°C and under a solar simulator delivering 100 $mW.cm^{-2}$ and reproducing the AM1.5G spectrum (solar spectrum at earth surface). In the laboratory, an Oriel LCS-100 simulator provides this illumination. The current variation with the applied voltage is measured with a Keithley source meter that contacts cells with four-point probes. The same measure can be performed in the dark in order to get the reverse saturation current. This measure highlights three important characteristics of the cell (Figure 3.7): **Jsc** the short-circuit current density, **Voc** the open circuit voltage and the maximum power point corresponding to a **Vmpp** and **Jmpp**. The fill factor **FF** is defined as $FF = \frac{V_{mpp}J_{mpp}}{V_{oc}J_{sc}}$, it quantifies the squareness of the J-V characteristic. This parameter is affected by the resistance values. Figure 3.7 shows how resistances change the J-V characteristic shape.

Then the efficiency of the solar cell, which is the ratio between the generated power density from the cell and the incident light power density is determined as:

$$\eta = \frac{V_{oc}J_{sc}FF}{P_{in}} \tag{3.3}$$

Another important cell characterization is the external quantum efficiency (EQE) measure, it characterizes the spectral response of the cells and is another way to measure the Jsc. For each wavelength, the EQE gives the probability that the energy of an incident photon will be collected as an electron-hole pair. Assuming that in our cells, all the photons with energy higher than Eg are absorbed, the Internal Quantum Efficiency can be determined with the measure of the reflection (R) on the cell surface. $IQE = \frac{EQE}{1-R}$. The IQE treats the collection of carriers generated by photons absorbed in the cell, whereas EQE dwells with both the ability of the cell to absorb photons and collect the generated carriers. Indeed, in the IQE the contribution of reflected photons is removed and only absorbed photons are considered. The relevance of the EQE lies in the fact that one can assess the quality of the photovoltaic conversion along the depth of the cell. From Beer-Lambert law, we know that a photon with a given wavelength has a specific absorption depth and is then characteristic of a given depth in the cell.

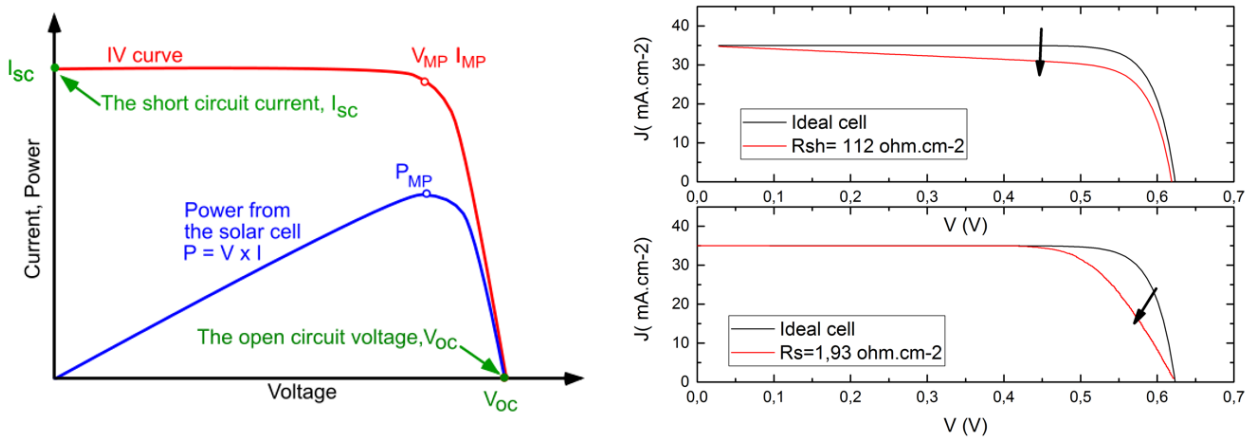

Figure 3.7: On the left, one-sun characterization example with important points displayed. On the right, resistance effect on the J-V curve. Ideal cell is a 1 cm^2Si cell with $R_s = 0\Omega.cm^{-2}$and $R_{sh} = 1.10^4\Omega.cm^{-2}$(Data from pveducation.org)

$$L(\lambda) = L_0(\lambda).e^{-\alpha(\lambda).x} \tag{3.4}$$

where L is the light intensity, α is absorption coefficient and x the depth within the semiconductor layer.

We can then evaluate the quality of the different layers of our structure based on the ability of the cell to absorb photons at different wavelengths. As detailed in Figure 3.8, short wavelengths relate to front surface response which is affected by surface recombination while long wavelengths EQE results from bulk collection and rear recombinations.

The set-up that serves to measure the EQE has a Xenon light source, the light passes through a Triax monochromator and is focused on the cell (a few hundreds of μm). The cell is contacted with a four-point probe connected to a Keithley source meter. The photo-current generated by the cell is measured for each wavelength. The comparison with the spectral response of a silicon photodiode, with calibrated spectral sensitivity allows to determine the EQE of the cell .

$$J_{sc} = q \int_0^{\infty} EQE(\lambda).\Phi_{AM1.5G}(\lambda).d\lambda \tag{3.5}$$

Equation 3.5 expresses Jsc can as a function of the spectral EQE(λ), where $\Phi_{AM1.5G}(\lambda)$ is the photon flux of the solar spectrum AM1.5G , q is the elemental charge. In our case an integration from 300 nm to 750 nm is sufficient as few photons compose the solar spectrum under 300 nm and no absorption occurs below the targeted bandgap.

3.2.2 Emitter thinning: improvement of photon collection in the front of cells

Figure 3.8 exhibits that III-V cells usually perform better in the bulk than in the front. Indeed, for most of the cells reported, the EQE shows a steep drop at energy close to their bandgap, while the increase of the EQE at high energy is much slower. This suggests that for this type of cells, optimization of the front of the structure can have significant impact on the photovoltaic conversion. Simulations from Kurtz et al [100] supports this assumption (Figure 3.9): the emitter absorbs most of the photons above 2.7 eV. Complementary absorption occurs in the depleted region and the base which has the most important contribution close to the bandgap energy.

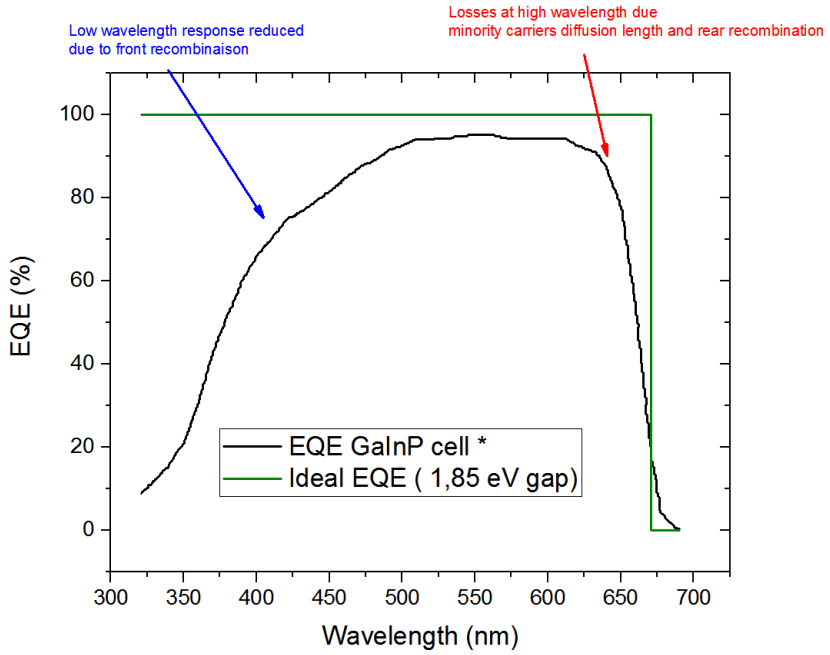

Figure 3.8: EQE of GaInP cell [104] and ideal EQE expected when no reflection occurs at the surface of the cells and carriers do not recombines in the bulk absorber.

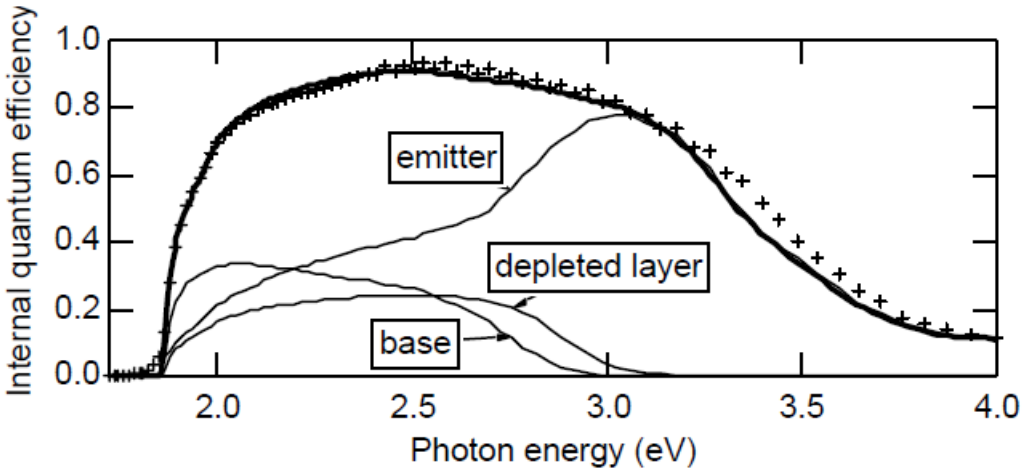

Figure 3.9: IQE of the different zones of a GaInP cell, from [100]. Crosses experimental data, lines model fitting the data and expliciting the contribution of each regions of the cell

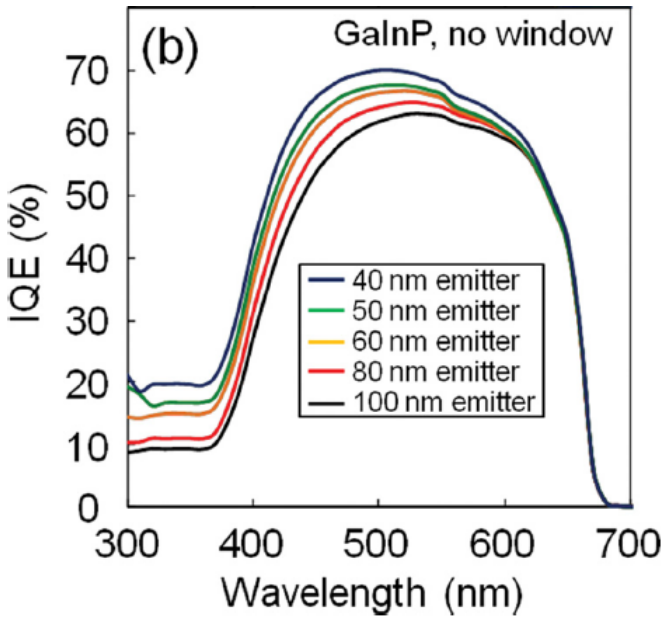

Figure 3.10: Effect of emitter thickness on GaInP cell IQE, from [105]

Therefore, we studied how to maximize the blue response of the cells grown in our conditions. While there is a consensus on a thickness of 1µm for the absorber, various thicknesses are used for the emitter. 100 nm is commonly used, but some laboratories use an emitter as thin as 50 nm.

An interesting work from Masuda et al [105] highlights the interest of reducing the emitter thickness for MBE-grown cells. For cells without window layer, they showed that thinning the emitter, the IQE of cells increases, especially for small wavelengths (see Figure 3.10). Thinning the emitter, the depleted region is located closer to surface. Since a strong absorption occurs in the emitter, the carrier concentration is particularly high in the front of the cell. Since the depleted region expansion in the emitter is dictated by the doping levels of the p-n junction, the thinner the emitter, the more significant is the depleted region share . Considering a p-n junction with n=$4.5.10^{17} cm^{-3}$ and p=$2.10^{17} cm^{-3}$, the depletion region expands 24 nm into of the emitter layer. For a 100 nm thick emitter, the photocarriers diffuse "randomly" within 76 nm of the emitter, while for an emitter thickness of 50 nm this zone is reduced to 26 nm. This minimizes drastically the photocarriers recombination in the front of the cells, as more photons are absorbed in the depletion region where carriers are drifted by an electrical field.

3.2.3 Application of the emitter thinning method to our material

This optimisation highly depends on the quality of the materials in use. Once again, a good example showing the influence of material quality on the optimization of the cell structure is the record GaInP cell elaborated by Geisz et al [48]. . In their case, n-GaInP is of better quality than p-doped GaInP: the optimal strategy for them was to bring the p-n junction close to the rear of the cell, which is thus composed of a thick emitter and a thin base. We performed simulations to forecast the benefit of a thin emitter. A model was developed in order to fit the performance of a cell from the literature [104]. A correct fit was obtained despite a slight difference in Jsc due to a lack of input on the ARC layer. We then changed a few parameters of the model with input from our experimental calibration, using mobilities obtained by van der Pauw measurements and reducing the carrier lifetime.

The results predict a weak impact on the Voc, but a strong increase of Jsc for the reasons explained earlier. While the fill factor decreases slightly with emitter thinning, the overall efficiency increases. In our case, it is expected that thinner emitter cells will perform better than cells comprising a 100 nm thick emitter (Figure 3.11).

Two structures were processed, (Figure 3.12). Their characterization confirms the simulation results. As

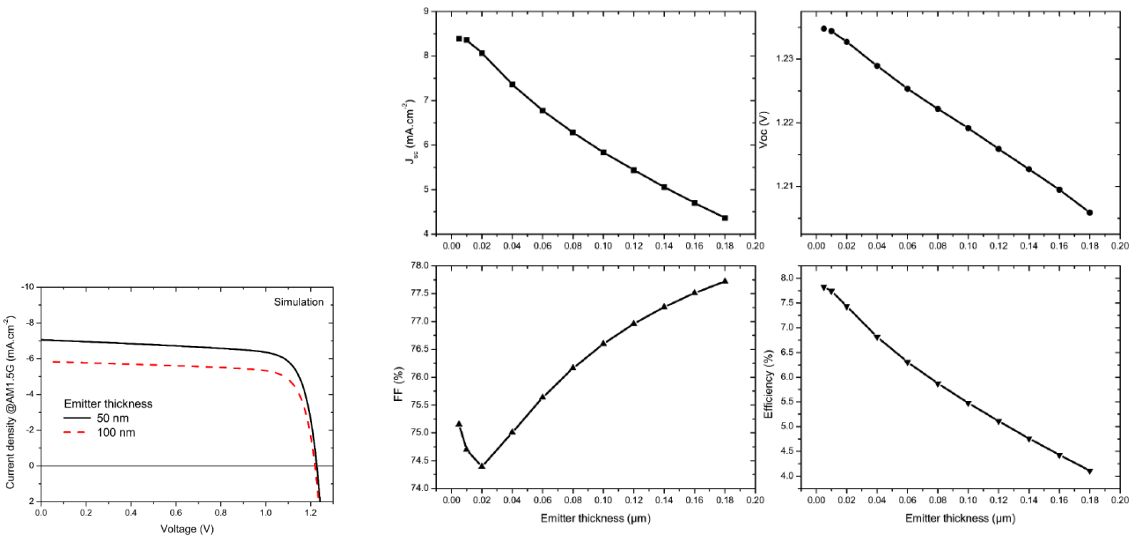

(a) (b)

Figure 3.11: Simulation results on the emitter thickness. a) IV characteristics simulated for 50 nm and 100 nm emitter thickness. b) Variation of the figure of merit of cells with the emitter thickness.

Sample	Jsc ($mA.cm^{-2}$)	FF	Voc (V)	Efficiency
100 nm emitter	5.5	0.757	1.19	4.97
50 nm emitter	6.15	0.728	1.11	4.99

Table 3.2: Mean characteristics of the cells depending on emitter thickness

shown in Figure 3.12, the cells with a 50 emitter have a better external quantum efficiency in the whole absorbed spectrum, the difference in EQE being the largest around 450 nm. Table 3.2 highlights the increase of current provided by the thinning, but the two sets of cells have similar efficiencies due an unexpected drop of the Voc for the 50 nm emitter cells. The Voc and FF drop is not due to the design of the structure nor to the quality of the sample; this degradation is attributed to an increase of shunt resistance caused by the process. The reader is reminded that the cells from a single batch are fabricated from a small piece of a 2-inch sample and they undergo the same process. Another piece from the same wafer processed differently exhibit good characteristics, as presented in the next section.

We carry on and grew a cell with a 25 nm emitter to see if further thinning would be beneficial, as the modelling suggests. This attempt was done on passivated cells grown in the IPVF compact 21, thus another cell with 50 nm emitter was grown in the same conditions for comparison. The two cells compared here, are better optimized than the two cells above, thus they have much better efficiency.

For this batch, all parameters degrade when thinning the emitter to 25 nm, including the Jsc that was supposed to increase with this modification of the emitter. With only 25 nm emitter, we may have transferred significant absorption from the depleted region into the base, this is less favorable for the carrier collection. Thus a thickness of 50 nm is a good compromise for the emitter.

Sample	Jsc ($mA.cm^{-2}$)	FF	Voc (V)	Efficiency
50 nm emitter	9.05	0.804	1.28	9.08
25 nm emitter	8.53	0.766	1.26	8.18

Table 3.3: Results from a second set of cells and influence of emitter thickness

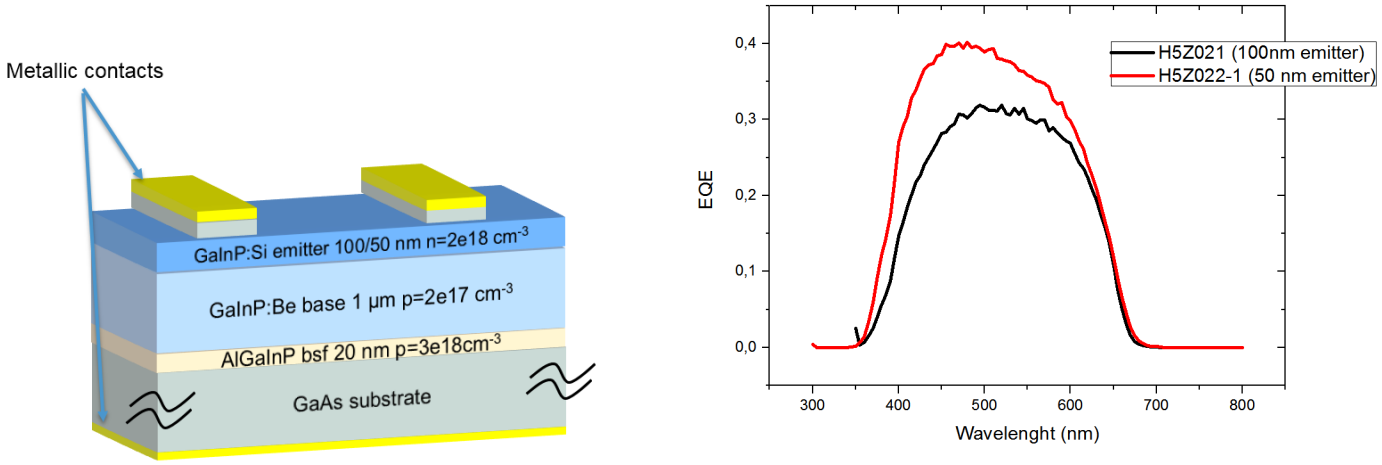

(a) (b)

Figure 3.12

3.2.4 Passivation and window layer

Optimizing the window layer is another important step toward the improvement of the blue response of the cells. As explained in section 3.2.2, we focus on III-P alloys lattice-matched to GaAs with bandgap higher that of GaInP.

Tuning the composition of AlGaInP alloy, one can impact several properties of the window layer. First aspect is the AlGaInP/GaInP band offsets. In our n-p configuration the window layer must provide a barrier for holes and a local field repelling them towards the n-p junction. Figure 3.13 highlights that the more Al content in the alloy, the larger the valence band offset [106]. This explains why AlInP is often chosen for this use in the literature.

Second important aspect is the ability to dope the layer. At least $1.10^{18} cm^{-3}$ concentration is required in our case in order to provide the desired band bending at the $Al_xGa_{1-x}InP/$ GaInP interface and good lateral conduction to the contacts. This is essential to minimize the series resistance.

It is known that the more Al concentration in quaternary AlGaInP alloys, the more difficult the doping of this compound [105, 107]. At first, we were not able to grow n-AlInP layer with the targeted doping concentration for using it as a window layer.

Therefore, we first grew a PV cell structure with an AlGaInP window (structure detailed in Table 3.5) . Two different pieces of sample were processed, one with the normal process and the other with an additional etching step to remove the window at the cells surface (the 50-nm-emitter cell used for emitter thickness study in the previous section). We could then illustrate the impact of the window layer on the passivation of the front surface and on cell performances.

The AlGaInP layer provides an increase of 2% efficiency. Without window, the cells have an average 6.15 $mA.cm^{-2}$ current density, a 0.728 fill factor, a 1.11 V open circuit voltage and thus a 4.99% efficiency. A AlGaInP passivation layer increases all these parameters: 7.6 $mA.cm^{-2}$ for Jsc, a 0.768 FF, 1.18 Voc and 6.89% efficiency. While the 2% increase in efficiency is overestimated since the Voc of cells without window is most probably underestimated for reason explained earlier (in section 3.2.3), the expected current improvement is indeed present.

Since we did not etch the window layer underneath the metallic/GaAs contact, we can reasonably assume that the barrier for current collection to the metallic contact is identical in the two samples. Thus, the effect which is observed must be related to minority carriers repel toward the p-n junction, as well as a diminution of the carrier concentration at the front of the cell. Moreover, placing AlGaInP on top of GaInP, reduces considerably the surface recombination velocity of the emitter region. In conclusion, the significant increase

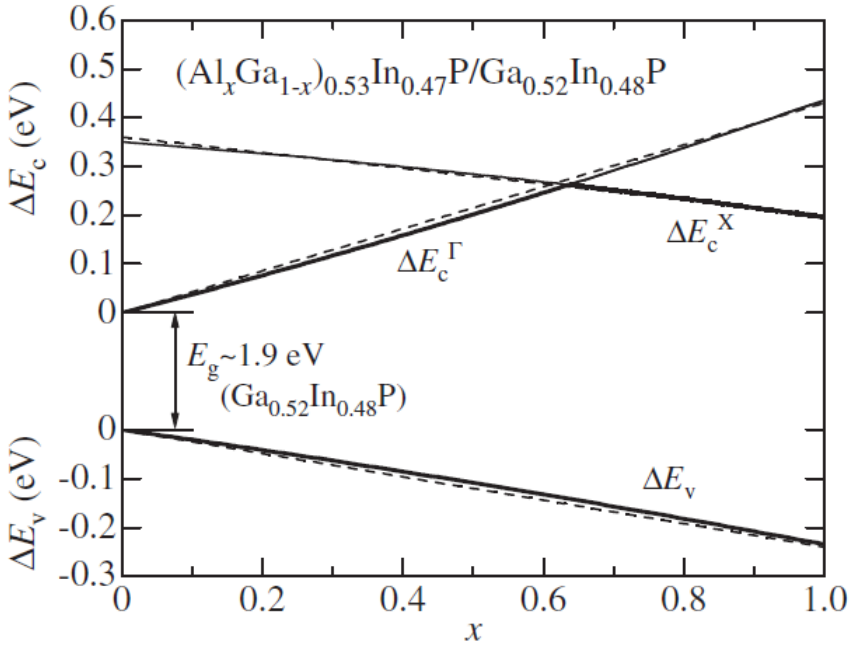

Figure 3.13: AlGaInP quaternary alloy properties of interest for the window layer. Band off-set between GaInP and $(Al_xGa_{1-x})_{0.52}In_{0.48}P$ alloy depending on the Al content x.[106].

Sample	Jsc ($mA.cm^{-2}$)	FF	Voc (V)	n
No window *	6.15	0.728	1.11	4.99
AlGaInP window	7.60	0.768	1.18	6.89
AlInP	8.15	0.784	1.23	7.87
AlInP and SiNx ARC	10.68	0.784	1.243	10.42

Table 3.4: Mean parameters for the different batches on the window study

of the Jsc can be attributed to a drastic decrease of the carrier recombination at the cell surface.

Even though the absence of anti-reflection coating was deposited on the cells limits the cell absorption, the collected current remains surprisingly low. Reflectance measurement performed on 1-µm-thick calibration layers (Figure 3.15) suggests that increasing the Al content in the alloy would favor more absorption because light reflection at the cell surface decreases in a wavelength range where the EQE of the cells is maximum, around 400 nm (see Figure 3.15 a)). Moreover, the band configuration at AlInP/GaInP interface is ideal. Gudovskikh et al report that at the AlInP (n=$5.10^{18}cm^{-3}$)/GaInP(n=$2.10^{18}cm^{-3}$) interface, electrons face only a 0.15 eV barrier, that the valence band bending effectively provides an electric field repelling the holes from the interface and that those properties are not sensitive to the interface defect density[99].

To solve the problem of AlInP n-type doping mentioned before, we used the Si dopant source beyond the temperature limit that was fixed. This allowed us to obtain $3.10^{18}cm^{-3}$ doping in AlInP. Another solution would have been to reduce the growth rate, but it requires a longer growth interruption to change the Indium cell temperature. Moreover, we want to keep the growth rate at 1 μm /h because it is an important factor contributing to the cost of III-V cells. Indeed, much efforts are dedicated to fasten the growth rate of III-V cells [108]. In Figure 3.15, the light reflection on the cell surface was indeed reduced by replacing the window material with AlInP. This translates into a better EQE at low wavelengths and therefore an increase of the short circuit current. The introduction of this AlInP window resulted in one additional percent of efficiency. Table 3.4 gathers the mean parameters for the three batches of this study.

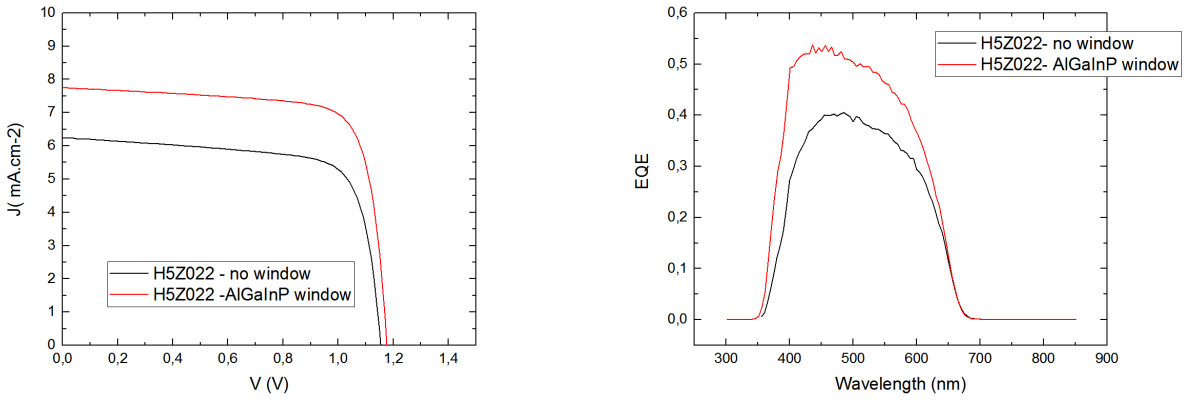

(a) (b)

Figure 3.14: AlGaInP window effect on GaInP cell performance

Regarding the back surface field layer, the rear passivation layer, less impact on the carrier collection is expected. With a 1-μm-thick GaInP layer, most of the photons of energy higher than the bandgap will be absorbed away from the rear of the cell. Thus less minority carriers are generated close to the BSF layer than in the front of the cell. Thus the role of the former is less critical than that of the window layer: carrier recombination at the window interface impacts not only the blue response, but also the efficiency on the whole absorbed spectrum while the BSF layer only impacts the red response of the cells [100].

It is noteworthy that the Al content has a drastic impact on the Be doping efficiency, as illustrated Chapter 2, and that it is difficult to grow highly doped p-AlInP. Moreover, at the AlInP/GaInP interface, majority carriers (holes) have to face a non negligible 0.54 eV barrier (see band diagram Figure 3.16) [99] and the electric field created at the interface would drive the few electrons generated at the rear toward the p-contact. AlInP is not a suitable chose for BSF in our case.

Then, we tested two compositions of the AlGaInP alloy, at 30% and 50% Al concentration. As expected and for additional reasons linked to the base that will be explained later, we did not notice any significant impact of the composition of the BSF layer on the cell efficiency and we chose a 30-nm-thick BSF layer with a 50% Al content doped at $3.10^{18} cm^{-3}$.

In order to compare our results with those reported in the literature, the best cells were then improved with an anti-reflection coating (ARC), which is not the optimal ZnS/MgF_2 ARC. We use a 70 nm SiNx ARC deposited by sputtering, the best solution available in the laboratory. Thereby, the cell absorption was improved, providing a 31% raised of the Jsc. The cell with AlInP window and ARC has then a 10.42% mean efficiency.

Performing STEM on a cell structure in Chapter 2, the passivation layers were investigated. We mentioned that EDX method can give a good estimation of the relative concentrations of each element in the layers. The passivation layers interfaces with GaInP and the GaAs contacts layer were characterized with this technique.

Figure 3.17 and 3.18 shows that these interfaces are not abrupt but present composition gradients. It is particularly striking in the window layer (Figure 3.18). Starting from the GaInP interface, the window has a 15 nm gradient before reaching an $(Al_{0.75}Ga_{0.25})_{0.5}In_{0.5}P$ composition instead of the nominal AlInP. The GaAs/window interface also presents a composition gradient; In, P and Al are still present in the first 10 nm. The HAADF image of the AlInP window at high magnification (Figure 3.3.19) confirms the presence of a composition gradient in the window layer.

This can be due to segregation effects. During the growth of these alloys, the bigger atoms tend to float at the surface of the sample. This surface segregation effect was widely reported for In during the growth of GaInAs on GaAs [109, 110]. When switching off the Ga and starting the Al for the growth of the window, the Ga atoms that still diffuse on the surface, keep on "floating" while Al starts to incorporate. Al incorporates faster and the incorporation of the remaining Ga atoms is delayed, causing the compositiongradient. Same

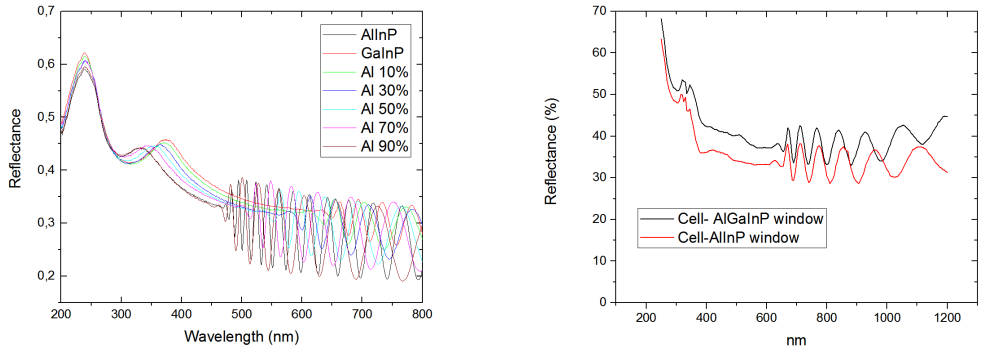

(a) (b)

Figure 3.15: a) Effect of the $(Al_xGa_{1-x})_{0.53}In_{0.47}P$ composition on the reflectivity of a 1-μm-thick layers. b) Reflectance measured on solar cell with $(Al_xGa_{1-x})_{0.53}In_{0.47}P$ and AlInP window. The cell passivated with AlInP benefits from the blue shift of the reflectance peak when increasing the Al content observed in a).

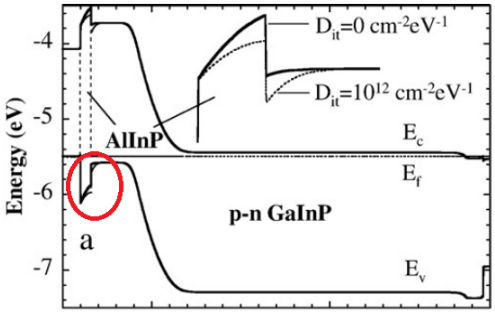

Figure 3.16: Band diagram of a p-AlInP/p-GaInP/n-GaInP structure. Non-negligible barrier appear in the red circle "a", disturbing holes collection.

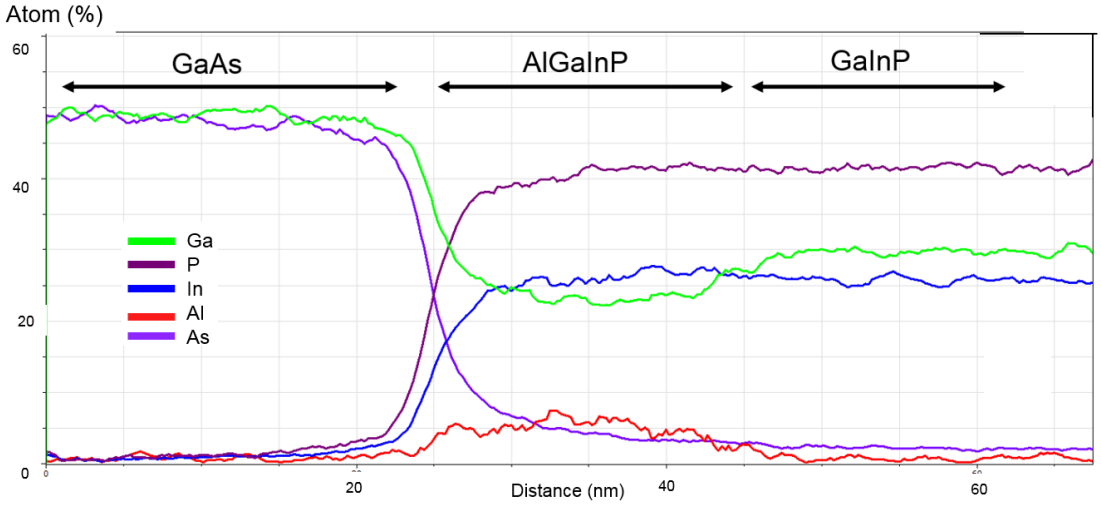

Figure 3.17: EDX profile at the rear of a solar cell. Concentration of constituents across the GaAs/ AlGaInP BSF/ GaInP stack.

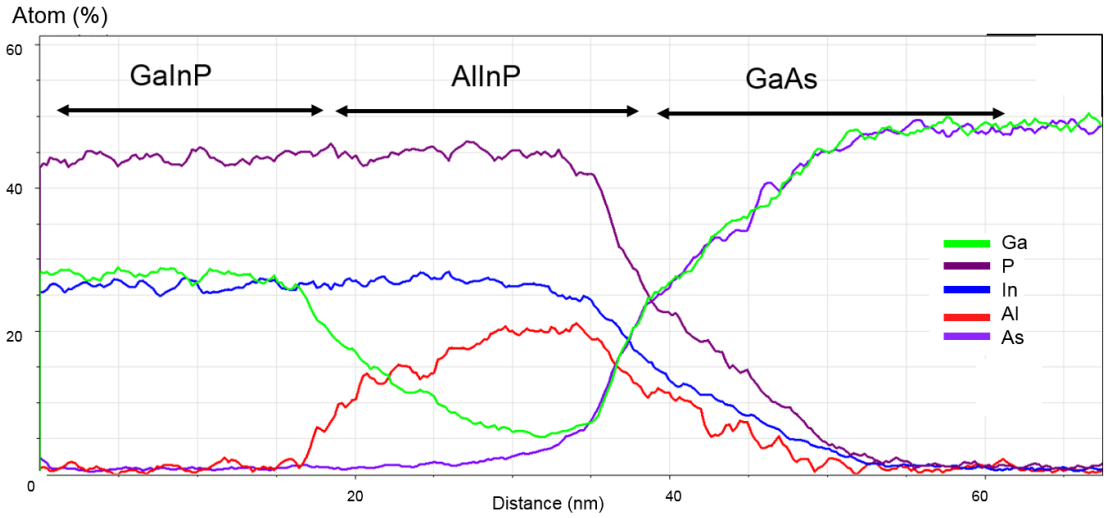

Figure 3.18: EDX characterisation at the front of a cell. Concentration of the constituents across the GaAs/AlInP window/ GaInP stack.

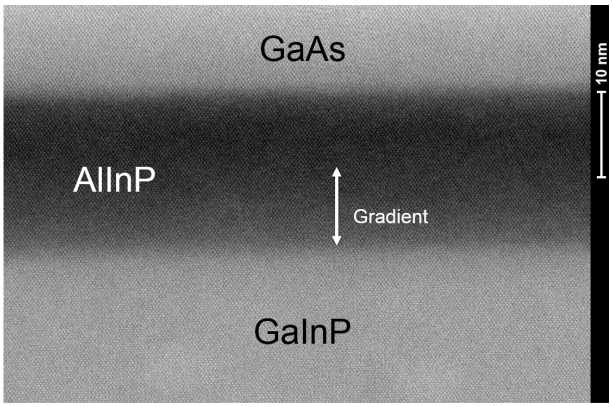

Figure 3.19: HAADF image of the AlInP window of the cell. High magnification on the GaInP/AlInP/GaAs stack.

happens with In while growing the GaAs contact.

Nevertheless, the expansion of the gradient seems surprisingly long length (10 nm) and the presence of a residual As content in the AlInP window (that cannot be explained by residual the As pressure in the MBE which has no reason to increase during the growth of the AlInP layer), would require further investigations to clarify the causes of the gradients observed. Another possible origin would be an important interface roughness in the direction perpendicular to the sample view in Figure 3.19. Indeed, a strong interface roughness in the depth of the sample would be probed as a region of graded composition since EDX or HAADF measurements are averages on atomic columns.

We evaluated the impact of this gradient (whether real or not) on the band diagram at the window/emitter interface, a 16 nm linear gradient in composition was added in our interface simulation with Scaps. We see in Figure 3.20 that the band diagram is in fact more favorable to the hole repel and that the barrier for electron is smaller. Thus unavoidable segregation effects during growth should not degrade the electrical properties of our cells.

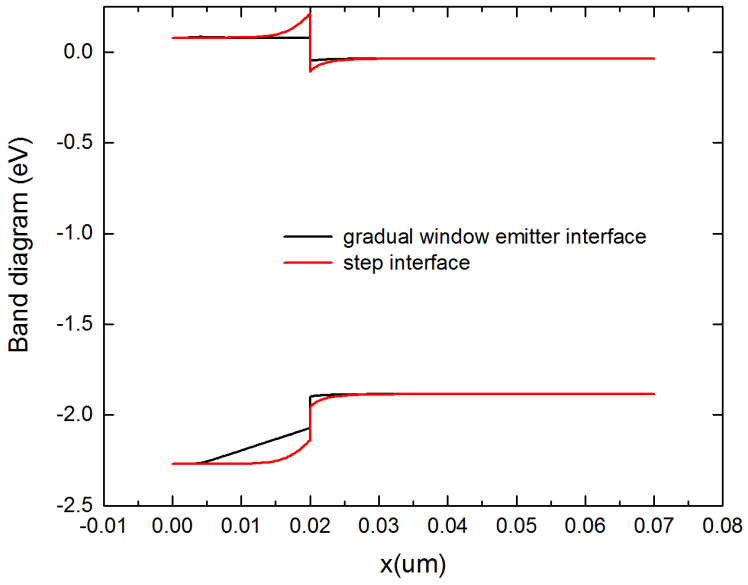

Figure 3.20: Simulation of the Window/emitter interface with a 16 nm composition gradient between GaInP and AlInP.

		AlGaInP BSF			Base		Emitter		Window		
section	structure	Thickness (nm)	p doping (cm^{-3})	xAl	Thickness (nm)	p doping (cm^{-3})	Thickness (nm)	n doping (cm^{-3})	Thickness (nm)	n doping (cm^{-3})	Alloy
3.2.3	100 nm emitter	20	$3\ 10^{18}$	0.3	1000	$2\ 10^{17}$	100	$2\ 10^{18}$	-	-	
3.2.3	50 nm emitter	20	$3\ 10^{18}$	0.3	1000	$2\ 10^{17}$	50	$2\ 10^{18}$	-	-	
3.2.3	50 nm emitter - reference cell	20	$3\ 10^{18}$	0.5	1000	$2\ 10^{17}$	50	$2\ 10^{18}$	20	$5\ 10^{18}$	AlInP
3.2.3	25 nm emitter	20	$3\ 10^{18}$	0.5	1000	$2\ 10^{17}$	25	$2\ 10^{18}$	20	$5\ 10^{18}$	AlInP
3.2.4	AlGaInP window	20	$3\ 10^{18}$	0.3	1000	$2\ 10^{17}$	100	$2\ 10^{18}$	20	$2\ 10^{18}$	AlGaInP
3.2.4	AlInP window	20	$3\ 10^{18}$	0.3	1000	$2\ 10^{17}$	50	$2\ 10^{18}$	20	$2\ 10^{18}$	AlInP

Table 3.5: Details on the structures fabricated in this work. The cells also comprised 300-nm-thick GaAs contacts layers (identical in all cells).

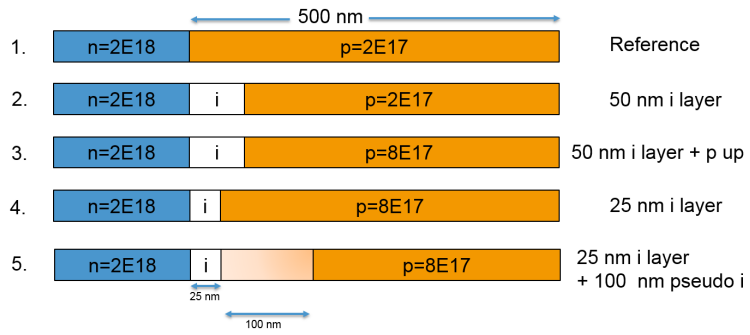

Figure 3.21: Sketch of the different structures tested in the study

3.2.5 Adding an intrinsic layer in the p-n structure

In the previous studies, we have shown how to maximize the photoconversion in the front of the cells, a steep EQE raise was thus obtained at short wavelengths. However, all the structures exhibit a non-expected behavior at longer wavelengths. Their EQEs slowly decrease and the usual "plateau" is not observed. These issues are characteristic of a poor base quality. As illustrated in Figure 3.9, the base contribution on photons absorption increases with the wavelength. The most probable reason of the poor conversion in the base is that electrons generated within the base recombine before reaching the p-n junction.

One pathway to solve this issue is to increase the depletion region thickness by introducing an intrinsic layer (hereafter i-layer) between the n and p layers. With a p-i-n junction, the intrinsic layer thickness adds to the depletion region. Electrons in the base have a lower distance to cover in order to reach the junction. This comes at the price of a lower electric field driving the drift current in the pin junction than in the equivalent p-n junction. One can expect better carrier collection thanks to this larger depleted region.

Moreover, as seen chapter 2, the carrier mobility increases while reducing the doping of the alloy. Replacing some of the usual p-doped base with some intrinsic layer should enhance the carrier mobility in this region, and thus improves their collection.

For this study we compared several structures with a 550 nm GaInP absorber and investigated how the thickness of the intrinsic layer and the doping of the base layer influence the cell performance. It is important to keep the GaInP absorber thickness constant to ensure that the changes observed in collected current are not related to different absorber thickness. Thus the emitter thickness was kept constant and a given thickness of i-layer replaced the last nanometers of the base layer.

Figure 3.22 shows how the depletion region (DR) thickness evolves while increasing the thickness of the i-layer within a p-i-n junction. These calculations are performed for doping levels of n=$2.10^{18} cm^{-3}$ in the emitter and p=$2.10^{17} cm^{-3}$ in the base, corresponding to the doping levels used in our structures. We plot the total DR thickness in black and the extent of the DR in the doped layers. Introducing the i-layer reduces the depletion width in the doped layers, but the total depletion region increases. We use the lowest reproducible p-doping for the GaInP base: increasing the DR by changing the doping levels would require to increase n-doping in the emitter which could be detrimental for the front response of the cells. The introduction of an i-layer is therefore an interesting solution to widen the DR without changing the doping levels.

Another effect of introducing i-layer is to separate the ionized donors from the ionized acceptors, therefore when a depleted region comprises a i-layer, the electric field is lower than in a p-n junction. This might cause a decrease of the drift current due to less efficient carrier separation.

First sample were a 500 nm reference cell and a structure comprising: 50 nm emitter-50 nm i-layer-450 base layer (see Figure 3.21). Table 3.6 gives the characterization results from cells characterization, averaged from the cells on the sample. As expected the current increases, from 9 to 9.5 $mA.cm^{-2}$. But unfortunately, an important reduction of both FF and Voc caused the p-i-n cells to be less efficient than the reference cell.

Therefore, we grew several other structures to understand the results observed in this first samples and discriminate the effect related to doping levels and i-layer thickness. We focus on Jsc and Voc as they are the most impacted figures and because the levers for FF improvement are similar to Voc. Using X-ray diffraction, we noted slight variations of composition between the samples and will intend to discriminate this effect from

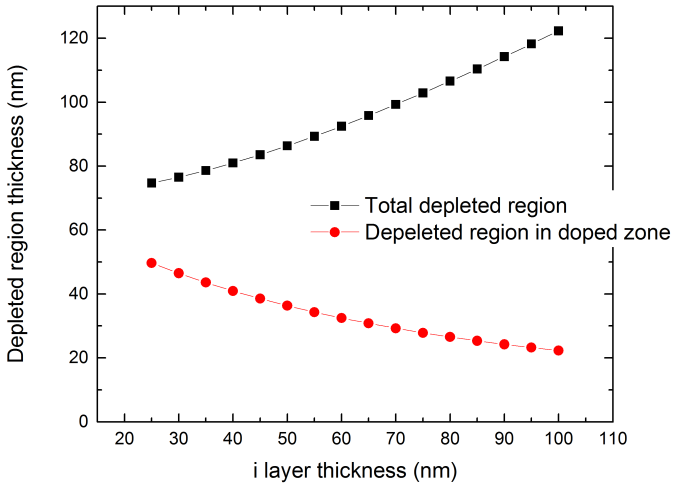

Figure 3.22: Depleted region thickness depending on the thickness of intrinsic layer introduced in the structure

the i-layer effects at the end of the section.

Figure 3.21 sketches the different absorbers tested and table 3.6 summarizes the characterization results.

Let us first compare the reference structure with the structure comprising 50nm of i-layer. Using Equation 3.5 and EQE data, we can quantify the currents variation provided by specific zones of the cells (Figure 3.23, a)). The cells with intrinsic layer gain around 0.63 $mA.cm^{-2}$ from the photons with wavelength above 500 nm. This results from the fact that the DR spreads more in the base (20 nm) and that half of the depleted region is non-doped. Less distance to be crossed and better mobility in the depleted region improve the collection of photons absorbed in the base. Then, 0.15 $mA.cm^{-2}$ are lost in the front of the cell, this is attributed to less efficient carrier separation. In this region with high concentration of generated carriers, the decrease of the electric field in the DR has more impact than in the p side of the pin junction, leading to this loss.

In order to recover Voc, the doping of the base was increased. This should have two advantages, reducing the resistance of the base, and increasing Vbi of the p-i-n junction. We expect Voc to increase with Vbi. Then, the n doping was increased from $5.10^{18}cm^{-3}$ to $8.10^{18}cm^{-3}$ in the window layer. This aims to improve minority carrier repelling from the front surface and to improve the short wavelength response of the cells. Those adjustments were successful in improving Voc and FF. For the two cells compared in Figure 3.23, the front surface response was also improved: 0.7 $mA.cm^{-2}$ was recovered from the loss induced by the introduction of the i-layer.

However, a global reduction of 1 $mA.cm^{-2}$ occurred on Jsc leading to no efficiency improvement. Figure 3.23 the EQE suggests that the higher doping degraded the base quality as 1.1 $mA.cm^{-2}$ was lost in the long wavelength range. This is mainly due to the reduction of the depletion region thickness (20 nm less than in the previous structure, see Figure 3.24 b)) and also from lower diffusion length in the base due to lower carrier mobility at higher doping level.

In other words, the change for the higher base and window doping allowed the recovery of the FF and of the reduction of some current loss in the front of the cell. It also improved Voc. However, the benefit provided by the insertion of the i-layer for the carrier collection in the base is suppressed. The point is to keep the benefit of the doping difference between the base and the emitter, while recovering collection of the carriers generated in the bulk. To benefit from a long DR and reduced the base area limited by a high doping level, a cell with a gradual doping was fabricated: with 25 nm i-layer and a 100 nm layer with a gradual doping level varying from $8.10^{17}cm^{-3}$ to intrinsic. Figure3.25 shows that this profile lengthens the DR to the same size as the reference structure. Consequently, the current is improved in the long wavelength range,

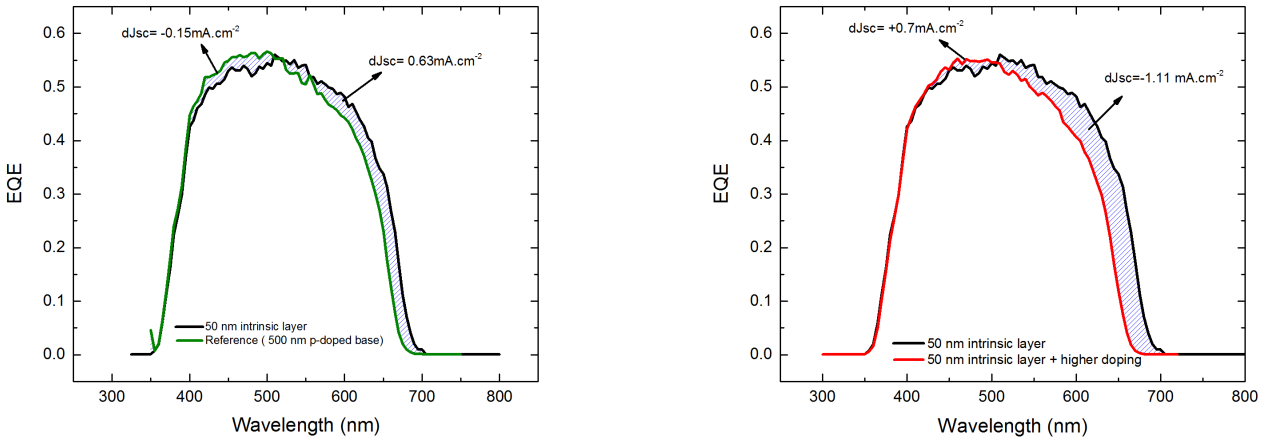

(a) (b)

Figure 3.23: a) EQE comparison of cells with 50 nm i-layer and reference cell. Current gain or loss of specific spectral ranges displayed as dJsc. b) Comparison of the structures with 50 nm i-layer. Influence of base and window doping concentration increase.

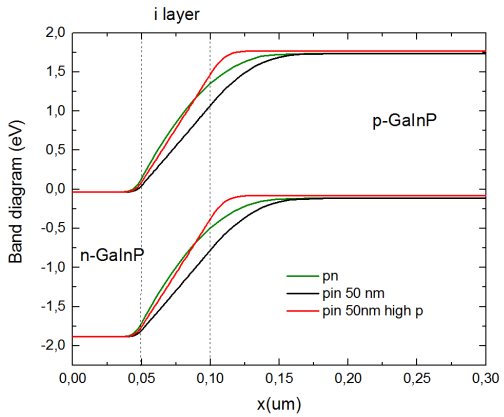

Figure 3.24: Band diagram of the reference and structures comprising 50 nm intrinsic layer.

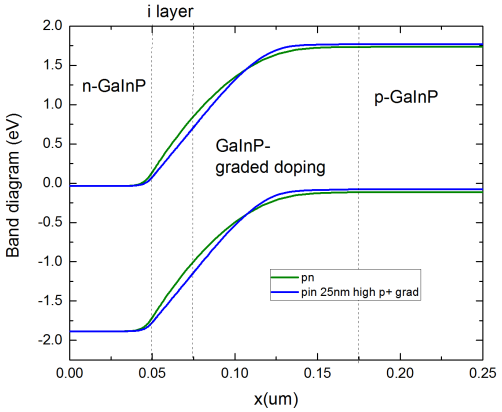

Figure 3.25: Band diagram of the reference and structures comprising 25 nm intrinsic layer.

profile type	Eg* (eV)	Jsc ($mA.cm^{-2}$)	FF	Voc (V)	Efficiency (%)
reference	1.93	9	0.82	1.3	9.66
50 nm i layer	–	9.5	0.77	1.21	8.99
50 nm i layer and higher doping	1.925	8.5	0.81	1.29	8.95
25 nm i layer and 100 nm pseudo-intrinsic	1.895	8.8	0.8	1.24	9.09

Table 3.6: Recap of the results from cells comprising an intrinsic layer. * Indication of the bandgap extracted from XRD

while FF and Voc do not change. Yet the efficiency of this structure does not overcome the performance of the reference structure.

Regarding the Voc variations, the bandgap value of the GaInP layer has an important influence. Table 3.6 shows that the Vocs follow the bandgap variations, yet the introduction of the intrinsic layer also impacts the difference in Vocs since it exceeds the bandgap variation. On the other hand, it seems that the bandgap variations were to small to impact the Jsc.

As a conclusion of this study, the use of an intrinsic layer in the cells does produce a higher Jsc current, however it tends to degrade the other figures of merit of the cells. Tuning the base doping profile can partially reduce this degradation, however the overall balance shows that the efficiency could not be improved with the insertion of the intrinsic layer. The use of intrinsic layer is of interest when the material quality reduces its impact on the Voc and the FF.

3.3 Analysis of the results and limitations

3.3.1 Focus on cell base and associated issue

With the best efficiency stagnating around 11%, we must identify the remaining limitations. Looking at state of art cells, it is obvious that work remains on all aspects of the cell. But the most significant gap between our cells and those reported in the literature lies on the current collection. A Jsc increase of 30%, respectively 50% is needed to catch up with MBE [104], respectively MOCVD [48], state of the art. EQE data show how important is the room for improvement of absorption/collection. By comparing the EQE of the state-of-art cell and the EQE of our reference cell in the Figure 3.26, one sees that 68% of incident photons are collected at best with our cells, while almost 90% of incident photons are collected over a large range of the absorbed spectrum for good GaInP cells.

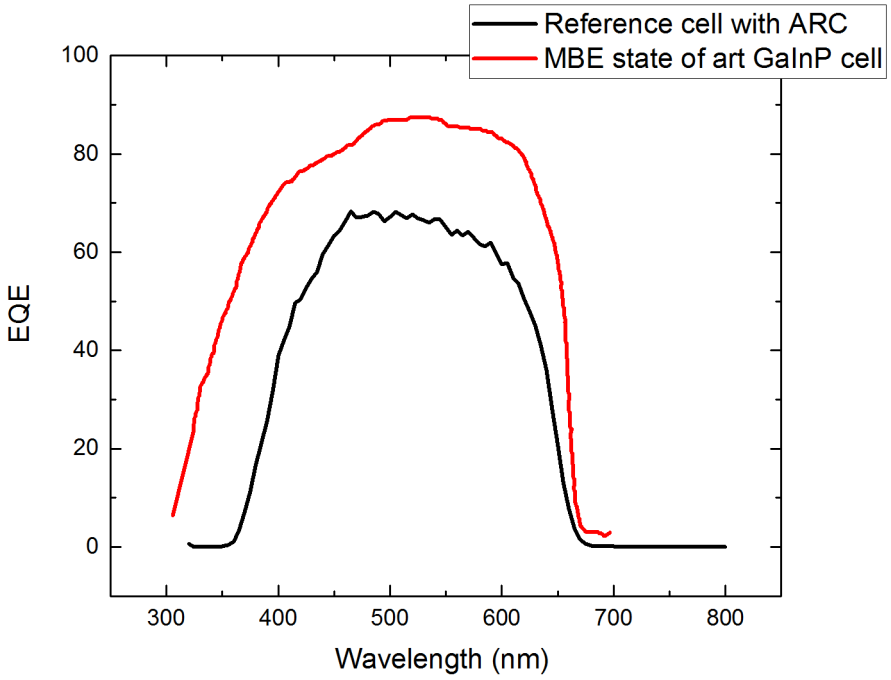

Figure 3.26: Comparison of EQE with state of the art cell. In red, data from best MBE-grown GaInP single junction cell [104], in dark our best GaInP cell.

In Figure 3.26 we clearly see a plateau in EQE from 500 to 650 nm for the Lu et al cell [104]. In our case, there is no constant conversion efficiency. EQE decreases after 450 nm. This is symptomatic of a lack of contribution from the base layer. The higher the wavelength, the bigger is the probability that photons will be absorbed in the base. Hence, all our EQE spectra suggest that an important part of carriers generated in the base recombine before being collected, i.e. electrons generated at the rear of the cell do not reach the depletion region.

To confirm this hypothesis, we modelled the variation of photogeneration and recombination rates with the cell depth. Their profiles was extracted from the fit of the "50 nm emitter" cell (Table 3.2) with the model used to predict the effect of the thickness of the emitter (in Section 3.2.3) . They are shown in Figure 3.27. In the base, the generation and recombination rates are equal, except in the first 200 nm near the p-n junction. This means that the probability that electrons generated in the base reach the p-n junction is small: no electron generated farther than 200 nm from the p-n junction contributes to the current.

This is a major issue that need to be address. This poor base quality not only impact the Jsc but probably degrades both Voc and FF. Providing that we improve the base of our structure, we can expect to catch up

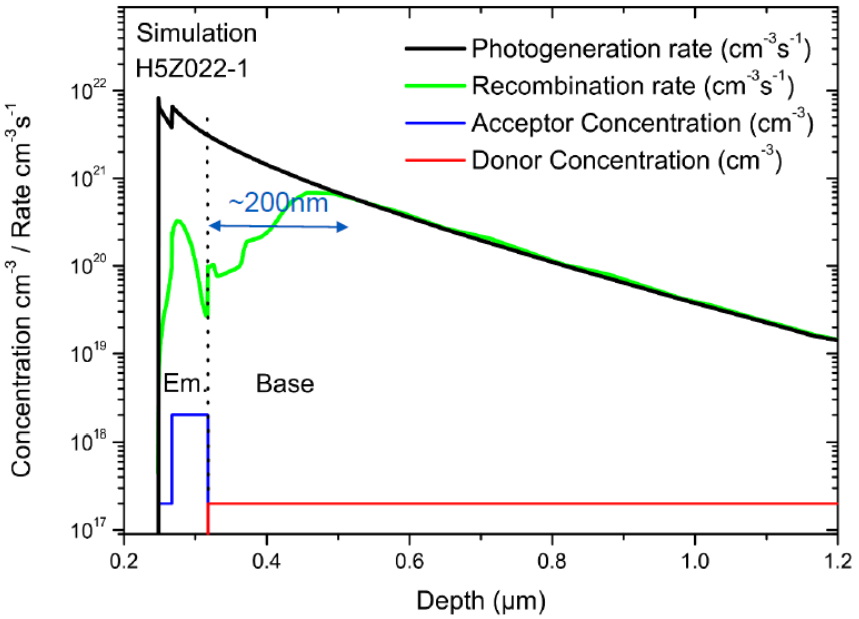

Figure 3.27: Photogeneration rate and recombination rate profile with depth. Obtained from the simulation of a 50 nm thick emitter cell with no window.

with the state-of-art short circuit currents.

3.3.2 Experimental illustration of the base limitations

We have concluded that the performance of our cells is limited by the p-doped GaInP material quality. The cell structure is probably not optimal yet, but the latter issue can hide the improvement that would result from other adjustments of the structure. As an illustration, the composition and thickness of the BSF were varied. But as suggested in section 3.2.4, BSF effects are subtle and since our base material does not permit the collection of carriers generated at the rear of the cell, we did not observed any significant effect by varying the BSF layer parameters.

Sample	Jsc ($mA.cm^{-2}$)	FF	Voc (V)	Efficiency (%)
C2N reference cell	8.15	0.78	1.23	7.87
IPVF reference cell	9.05	0.82	1.3	9.66
C2N reference cell (with ARC)	10.69	0.78	1.24	10.42
IPVF reference cell (with ARC)	10.94	0.8	1.29	11.60

Table 3.7: On the influence of the material and growth quality. Comparison of identical cells grown in different MBE.

During this thesis we had to move our activities from a MBE machine belonging to the ELPHYSE group at C2N to an identical MBE at IPVF. We perform a second optimization of the growth conditions, to find almost identical optimal condition as in Chapter 2. Interestingly, changing the MBE equipment provided an improvement of 1.79% efficiency with the structure optimized at C2N. Table 3.7 shows that all the cell parameters improve with this new machine. This suggest how much can be gain from further work on the material quality. Changing the growth machine we benefited from a chamber dedicated to our photovoltaic project, where only effusion cells needed for our III-V structures where loaded. In the C2N MBE the presence of Antimony and Carbon might pollute the layer, we will develop later how the MBE configuration can be further improved.

To confirm the poor collection of photocarriers generated in the base, three structures with different base thickness where grown: 1 µm, 750 nm, 500 nm. The current is expected to decrease with the base thickness, because less incident photons will be absorbed. However we observed only a little impact on the cells current and efficiency. Indeed halving the base thickness the current is only reduce by 3.5%. Furthermore, the cells with a 750 nm base have lower short circuit current than cells with 500 nm base.

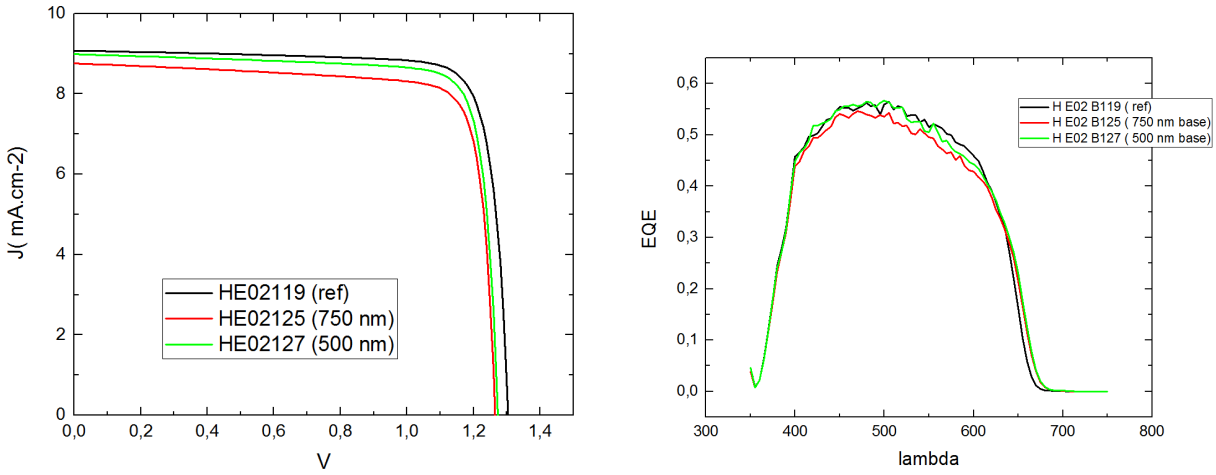

(a) (b)

Figure 3.28: Influence of the base thickness on the IV and EQE of GaInP single junction cells.

This leaves no doubt on the fact that all cells have a serious collection problem in the base as important reduction in absorption has no impact on the current collected.

3.3.3 On the control of the open circuit voltage

We have improved the Voc of our structures during our studies. However, some fluctuations of the values were not fully comprehended.

The open circuit voltage is linked to the energy at which carriers are collected. Some intrinsic losses cannot be avoided resulting in maximum Voc values, then other losses are linked to the quality of the devices. A popular convention is to write Voc as: $V_{oc} = \frac{E_g}{q} - W_{oc}$

where Woc is a figure of merit, in volt, to evaluate the quality of the cell (material and contact quality) [111, 112]. This Woc comprises thermalization, Carnot and Boltzman losses [11], other sources are resistances or saturation current J_s:

$$V_{oc} = \frac{kT}{q}.ln(1 - \frac{J_{sc}}{J_s}) \tag{3.6}$$

$$J_s = q.n_i^2(\frac{D_e}{n_A.L_e} + \frac{D_h}{n_D.L_h}) \tag{3.7}$$

Where **k** is Boltzmann constant, **q** elemental charge, **ni** intrinsic carriers concentration, n_A and n_D are respectively acceptor and donnor concentration. **De**, respectively **Dh**, are electron respectively hole diffusion coefficient. **Le**, **Lh**, electron, respectively hole diffusion length.

Cells are considered of good quality when Woc$<$ 0.5 V. Equation 3.6 and 3.7 highlight that large Voc requires the smallest reverse saturation current possible. Moreover the saturation current Js is deeply related to material quality via intrinsic carriers concentration and diffusion length.

The bandgap of every samples (from Section 3.2.5 and Section 3.3.2) was estimated with X-ray diffraction on the solar cell stacks. First, we notice that, despite our daily calibration with RHEED oscillations, there is a variability in the GaInP composition of the different cells. Having the real composition of cells, we look at the bandgap influence on the Voc. Figure 3.29 displays in black the mean Voc for a given structure and in red,

the difference between the band gap of its GaInP layers and that of the target composition, lattice-matched to GaAs. There is a clear correlation showing that the prime source of the Voc variation is the bandgap dispersion between samples.

The Wocs measured, which values exceed 0.6 for all the cells, reveals the room of improvement still available.

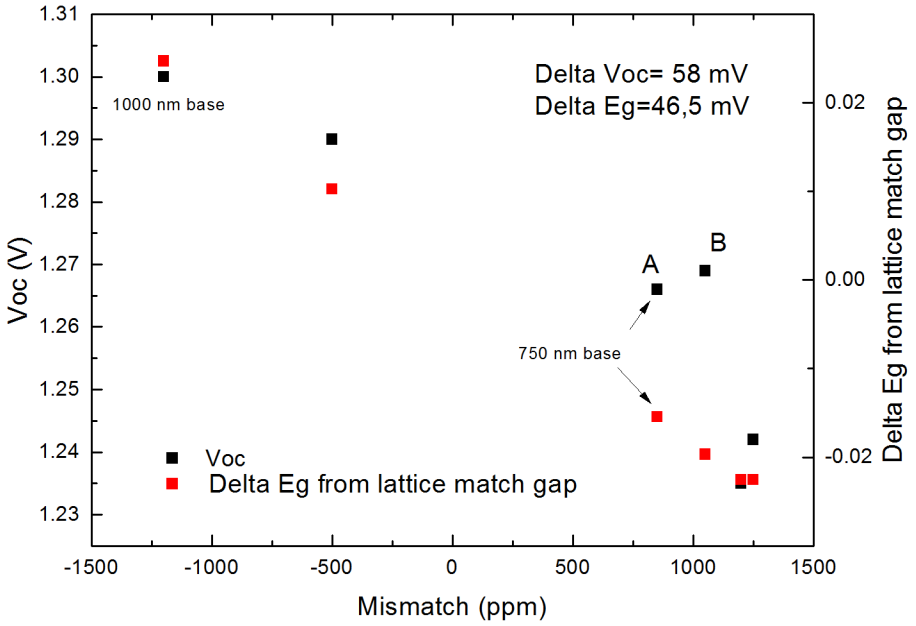

Figure 3.29: Strain impact on Voc. Voc mostly follows bandgap variation induced by the composition variations. If not stated otherwise, data points are for solar cell with 500-nm-thick base.

The general tendency illustrated in Figure 3.29 can be exploited: growing slightly Ga-rich GaInP layers (without exceeding a composition, which would result in the formation of misfit dislocations), Voc can be increased.

Base quality also impacts the Voc. The batch of p-n cells highlight how the Woc decreases with the base thickness. Figure 3.30 shows a reduction of 13 mV on the Woc when halving the base thickness. This reduction explains why in Figure 3.29 samples labeled A (which has 750 nm base structure) an B (500 nm base) do not follow the bandgap trend in Figure 3.29, and have Vocs above the expected value. Finally, the introduction of an intrinsic layer in the structure tends to increase the Woc. This indicates that the variation in composition between the different structures is not fully responsible for the reduction of Voc observed in section 3.2.5 and validates our observations in this section.

3.3.4 Summarizing the GaInP single junction cell study

Significant progress was achieved, but much work remains before we reach the state-of-the-art conversion efficiency.

The window and emitter layers are determinant for the efficiency of the cell in the short-wavelength range. By optimizing these layers, the efficiency was increased from 4,9% to 11%. However, our GaInP cells collect poorly the photo-carriers excited by the longer wavelength range of the spectrum. At these wavelengths, the most of the photons are absorbed deeper in the structure: in the base layer. The problem is thus related to quality of the p-doped GaInP. However, Jsc could not be improved by inserting an intrinsic layer between the n and p layers.

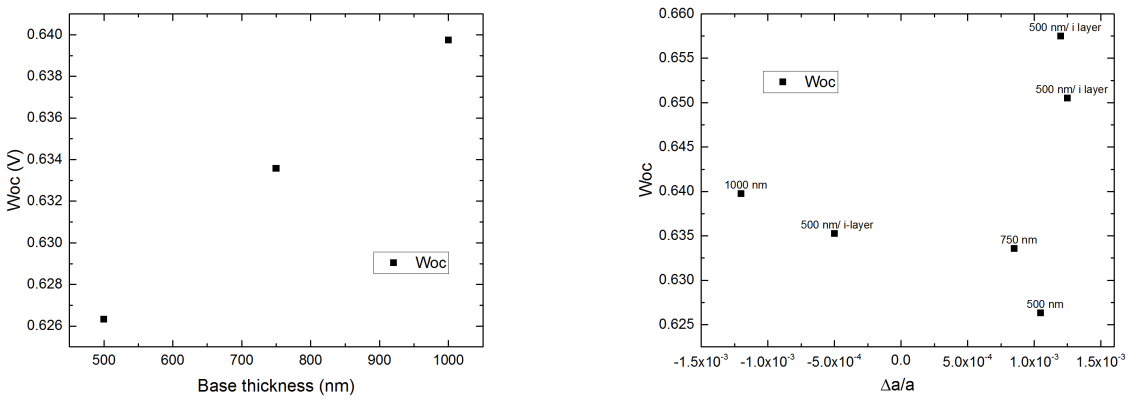

(a) (b)

Figure 3.30: Woc for the cells. a) Effect of the base thickness on the Woc for p-n cell. b) Woc of all cells: p-n cells with different base thickness and p-i-n cells from Section 3.2.5.

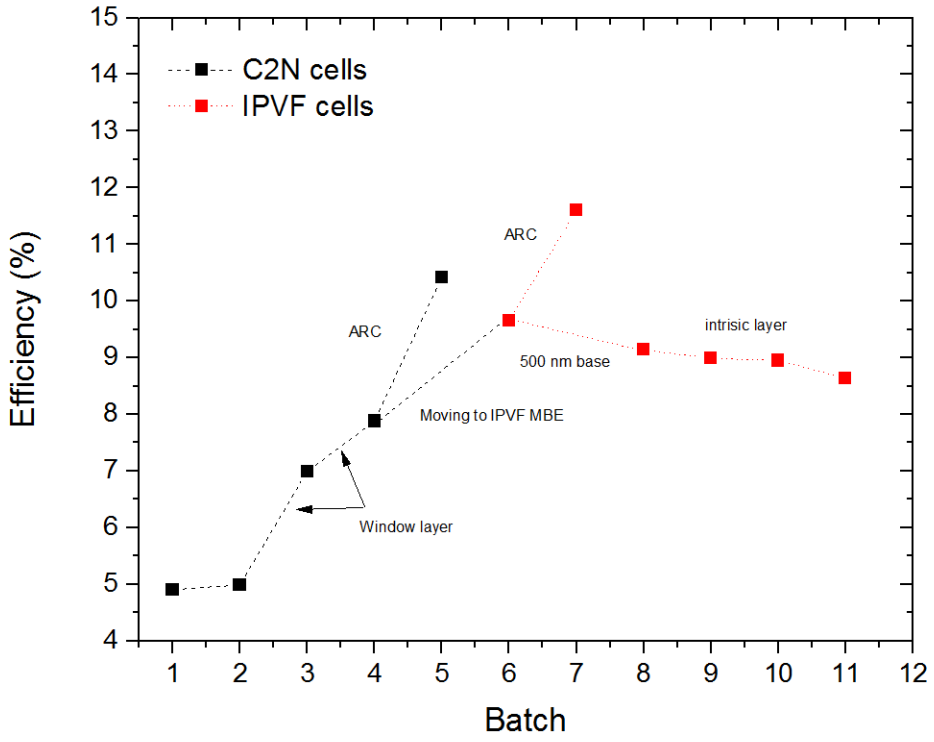

Figure 3.31: Cells study wrap-up

The purity of the nominally undoped GaInP alloy is probably not high enough. A better quality of the p-doped layer should also improve the Voc of the cells.

In the next chapter we will develop further on the material limitations degrading the cells and technical solutions will be proposed.

3.4 Top cell integration on Silicon cell

Despite the limitations observed on the top cells, we develop methods in order to transfer them and to progress toward a full tandem device. As developed Chapter 1, a 4-terminals design was chosen. This requires a robust bonding method that is both transparent and insulating. In this section, we will expose the different methods attempted and the issues encountered.

3.4.1 Additional process steps

The transfer of cells on a host requires additional process steps, the growth of the solar cell structure also needs to be adapted to such a process.

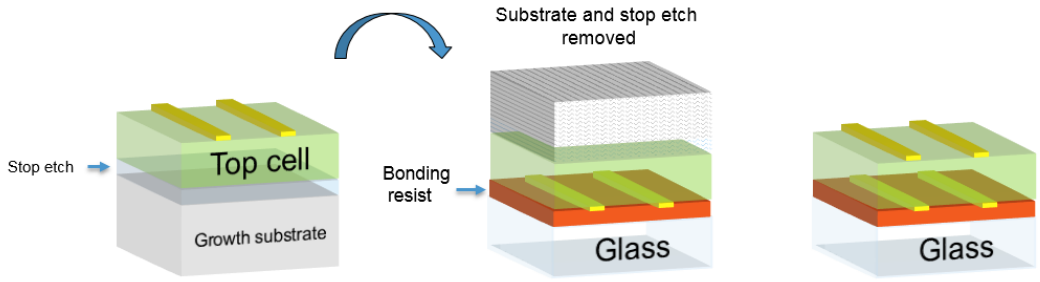

Figure 3.32: Additional steps required for the transfer of cells on glass

First, the layer stack must be inverted during growth. Indeed, the back of the cell should be the surface of the epitaxial structure since it will be stuck on the host. Then the growth substrate is removed, ideally with epitaxial lift-off (ELO) [113, 32, 31] which permits growth substrate reuse. In our process, we just etch the growth substrate completely. ELO which is an indispensable building block for the competitiveness of III-V tandem cell will be addressed later in IPVF projects. A specific layer is necessary to remove the substrate without any damage to the cell. To this end, a layer called "etch-stop" is grown prior to the cell structure. It will permit a selective etch of the GaAs substrate. Then, the etch-stop layer must itself be removed without damaging the next layer of the structure, which is the n-GaAs contact layer. Two good candidates are $Al_xGa_{1-x}As$ alloy (with x>0.6) and GaInP. We chose to use $Al_{0.8}Ga_{0.2}As$ since the solution needed to remove a GaInP etch-stop layer may damage the GaInP layers of the cell if the sidewalls are not fully protected.

So, first an AlGaAs etch-stop is grown, followed by the layers of the desired cell structure grown in the reverse order. Then, the cell process starts with the back contact metallization. It consists of either Ti/Au deposited on the whole back of the sample or the deposition described in section 3.1.2 (step 2) which enables the light to pass through and reach the bottom cell. Once the metallization is completed the sample can be bonded to a host (glass, Si wafer, Si cell). The bonding methods will be presented later on.

The growth wafer is removed via chemical etching. As the contact layers of the cell are also made of GaAs, the side of the sample is protected with wax. The sample is then etch in $H_2SO_4/H_2O_2/H_2O$ 2:1:1 for 25 min, while rotating the sample of 90° every 5 min for better homogeneity. In order to continue the etching at more moderate speed, a $NH_3/H_2O_2/H_2O$ 1:1:2 solution is then used. The sample remain in the solution until the etch-stop layer appears, with again a 90° rotation every 10 min. The etching is finished in a Citric acid/H_2O_2 5:1 solution that allows a selective etch of GaAs on the AlGaAs etch-stop. AlGaAs layer is removed with a deep of a few seconds in 1% HF solution. Table 3.8 recapitulates the substrate removal process.

Once the stop etch is removed, normal process (described section 3.1.2) permits to complete the cells.

Solution	Volumic Ratio	Usual etch time
$H_2SO_4/H_2O_2/H_2O$ at 50°C	2/1/1	25 min
$NH_3/H_2O_2/H_2O$	1/1/2	50 min-1h
Citric acid/H_2O_2	5/1	2-3h

Table 3.8: GaAs substrate etching procedure

3.4.2 Bonding Methods

The method chosen needs to be simple and without demanding process steps. Mechanical stacking, intercalating a glass slide between cell is a successful method [114], we would also like to be able to stack the III-V cell directly on the Si cell.

3.4.2.1 Ormostamp bonding:

Ormostamp, a viscous polymer, offers glass like properties once cured with UV. Generally used for the fabrication of nanoimprint stamps [?, 115], it can be used for bonding purposes. The UV curing is not compatible with bonding on Si that would absorb the UV light, however it is an interesting polymer if a glass host is used. With this solution, it is better to add a few nanometer of Chromium on the back metallization of the cell to enhance the Ormostamp adhesion on the metallized area. The glass slide is cleaned in Piranha solution and acetone to remove any organic residues. Then, it is dried on a hot plate at 120°C. Ormostamp is spin-coated on both surfaces to be bonded. Finally the sample and host are brought into contact and exposed to a UV lamp for 20 min of curing.

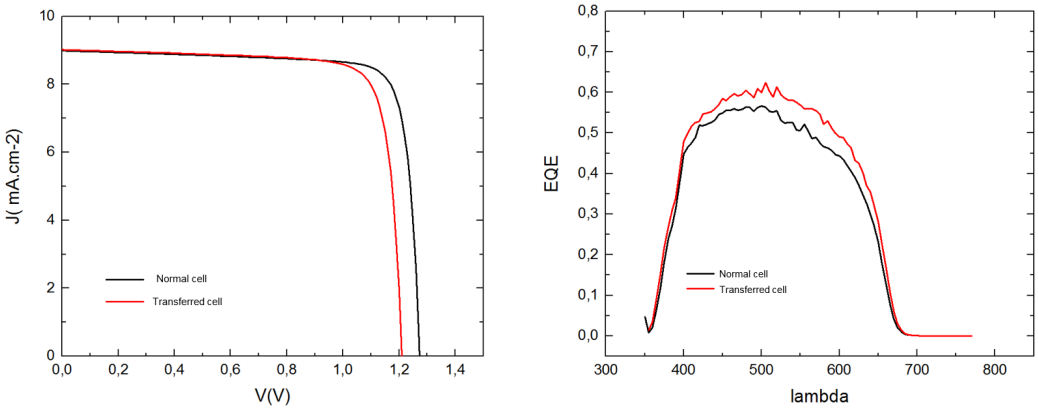

(a) (b)

Figure 3.33: Comparison of GaInP cell structures characteristics for normal configuration in black, bonded to glass with Ormostamp in red. a) JV b) EQE

Bonding tests were performed on samples with a back surface fully metallized (with Ti/Au/Cr). The process described earlier led to the following result: a GaInP structure of 9.30% efficiency without transfer, showed a 8.57% efficiency after transfer. The same transfer process applied to an AlGaAs structure (as AlGaAs is another III-V alloy studied in Project E), resulted also in a slight decrease of efficiency, from 12.5% to 11.86%. Remarkably, the collected current is generally higher for transferred cells. This is highlighted by the EQE spectra in Figure 3.33: the cell transferred has a better response over the whole spectrum. The cells probably benefit from reflection from the glass slide, enhancing the base response. On the contrary, FF and Voc are lower when transferring the cell. In addition, the variability of the cell performances increases significantly after the transfer. This may be due to the etching of the mesa, necessary for the isolation of the cells: the sample is dipped for a relatively long time in the solution in order to etch the whole III-V stack. Etching might not be fully homogenous and cause side etch in some cells.

3.4.2.2 Cyclotene 4026-46:

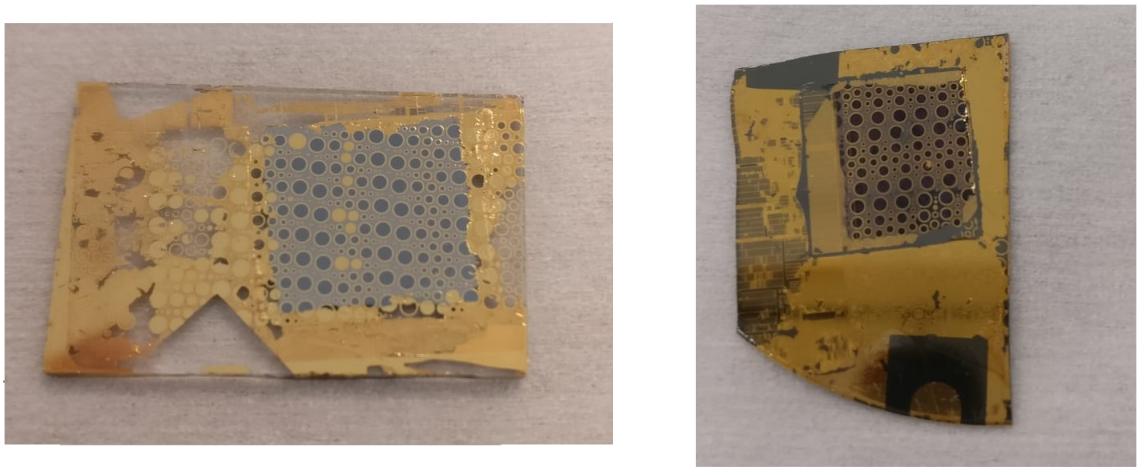

(a) (b)

Figure 3.34: Pictures of transferred cells: a) bonded to glass slide with Ormostamp. b) bonded to Si wafer with BCB.

The cyclotene 3022-46, bisbenzocyclobutene (hereafter BCB), is a polymer resist designed for microelectronics packaging and processing [?]. This resist is extensively at C2N to process III-V devices on SOI substrates. We used it to bond the III-V cells on (100) Si host. Our process consists in sputtering a thin layer of SiO_2 on the two surfaces to be bonded, then BCB, diluted in mesitylene, is spin-coated on both surfaces. Samples are outgassed for 15 minutes at 80°C. Then, the two pieces are brought into contact with each other and placed in a bonder. The bonder applies a pressure and temperature ramp with final values of 250 mbar and a temperature of 320°C. Those conditions are maintained for 30 minutes. An alternative process without bonder consists in a 10 h curing on a hot plate. BCB bonding has been successful on glass substrate and Si wafer.

Figure 3.34 shows a batch of cells transferred on Si with this process. A very little degradation of the cell performance was noticed: efficiency changed from 11.94 % to 11.85 %, without and with the bonding, respectively.

Since the Si cells are textured (the depth of the surface pattern is about 4 μm and their top contacts are about 20μm thick), we used BCB to benefit from its planarization capacity in order to bond the III-V stack directly on a Si cell. Inverted III-V structures were bonded to Si cell pieces (of larger surface), using the hot plate curing. Adhesion properties were satisfying. Before processing the top cell, the area of the Si cell surrounding the bonded surface was protected with wax. Growth substrate removal from the III-V cell after bonding was successful for the top cells bonded. Although, during this step, we could not avoid some damages of the metal contacts of the Si cell.

After the growth substrate is removed, the remaining III-V layers are only 1.6 µm thick. This stack starts to bend between the Si cell fingers because of an important stress at the bonded interface. As shown in Figure 3.35 , the III-V stack eventually breaks and strips of material start to peel between the fingers. Because of this issue, we could not process the top cell and we could not obtain functional cells.

The fingers thickness is close to the maximum thickness of the BCB coating. The bending may results from a too important volume reduction of the BCB film during the curing.

Taking into account these issues (III-V bending and degradation of the Si bottom cell), we decided to bond each cell on one side of a glass slide.

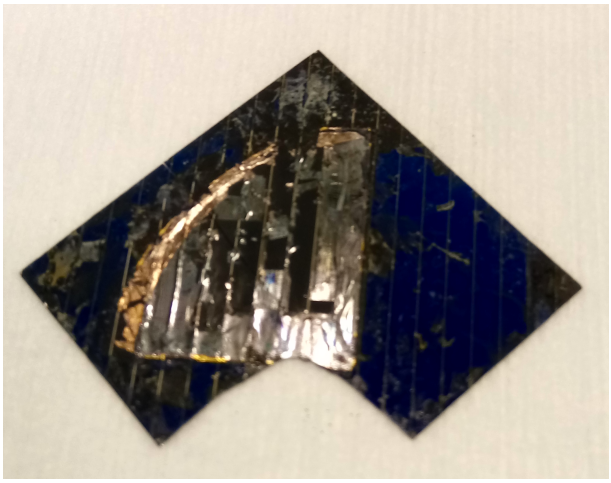

Figure 3.35: Picture of a III-V stack bonded to Si cell with BCB. Once mechanical support from the GaAs substrate is lacking, the cell stack eventually bends and peels.

3.4.2.3 Poly-Di-Methyl-Siloxane (PDMS):

The PDMS is another polymer, used for micro-fluidic applications for example [116, 117]. It is cheaper and more adapted to bigger batches than the other two solutions. A bonding process consists in a few basic steps: mixing of the precursor and the curing agent, spin coating on the sample, contact to the host material and finally curing on hot plate. In order to avoid bubbles to be trapped between the two pieces, we found that it was better to add a few steps. First a long degassing under a vacuum bell after mixing the two PDSM components, then another degassing step before the curing, so that the few bubbles trapped while bringing the two pieces into contact, can flow to the edges.

We fabricated two types of samples with the PDMS method. First type of samples is III-V top-cells with full plate GaAs back-contact. Second type corresponds to III-V top cell adapted to the tandem configuration, where the GaAs back-contact layer is etched when not covered by the back-metallization.

Regarding our first type of samples: transferred cell not adapted to a tandem design (since the 300-nm-thick GaAs layer will cause parasitic absorption for the Si bottom cell). Two different designs were tested, one design with a flat bonding surface, the GaAs back-contact layer. The metallic back-contacts of the cell were deposited on the surface of the GaAs back contact (see Figure 3.36 for details) to permit the characterization of the cells.

The second design is closer to a viable top cell, the back-contact pattern is deposited on the GaAs and bonded to glass (Figure 3.36).

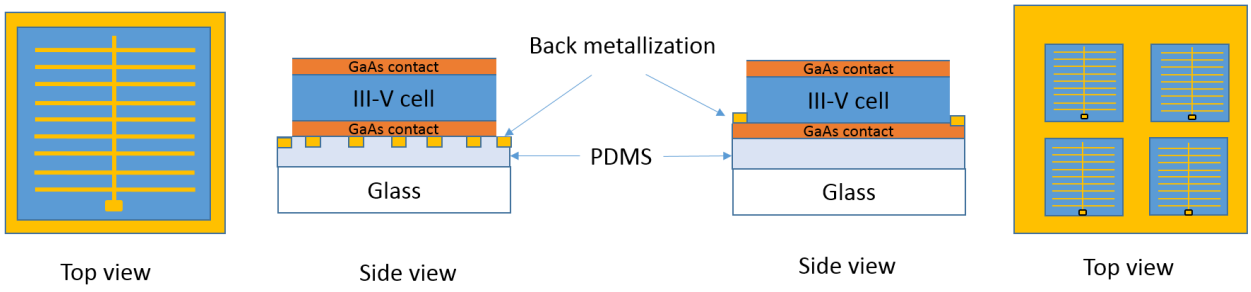

Figure 3.36: Structure of the two cells samples transferred on glass, on the left version with fingers on the back of a $1cm^2$ cell, on the right metallization of the full front the surface of the GaAs back-contact layer.

The substrate removal and the solar cell process were successful. The first design led to working cells. The second design (a $1cm^2$ cell), revealed lithography issues and could not be characterized. For this type

of back-contact, the mesa etching (explained in section 3.4.3) must remove all the III-V layers and expose the metallic contacts at the rear of the stack. During this last etching step, over-etching has isolated the cell from its back-contacts and no current could be collected. More details on this issue will be developed in the next section. Apart from this issue, we did not detect any cracks or peeling related to PDSM bonding.

With adjustments on the lithography, the back-contact isolation issue was solved. The second type of sample was processed. With this type of sample, GaAs back-contact layer remains only under the back-metallization grid, while in the first type, the GaAs was surface bonded to glass. For the six samples processed, cracks and peeling of the III-V stack was observed. From confocal microscope observation, the cracks seem to be ignited by the back-contact motifs: they mostly follow the metallization edges. Removing the GaAs layer, it seems that cracks cannot be avoided, and therefore this process is not a viable method for our project.

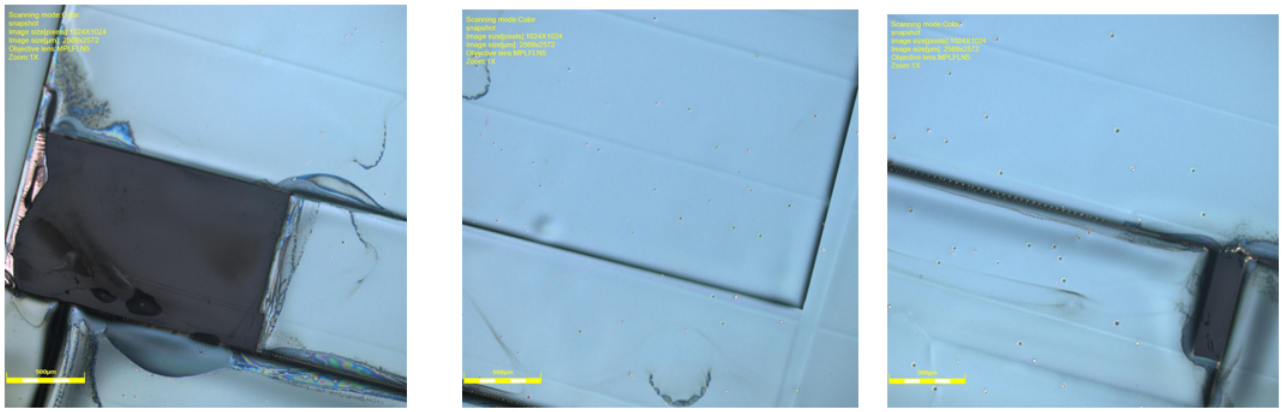

Figure 3.37: Confocal images of III-V top cells bonded to glass. The back contact metallization visible through the cell seems to cause the cracks.

However PDMS is a good candidate for the bonding of the glass slide assembly with the Si cell. We were able to perform such a bonding, using an oven at 100°C. If the adhesion works fine, one challenge is to guarantee that no bubbles remain in the PDMS. This cannot be checked easily since asthe opaque cells mask the bonded interface.

All in all the use of Ormostamp, that combines process simplicity and no arm to the III-V stack, is our best option at the moment. Cell with patterned back contacts were successfully bonded and removed from their growth substrate.

3.4.3 Back-contact metallization lithography

In this section we develop the adjustment of the "back-contact metallization" lithography. For the cell design, shown in Figure 3.36 , the back-contact metallization was obtained from adding pads on the usual "top-contact" mask. These pads serve to extend the back-contact metallization above the top-cell 1 cm^2 area and permit the cell characterization. However this method was not compatible with the mesa etching used during the process.

Indeed, in order to have access to the back-contact metallization, etching of the whole III-V stack is needed around the cell. We use a HBr solution which presents a side effect: etching is faster at the limit of the resist motif. This produces a notch in the III-V stack along the edge of the motif. This even leads to a discontinuity between the GaAs back-contact layer and the metallization (Figure 3.38). This problem has impeded the characterization of the transferred samples.

In order to solve this issue and to improve reproducibility we design a new mask to make the mesa etching viable. Figure 3.39 details the specifications of the new mask design.

The back-contact metallization mask adds a frame to the top contact mask that was used previously. Figure 3.39 shows in blue the usual top-contact pattern, the black area are the shadings added by the new

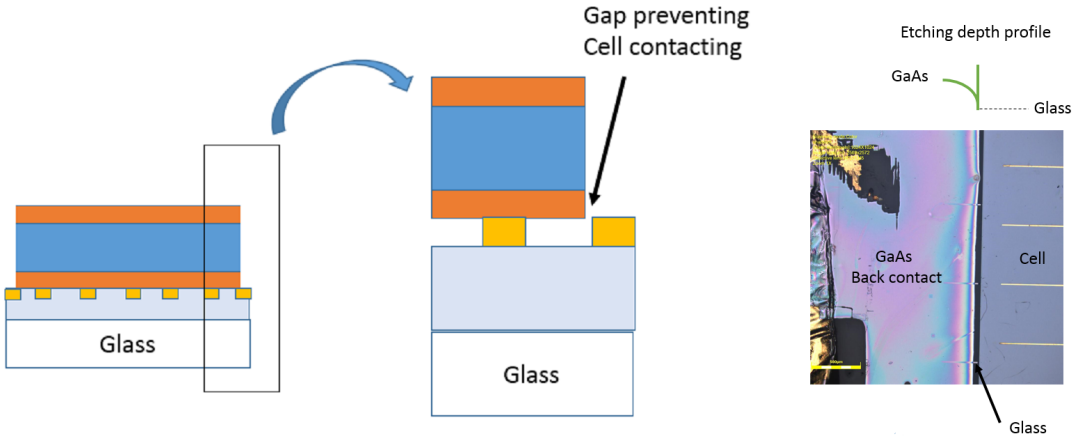

(a) (b)

Figure 3.38: Issue related to the etching step giving access to the back-contact metallic contacts. a) Front view of the structure illustrating the absence of contact between III-V layers and back metallization. b) Optical microscope top view of the etch notch at the mesa edge.

mask. A 1 cm^2 area is identical to the top-contact mask (free area with the grid pattern). The new mask comprises a 2 mm thick frame around this area and two pads also insure the continuity of the metallization between the grid pattern and the frame.

For the mesa etching the shaded area is now bigger than the area defined by the back-contact mask. Indeed, it protects a 1.1 cm^2 area. The notch cause by the Hbr etching now occurs on top of the back-metallization frame, preventing insulation of the cell form the metallic frame used for the characterization contacting.

Figure3.40 displays the results after this lithography step. Clear areas correspond to exposed III-V while the darker areas are protected by the resist.

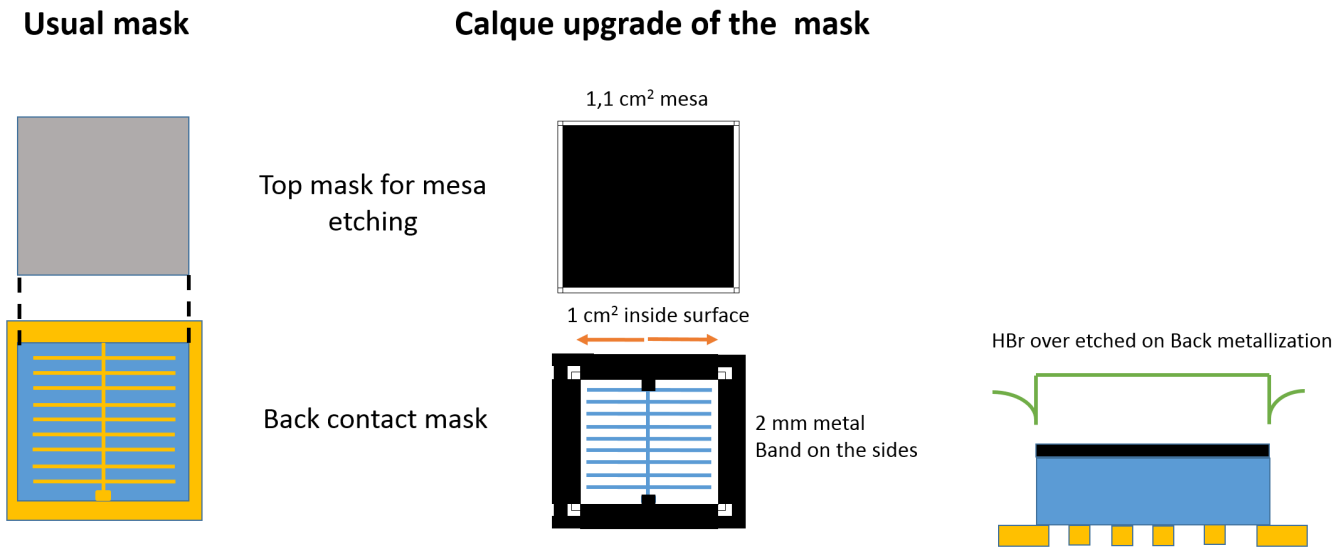

Figure 3.39: Details on mask adjustment with the calque. a) with usual method, the mask delimiting the mesa and the back contact frame are of same size. It results in the issue pictured Figure 3.38. In b) Front view of the sample after lithography step. With the calque adjustment the over-etched occurs on top of the back-metallization, solving the isolation issue.

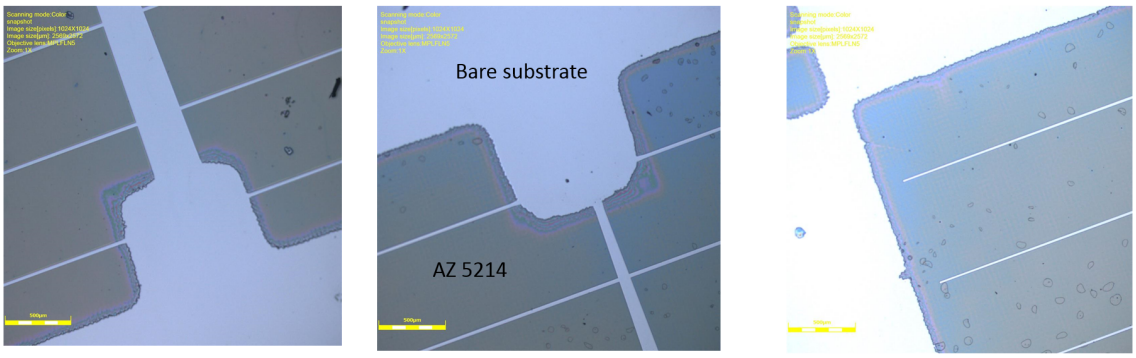

Figure 3.40: Pictures of the modified back-contact lithography. Bright areas correspond to III-V surface that will be metallized, darker areas correspond to the resist covering the III-Vs.

Take away message from Chapter Three:

- Window layer composed of AlInP is the best front surface passivation option.
- Interfaces between layers are not abrupt, composition gradients revealed by EDX profiles. These gradients should not degrade the performance of the cell.
- Thinning the emitter improves the cell response by reducing the distance between cell surface and the depletion region. 50 nm was found to be the optimum thickness experimentally.
- Several observations point the Be-doped GaInP layer (the base layer) as the limiting factor: the EQE spectrum shows a reduced efficiency in the high wavelength range; a thicker base does not lead to more collected current but to an increase of Woc.
- Adding intrinsic layer is of interest, however no significant improvement could be obtained.
- Best cells has a 9.66% conversion efficiency, with Voc=1.3 V, FF=0.82 and a Jsc of 9.05 $mA.cm^{-2}$. Adding SiNx antireflection coating improves the efficiency to: 11.6 % .
- Process for the transfer of cells on glass and flat Si wafer was developed. When the cells have full plate back-metallization, transfer and bonding were successful with Ormostamp, BCB and PDMS. Little degradation of the conversion efficiency was observed for the transfer process with BCB and Ormostamp.
- Transfer fails when patterned surfaces are involved: direct bonding to textured Si cell and bonding of a top cell with a "patterned back-contact metallization" on glass were not successful.
- Ormostamp seems to be viable for the transfer of cells with "patterned back-contacts" on glass. However transferred cell could not be fully processed before the end of the thesis.
- The back contact metallization process was modified in order to improve pattern reproducibility and solve the issues in reaching the top cell back contact.

Chapter 4

Be-doped GaInP limitations and perspectives for improvement

4.1 Luminescence characterization and comparison with MOVPE grown alloy

In the previous chapter, we noted that the material quality of the base layer is the main limitation to the performance of our GaInP solar cell. Despite the optimization of the growth conditions led in Chapter 2, it seems that further improvements are needed. As pointed out in Chapter 1, MOVPE- grown GaInP solar cells show better performance than MBE- grown cells. A lower material quality related to MBE growth conditions could be at the origin of their difference in efficiency.

In this section we will investigate further on the differences between the GaInP alloy obtained with these two methods of epitaxy.

4.1.1 Comparing MBE and MOVPE materials

As stated in the first chapter, MBE relies on solid element sources, high vacuum and growth temperatures in the 500-600 °C range. On the other hand, MOVPE is based on gas precursors and higher growth temperature (around 700°C).

These different growth conditions may be at the origin of the differences in material quality between these two methods of epitaxy. Since MOVPE uses higher growth temperatures, annealing has been tested to improve the GaInP material grown with MBE.

Rapid thermal annealing (RTA) at temperatures from 700°C to 925°C of GaInP bulk samples could increase carriers lifetimes from 640 ps (as grown) to 2.6 ns when annealed at 925 °C [118]. Deep level transient spectroscopy (DLTS) evidenced that RTA reduces the deep traps concentration within the bandgap (Figure 4.1), this reduction coincide with an increase of carrier lifetimes observed by Dekker et al.

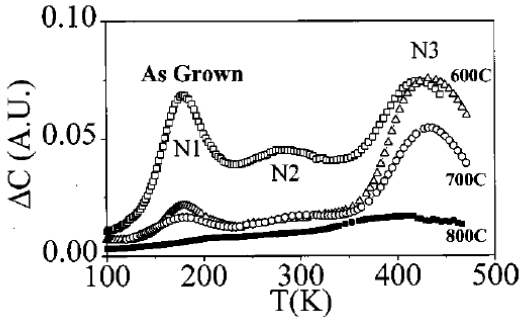

Figure 4.1: Deep state levels in MBE grown GaInP and effect of annealing their concentration. From [118].

Nevertheless, annealing at such high temperature is not trivial. Important surface degradation may occur due to species desorption, especially the group V elements. RTA often consists in short temperature ramp, a plateau (a few s) and rapid cooling to room temperature. To protect the surface from group V desorption, a few nm of SiO_2 is deposited on the sample surface.

We tested annealing on the sample grown at 450°C, studied in Chapter 2. A one min RTA at 550°C was performed on the sample.

In Chapter 2, we have shown that this sample suffers from deep levels that result in PL intensity lower than from the samples grown at higher temperatures. The study of the PL spectra of this sample at different excitation power, allowed to differentiate the deep levels emission from the bandgap transition.

Same experiment was performed on the annealed sample, with laser power varying from 1 µW to 50 µW. Figure 4.2 shows that, at a power excitation of 50 µw, the sample exhibits better PL intensity (x 2.5 higher) after annealing.

Then as seen in Figure 4.3, the ratio of intensities of the bandgap emission relatively to the localized state emission, grows faster with the excitation power for the annealed sample. The band gap emission becomes dominant at 20 µW for the annealed sample, while 35 µW are needed for the "as grown" sample. This suggests that the deep states concentration is indeed reduced by annealing.

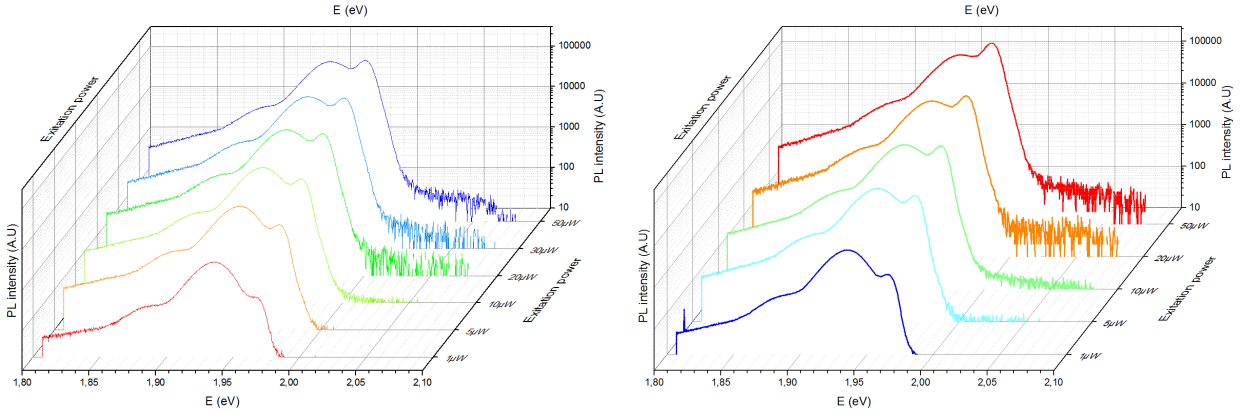

(a) (b)

Figure 4.2: Comparison of the evolution of the PL spectra with excitation power. In a) sample grown at 450 °C studied Chapter 2. b) Sample annealed at 550 °C.

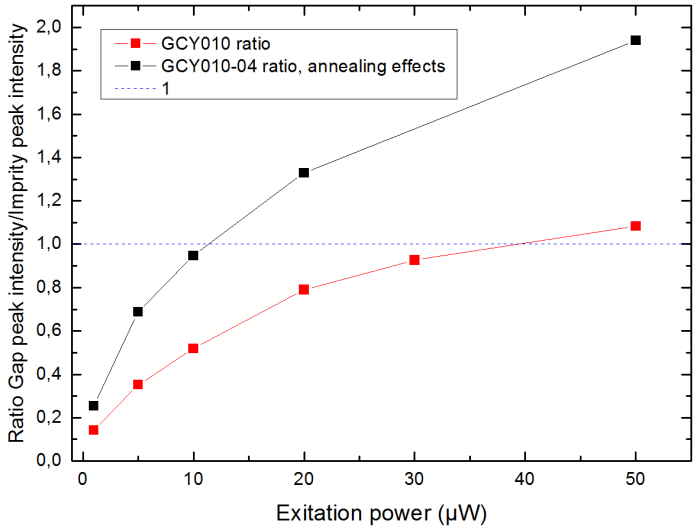

Figure 4.3: Comparison of the deep state and bandgap transition PL intensity depending on the excitation power. In black the annealed sample, in red the as-grown sample.

RTA method was also applied to solar cell samples. In this case, SiO2 was not deposited to protect the surface because it would have requested an etching step before the processing cells. During the anneal step, the GaAs top contact is at the surface of the solar cell sample. We place another GaAs piece on the top of the sample, the surface of the sample is protected from As desorption by the GaAs cap.

Three pieces of cell sample processed of the cells. One piece was processed without annealing, the others were treated by RTA at 700 °C and 800°C. No degradation of the GaAs contact layer was observed. Figure 4.4 gathers the cell efficiencies. Their mean efficiency does not improve with the RTA treatment. A few cells perform better when annealed at 800°C, but the RTA provokes an important spreading of the efficiency which decreases in most cases. Dopant diffusion during the annealing could affect the p-n junction and might be involved in these degradations.

In order to avoid this effect we tested an in situ annealing during the MBE growth. The idea consists in performing the annealing before the start of the growth of the n-doped emitter. Doing so, interdiffusion of the dopant at the p-n junction can be avoided while improving the base layer. In order to compensate the phosphorus desorption, the maximum P flux was provided to the sample. Raising the temperature, we observed that the RHEED pattern became spotty near 615 °C, indicating a degradation of the sample surface. This method was thus considered as not viable with our present conditions.

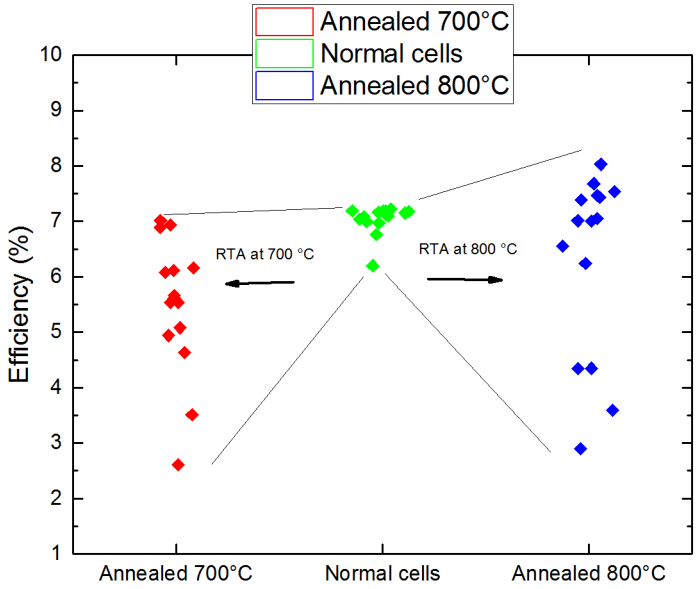

Figure 4.4: Effect of RTA on GaInP solar cells efficiency.

Though annealing seems like a promising path to improve MBE grown GaInP, our attempts were not successful for solar cells.

Another difference between MOVPE and MBE is the p-dopant: in MBE most common p-dopant is Be; in MOVPE Zn is used. We have already mentioned the possible role of Be on the incorporation of O in the phosphides. This may be another origin of the differences observed between MBE and MOVPE cells. Chmielewski and al studied the difference between MOVPE and MBE grown cells [119]. Identical structures (comprising p-doped base layer) were grown with the two methods. Figure 4.5 shows in black the EQE of the two GaInP cells compared. The EQE spectrum of the MBE cell exhibits a shape similar to that of our cells. Above 550 nm, the MOVPE cell, shows better PV conversion than the MBE cell (solid and dotted black lines respectively). This is exactly the wavelength range corresponding to our present limitation. The authors also compared the samples with deep level optical spectroscopy (Figure 4.5 b)). Trap concentration was found below the detection threshold with MOVPE while the MBE sample shows a concentration of traps of the order of $10^{14} cm^{-3}$ in a wide range of energies.

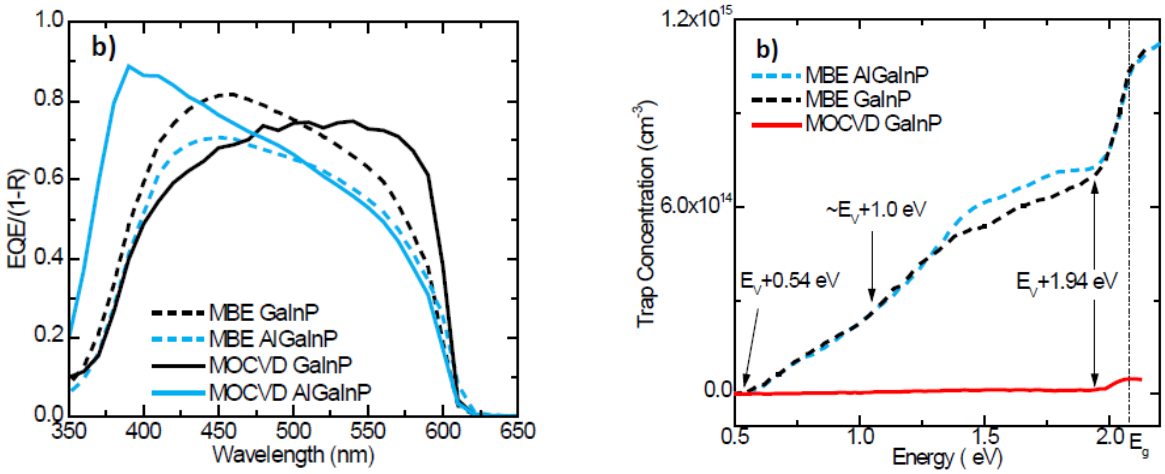

(a) (b)

Figure 4.5: Comparison of MBE and MOVPE GaInP solar cells. a) EQE of the cells. b) Trap concentration measured with DLOS. From [119].

4.1.2 Cathodoluminescence study

Effect of the doping and the passivation of GaInP:

We already pointed out the possible detrimental effects of Be doping on the GaInP material. Here, we study by CL the impact of Be doping on the optical properties of GaInP.

Four samples were grown by MBE, they comprise a 5 nm AlInP front passivation layer and a 200 nm GaInP layer. Two samples are Be doped at a concentration of p= $2.10^{17} cm^{-3}$. The two others are nominally undoped. One undoped sample and one doped sample have a rear passivation consisting in a 50 nm thick AlInP layer. The other two samples are not passivated at the rear. The details of this series are available in Table 4.1.

The cathodoluminescence spectra were measured at room temperature and at 10 K. Figure 4.6 displays the spectra measured at room temperature (red curves are undoped samples; black curves corresponds to p-doped samples; dash line: passivated samples; solid lines: samples without rear passivation). Be clearly degrades the PL intensity of the samples. Without rear passivation, integrated intensity is 24 times higher for the intrinsic sample compared to the Be-doped sample. A factor 8 remains between intrinsic and doped samples when the back-side is passivated.

Sample	p-doping at $2{\cdot}10^{17}$ cm^{-3}	Rear passivation AlInP 50 nm	CL integrated intensity $*10^4$ (A.U)
232	x	yes	231
233	x	x	21
234	Yes	yes	9,7
235	yes	x	2,6

Table 4.1: Samples details for the study of doping and rear passivation effect. Comparison of the integrated CL intensities.

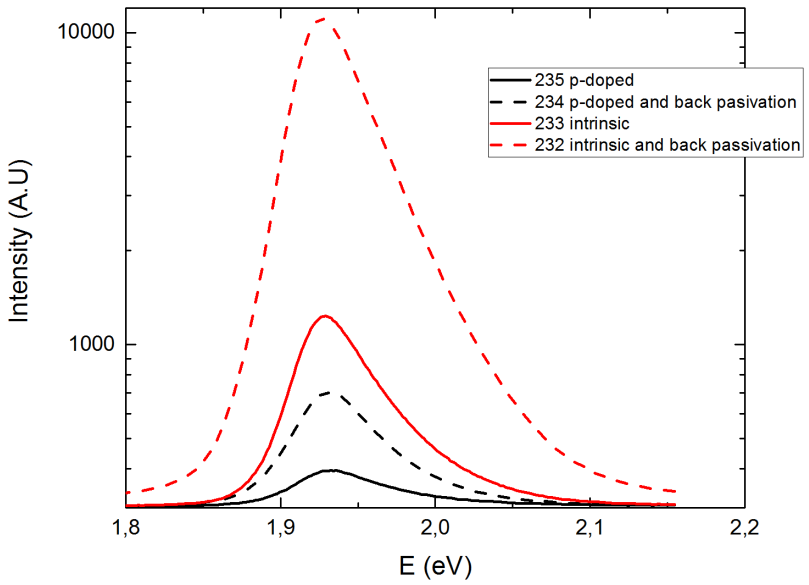

Figure 4.6: CL spectra measured at 300 K. Effect of Be doping and rear passivation with AlInP.

The rear passivation effect, by the AlInP layer improves the CL intensity significantly. This indicates that carriers, generated by the incident electron beam, reach the bottom interface of the GaInP layer. Without AlInP barrier significant recombination can occur at the GaInP/ GaAs interface and most probably at the GaAs substrate surface (despite substrate preparation, this interface may present significant defect density). This emphasizes the role of the BSF in preventing recombination at the rear of the structure and in improving the solar cells photoconversion. In the previous Chapter, we could not evidence this effect from the analysis of the cell performances, because this recombination was not an important limitation due to the short diffusion length of carriers in the base layer.

Comparison of GaInP with AlGaAs:

During this campaign of CL measurements, we compared GaInP with potential material for the tandem cells: AlGaAs. Figure 4.7 compares the CL of the two alloys at low temperature (10 K). GaInP presents multiple peaks, the bandgap emission at 1.953 eV and three peaks at lower energy (around 1.90, 1.85 and 1.75 eV).We already noted multiple peaks in the PL emission of GaInP at low temperature in Chapter 2. As compared to PL, CL reveals more contributions, in particular, the lowest energy peak was not visible in PL. This is probably due to the CL excitation which generates more carriers than PL.

In the AlGaAs spectrum, three contributions can be identified, then the luminescence decreases exponentially at lower energies, revealing a tail of states in the forbidden band..

At this point, it is difficult to predict which alloy is preferable for the top-cell of the tandem device.

Comparison of MBE with MOVPE

A first comparison of luminescence properties of MBE- and MOVPE- grown GaInP samples was performed with CL. The samples have an identical structure (comprising front and rear passivation). Low temperature spectra are displayed in Figure 4.8 with normalized intensity. MOVPE sample emission peak is at 1.973 eV, while MBE sample emission occurs at 1.958 eV. The high energy peak of luminescence of the MOVPE sample is characteristic of disordered GaInP.

Both samples present a second peak at lower energy, about 25-30 meV below the main peak emission

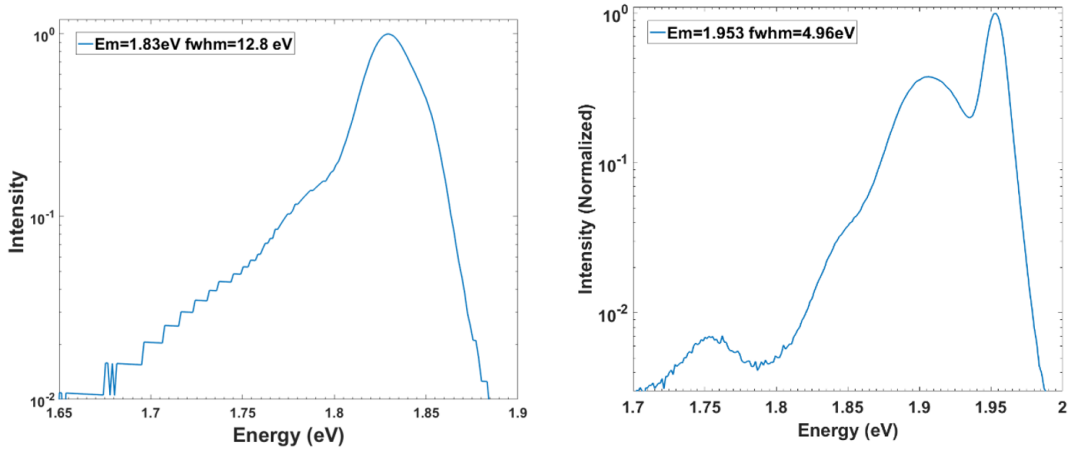

(a) (b)

Figure 4.7: Comparison of the CL spectra of a) AlGaAs and b) GaInP measured at 10 K.

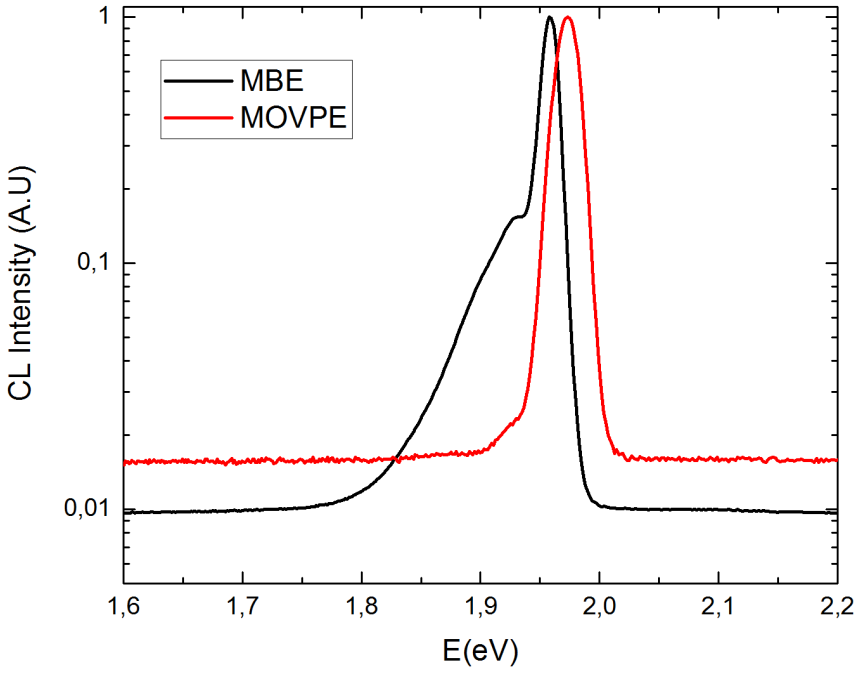

Figure 4.8: CL spectra measured at 10 K for sample grown with the two epitaxy methods compared.

corresponding to the bandgap emission. This emission can be attributed to impurities introduced in the alloy during the growth. For the MBE sample the impurity peak has an emission 10 times weaker than the peak attributed to the bandgap. For the MOVPE sample this ratio is of two orders of magnitude. Nevertheless, the MBE sample has a higher CL intensity than the sample grown with MOVPE, see Table 4.2.

	CL peak position at 10 K (eV)	Integrated Intensity (A.U)	CL peak position at 300 K (eV)
MOVPE	1,973	44010	1,90
MBE	1,958	57178	1,88

Table 4.2: Details on the CL measurement at 10 K and 300 K.

The evolution of the CL with the temperature, from 10 K to 300 K, was also investigated (Figure 4.9).

For the MBE sample the lower energy peak quickly quenches. The temperature dependence of its bandgap emission position follows a Varshni law. Significant broadening of the emission occurs at room temperature. The evolution of the CL with the temperature is very similar to the observations reported Chapter 2 for the optimal growth conditions.. The impurity peak is more pronounced with CL, probably due to higher injection conditions (bandgap emission was 100 times higher than impurity peak with PL). Another difference concerns the intensity variation with temperature: the intensity is reduced by a factor of 105 between 5 K and 300 K in PL, while it is halved with temperature in CL (ratio from spectra in Figure 2.14 for PL and Figure 4.9for CL).

The MOVPE sample exhibits a similar behavior, except that the impurity peak is weaker at low temperature.

Thus, we can retain that the MOCVD-grown GaInP sample has incorporated less impurities than the MBE sample. The MOCVD sample seems to be a random alloy with no severe localization effect. MBE sample exhibit more CL intensity, suggesting similar material quality to MOVPE grown GaInP despite a notable impurity incorporation.

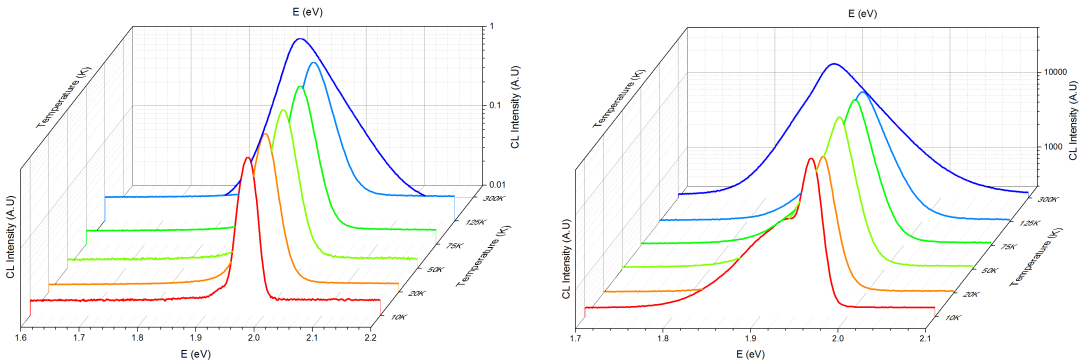

(a) (b)

Figure 4.9: CL spectra measured at different temperatures. a) Sample grown by MOVPE. b) Sample grown by MBE.

4.1.3 Time-resolved fluorescence study of carriers transport

Carriers transport and dynamics in semiconductor

In semiconductors, carrier recombination mechanisms are Shockley-Read-Hall recombination, radiative recombination and Auger recombination, as illustrated in Figure 4.10. In direct bandgap semiconductors, such as GaInP, the most common recombination process is the radiative recombination where an electron-hole pair recombines and emits a photon. During the Shockley-Read-Hall mechanism, a carrier gets trapped by a defect state within the gap, a carrier of opposite charge moves to the same defect level and causes the recombination. Auger recombination involves three particles, an electron-hole pair recombines and the corresponding energy is transferred to another electron.

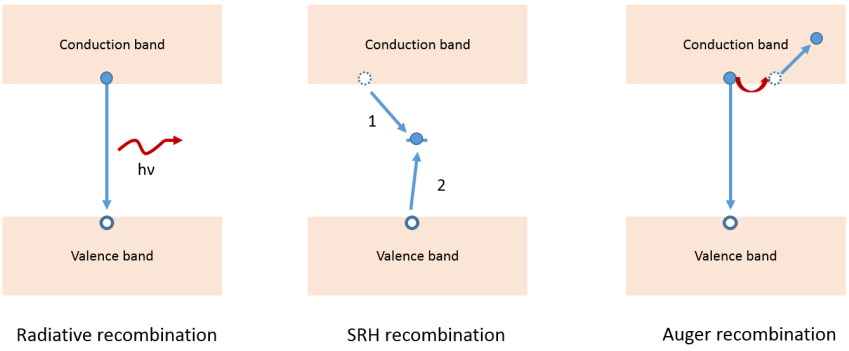

Figure 4.10: Different recombination mechanisms in semiconductors.

These phenomena result in finite lifetime of photogenerated carriers in the solar cells. Losses of carriers due to radiative recombination is solved through light trapping in the cell which permits the reabsorption of the photons emitted by photocarrier recombination. Other recombination processes are pure losses for the photocurrent of the cell. The lifetime of generated carriers and their mobility determine their diffusion length in semi-conductors. In Chapter 3, we assumed have concluded that the main limitation of our cells is related to the fact that the diffusion length of minority carriers in the base layer is too short. In this subsection, we study the transport dynamics of photocarriers by time-resolved fluorescence imaging (TRFLIM). We will compare GaInP samples mimicking our base layer material grown by MBE or MOVPE.

Experiment details

The TRFLIM setup allows to map the luminescence spatially, and record its evolution with time. The sample is illuminated with a 550 nm laser via an objective that focuses the beam to a $1\mu m$ spot. The laser is pulsed (6 ps pulse) with a frequency of 1 MHz; a CCD camera, triggered by the laser pulse, records the luminescence with a resolution of 750 ps.

When illuminated with the laser pulse, carriers are generated in the sample, they diffuse and eventually recombine. As illustrated Figure 4.11 the setup permits to record $I_{PL}(r,t)$, the PL intensity in space and time. The number of carriers generated with the excitation pulse is known from the fluence of the laser pulse. Fitting the recorded $I_{PL}(r,t)$ to the continuity equation (Equation 4.2) applied to minority carriers, one can extract carriers lifetime and diffusion coefficient. Auger recombination was neglected: this mechanism involves three particles and thus becomes significant at high doping levels or in high injection regime. In this study, all sample are doped below $5.10^{17} cm^{-3}$ and the injection regime generate carrier concentration similar to 1 sun exposition conditions.

PL intensity is proportional to the square of the carrier concentration, indeed radiative recombination is described by the term $R_{eh}.n^2$ in Equation 4.2. The carrier concentration at given moment and position follows the continuity equation (Equation 4.2) which include a carrier diffusion term $D_n.\nabla n$, and the SRH recombination term, $\frac{n}{\tau_n}$.

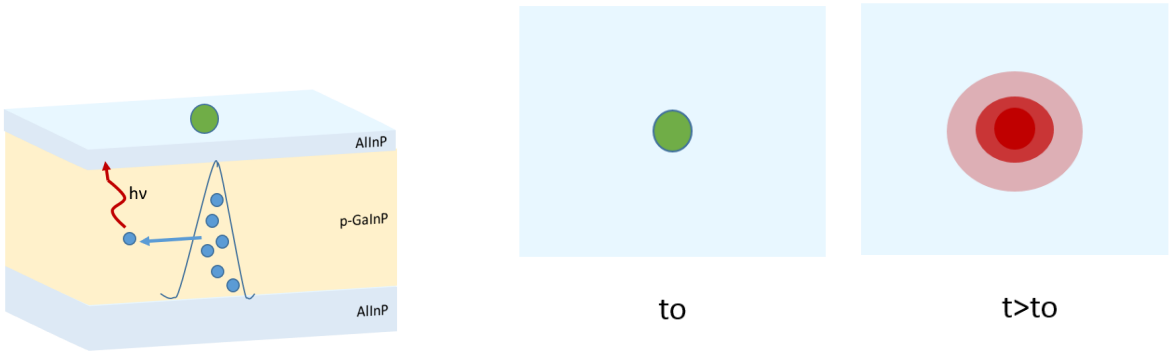

(a) (b)

Figure 4.11: Illustration of the TRFLIM experiment. a) The focused laser beam generates carriers in the GaInP. Carriers diffuse in the layer and eventually recombine radiatively, allowing the study of diffusion and recombination of carriers by mapping the sample luminescence. b) Top view of the sample, at t_0:carrier generation with green laser; at t>t_0: luminescence from the sample is recorded. I_{PL} depends on the distance from initial laser spot and on the delay time after the excitation pulse..

$$I_{PL}(r,t) \propto n^2(r,t) \tag{4.1}$$

$$\frac{\partial n}{\partial t} = D_n.\nabla n - \frac{n}{\tau_n} - R_{eh}.n^2 \tag{4.2}$$

where D_n is the diffusion coefficient for electrons and R_{eh} is the radiative recombination coefficient.

The carriers concentration is assumed to be homogenous in depth (GaInP is only 200 nm thick) and initial conditions are fixed with the spot of laser pulse. We can then fit the experimental $I_{PL}(r,t)$ to Equation 4.2 and deduce D_n and τ_n. Bercegol et al developed this method to the study both the photo-recycling effect and the carrier transport in perovskites [120].

For this experiment, a passivated GaInP structure with doping level identical to the base layer was compared to sample with p-doping levels of $5.10^{17}cm^{-3}$,$5.10^{16}cm^{-3}$ and $1.10^{16}cm^{-3}$ grown with MOVPE. Figure 4.12 displays data acquired at different times for one the MOVPE sample, one notices that the luminescence spreads with time.

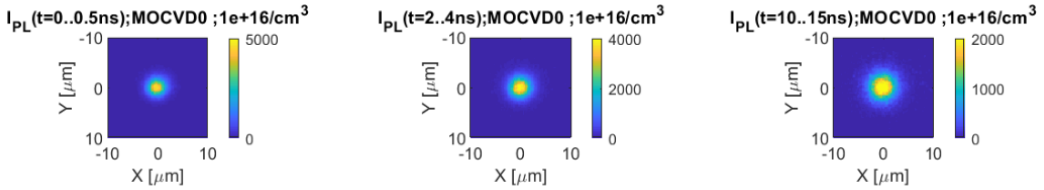

Figure 4.12: Plot of the acquired map of phtoluminescence intensity with time. The emission spreads with time and will then vanish.

The measurement was performed for two photon fluences: low injection corresponds to 3.10^5photons/pulse generating a $10^{17}cm^{-3}$ carrier concentration in the GaInP, medium injection corresponds to 3.10^6 photons/pulse generating $10^{18}cm^{-3}$ carriers. These generation regimes are close to the one-sun injection regime. Table 4.3 gathers the results for the four samples. MOVPE sample doped at $5.10^{17}cm^{-3}$ which exhibits a lower PL intensity than the others, could not be fitted at low excitation. Input parameters of the fit

are majority carriers mobility, extracted from literature for Zn-doped MOVPE samples, GaInP radiative recombination coefficient fixed at $5.10^{-11} cm^3.s^{-1}$[121], and p-doping level of the samples.

Résolution équation de continuité	MOCVD		MBE		MOCVD			
Coeff diffusion majority carriers [cm2/s]	170		850		1640		8200	
Doping level (cm-3)	5,00E+17		1,00E+17		5,00E+16		1,00E+16	
Laser pulse flux	low flux	mid flux	low flux	mid flux	low flux	mid flux	low flux	mid flux
Temps de vie SRH τ_n [ns]	NR	1,6	2,3	1,9	1,8	1,8	2,3	1,8
Coeff diffusion min Dn [cm2/s]	NR	0,058	0,29	0,32	0,43	0,69	0,38	0,53
Minoritaire : longueur de diffusion Ln [nm]	NR	96	258	247	278	352	296	309

Table 4.3: Results obtained with TRFLIM transient fit.

Carrier lifetime

MBE sample exhibits a relatively good carrier lifetime: **2.3 ns** determined for low fluence and 1.9 ns determined at medium fluence. For MOVPE grown samples the lifetimes determined with the medium flux are 1.8 ns for sample doped in the $10^{16} cm^{-3}$ range and 1.6 ns when doped at $5.10^{17} cm^{-3}$. At low fluence, **1.8** ns is obtained for sample at a $5.10^{16} cm^{-3}$ doping level and **2.3 ns** for sample doped at $1.10^{16} cm^{-3}$.

The carrier lifetime τ_n, tends to decrease slightly with the doping level, as expected since more majority carriers are present for minority carriers recombination. . An interesting result is the long lifetime determined for the MBE sample. Figure 4.13 gathers the carrier lifetimes in GaInP reported in the literature. The lifetime of our MBE sample is comparable to the best values reported for MBE grown material. Although it is under the value reported for MOVPE-grown GaInP, which is 5.4 ns in Figure 4.13, better values are probably achieved by the PV reference laboratories.

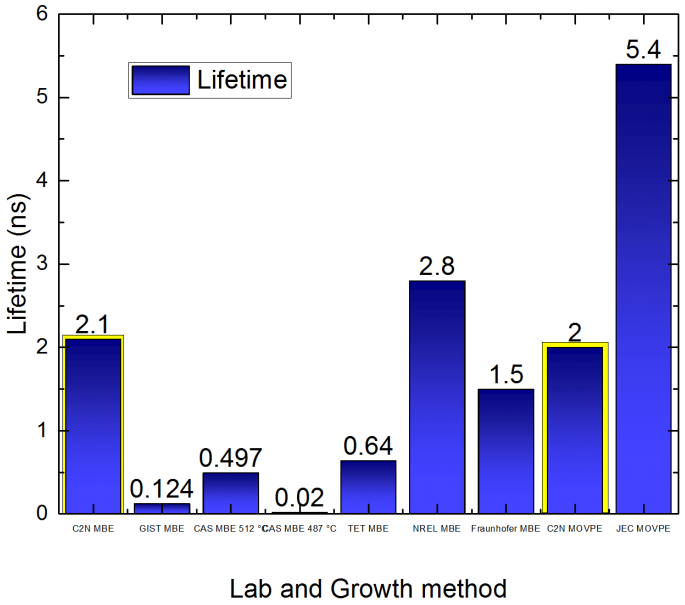

Figure 4.13: Comparison of carrier lifetime in GaInP for various laboratories and growth methods.

Figure 4.14 associates to these lifetimes, the photoconversion efficiencies of GaInP single junctions (when available) reported by the same laboratories. Surprisingly, there is a weak correlation between these two parameters, efficiency and lifetime. In particular, regarding our value of minority carrier lifetime, we could have expected a better efficiency of our cell. Indeed record MBE cell only has a carrier lifetime of 0.5 ns. This suggests that the small diffusion length in the base layer of our cells , is limited by the mobility of generated carriers.

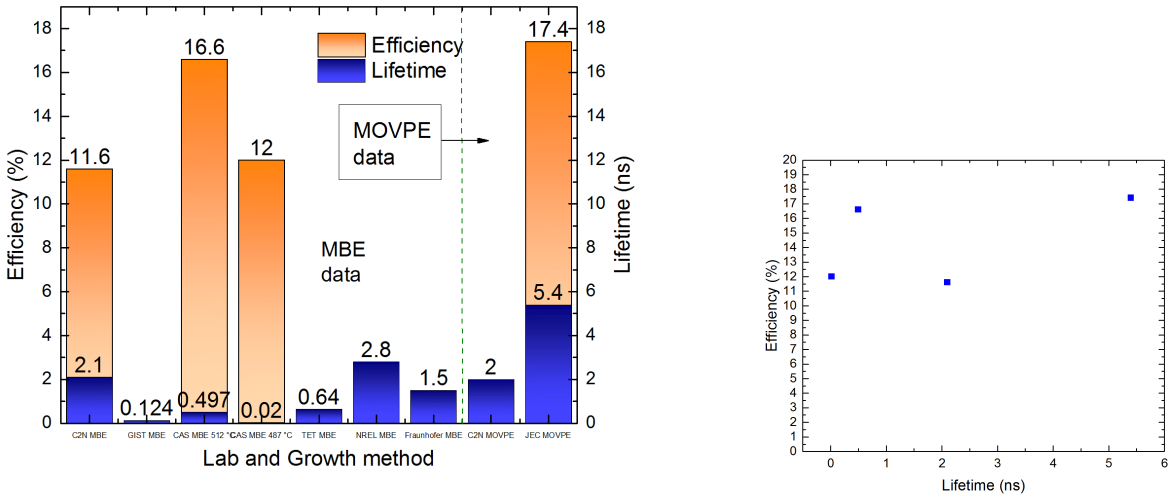

(a) (b)

Figure 4.14: Lifetimes and associated efficiency for GaInP single junction cells.a) addition of the efficiencies reported to the lifetimes values presented in Figure 4.13. b) Efficiencies of GaInP cells depending on their carrier lifetime, no correlation exhibited.

Minority carriers mobility:

In order to compare with values from the literature [97] and expose the poor mobility determined for this batch of samples, Figure 4.15 displays the minority carriers mobility,μ_n, calculated from the diffusion coefficient of Table 4.3 with the Einstein relationship:

$$\mu_n = \frac{D_n.q}{k_b.T} \tag{4.3}$$

Where q is the elemental charge, k_b is the Boltzmann constant and T is the temperature.

For same doping levels, minority carrier mobility is two orders of magnitude lower than the values reported by the NREL (MBE-grown GaInP samples). This huge difference explains the ratio of more than 10 between the diffusion length of 258 nm in our material and that of 2.9 µm for the NREL material. This drastically impacts the cell efficiency: the diffusion length in NREL material is twice the thickness of their GaInP cells, it thus guarantees the collection of all carriers generated within the cell.

$$L_n = \sqrt{D_n.\tau_n} \tag{4.4}$$

The diffusion length L_n is calculated from the fitted parameters with Equation 4.4

The MOVPE samples used in this study exhibit slightly higher mobilities than the MBE sample, resulting in diffusion length of the order of 350-310 nm. Unfortunately we could not find data on the mobility of minority carrier associated to Zn-doped MOVPE-grown GaInP. It is therefore hard to compare our material with state of the art GaInP cells. The GaInP single junction cells reported by NREL are grown by MOCVD and their carrier mobility might be at least as high as the values reported for their MBE material. Carrier

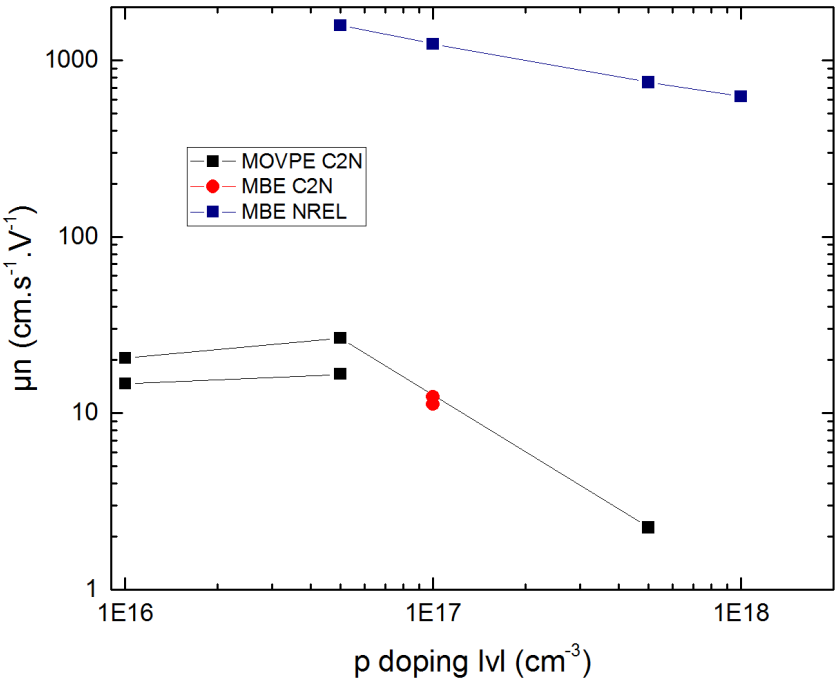

Figure 4.15: Comparison of minority carrier mobilities in p-doped GaInP. Data from literature [97] and our data deduced from TRFLIM measurements.

lifetime of 10 ns was reported by Haegel et al and Takamoto et al [96, 122] in MOVPE-grown GaInP. These figures would be consistent with a carrier diffusion length of about 6 µm in the state-of the-art GaInP cells, a value well above that we inferred for GaInP cells.

With this TRFLIM study, we further investigated the properties of our GaInP material. Our growth optimization (Chapter 2) led to satisfying carrier lifetime (around 2 ns). On the contrary, the minority carrier mobility is too low. This parameter limits the carrier diffusion length to about 260 nm, a distance smaller than the thickness of the neutral region in the base of our cells. This result is consistent with our simulations in section 3.3.1.

4.2 Perspectives related to Phosphorus sources

Improving the carrier mobility requires to minimize impurity incorporation during GaInP growth. Two different types of impurities can be distinguished, impurities responsible for residual doping of the alloy and impurities acting as traps which can favor non-radiative carrier recombination.

Oxygen incorporation has been discussed in Chapter 2. It could be related to Be doping via Be-O complex formation, which would reduce the Be-doping efficiency. The influence of the phosphorus source on the concentration of oxygen incorporated in GaInP layer has also been studied by Nadja et al. [85]. The standard MBE sources, corresponding to our configuration, are elemental solid sources (SSMBE). Gas source MBE (GSMBE) consists in replacing the group V solid sources with gas sources (phosphine and arsine). Nadja et al had an MBE offering both possibilities. They used either a GaP decomposition cell or phosphine gas as the P source for AlGaInP growth. Figure 4.16 shows the oxygen concentration profile in their samples measured by SIMS. It evidences that the GaP solid source causes about an order of magnitude higher incorporation of Oxygen than the gas source. Removing the background contribution, they measured an oxygen concentration of $2.10^{16} cm^{-3}$ when solid source is used while the concentration was below detection threshold when gas source MBE was used.

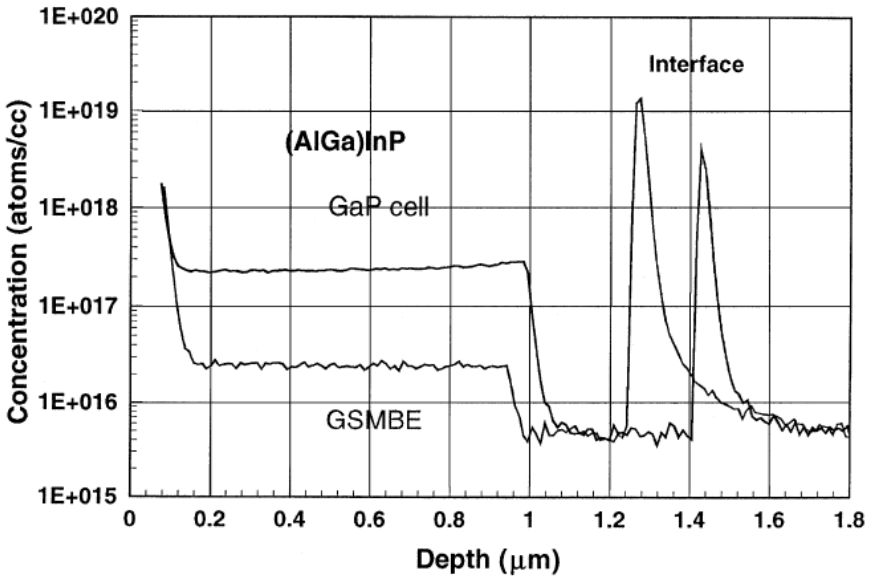

Figure 4.16: Impact of the type Phosphorus source on the O concentration incorporated in the AlGaInP. "GaP cell" corresponds to SS-MBE configuration, phosphine gas is used in GS MBE. From [85].

Hence, impurity incorporation in GaInP must also strongly depends on the type of P source which is used. This may be one of the reasons for the gap of performance between MBE- and MOVPE- grown materials. In our case, we use an elemental P source in the form of a red phosphorus ingot of 6N nominal purity. Moreover, elemental P source must be used with a cracking zone which can generate additional contamination. Indeed, increasing the cracker temperature from 800 to 1000°C can result in a multiplication by ten of the O concentration [123] .

The presence of n-type impurities in red phosphorus source is known for a long time. In 1985, Martin et al noticed that for SSMBE-grown InP, no residual doping below n=$10^{16} cm^{-3}$ was ever reported [124]. They identified S and Si as the impurities causing this high level of residual doping (concentration as high as $10^{16} cm^{-3}$ for S and $10^{15} cm^{-3}$ for Si). Using GS-MBE, Yokotsuka et al could obtain p-doping levels in GaInP and AlInP three times higher than the maximum p-concentration obtained with SSMBE [125].

Solid sources purity is graded in "N"s, a 2 Ns phosphorus source has a purity of 99%, in fact N corresponds to the number of 9s in the material purity percentage. As a second example a 99.999% pure ingot is graded 5N. In our case, the phosphorus cells was charged with 6N P ingots, which was also the case of Martin et al..

Considering the 6N purity of the elemental P source we used, a simple calculation indicates that $2.21.10^{16}cm^{-3}$ impurities coming from the P flux, could be incorporated in the III-P lattice. This concentration is of the same order of magnitude than the residual doping level of $1.10^{16}cm^{-3}$measured in our GaInP material. Taking into account that S and Si are known contaminants of solid phosphorus and n-type dopants of III-Vs, these impurities are likely responsible for the residual doping of our GaInP layers.

This highlights the importance of the phosphorus source on the limitation observed in our cells. Today, 7N grade red phosphorus is available on the market. If the use of such material results in a reduction of the GaInP residual doping level by a factor of 10, we would be able to reproducibly dope the base in the $10^{16}cm^{-3}$. The carrier mobility should be improved accordingly, with beneficial effect for the PV efficiency of the cells

7N grade phosphorus ingots are already purchased, but were unfortunately not loaded in the growth chamber during the PhD. A long interruption is forecasted for moving the MBE machine in the new IPVF's building. It was decided to wait for this long interruption before loading a new phosphorus charge in the cracker cell and we shall see in the future how the change of the phosphorus purity improves the GaInP cells quality.

4.3 Overcoming the GaInP base limitations: the heterojunction

4.3.1 The heterojunction idea

Having noticed the current limitations of GaInP material used in this work and being aware that further improvement requires a maintenance of the MBE system that would interrupt our activities for a long time, another path was investigated for the improvement of the base of the cells.

Within project E, my colleague Ahmed Ben Slimane was focusing on AlGaAs solar cells. We have seen in the first chapter that AlGaAs and GaInP are both interesting candidates for the elaboration of wide-bandgap top cell for double junction tandem solar cell based on Si. Although state-of-art GaInP cells have reached better efficiencies, AlGaAs cells offer optimal an bandgap value for 2-terminal tandem junction solar cells on Si. Moreover p-GaInP has been identified as the limiting factor of the cells grown in our MBE.

In parallel to the GaInP cell, an AlGaAs cell was developed. Best cell has a **9.93%** efficiency obtained with a FF of **0.82**, Voc of **1.139** V and Jsc of **10.62** $mA.cm^{-2}$, The Al concentration of the AlGaAs layer was of 28%.

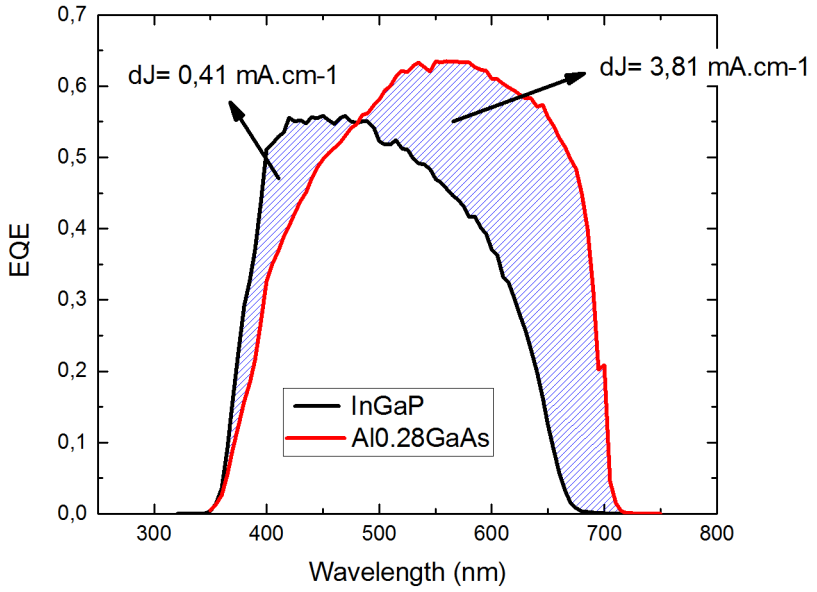

Figure 4.17: Comparison of the EQE of the GaInP and AlGaAs cells fabricated in the project (cells without ARC).

Looking at the EQE, which is a good figure of merit of the solar cells, Figure 4.17 shows the differences between the AlGaAs and GaInP cells. The two structures are: our reference GaInP cell and an AlGaAs cell comprising $Al_{0.7}Ga_{0.3}As$ passivation layers and an $Al_{0.28}Ga_{0.72}As$ absorber composed of a 100 nm Si-doped emitter and a 1 μm Be-doped base.

According to the EQE of Figure 4.17 , beyond 500 nm wavelength, the AlGaAs cell performs better than the GaInP cell. First, the AlGaAs cell absorption drops at higher wavelength due to its smaller bandgap (1.77 eV at this absorber composition compared to 1.85 eV for the GaInP absorber). Then, the photoconversion in this high wavelength range is more efficient than in the GaInP cell. Indeed, the EQE of the AlGaAs cell exhibits a steep drop near the absorption limit and a value around 60% from 500 to 700 nm.

In the short wavelength range, the GaInP cell performs better, having both steeper slope and higher EQE value than the AlGaAs one. This results partly from the front cell optimization of the GaInP cell. Quantifying the differences in current (the dashed area in the EQE spectra) with Equation 3.5 , the AlGaAs cell provides 3.81 $mA.cm^{-2}$ more than the GaInP cell above 500 nm. In the spectrum range below 500 nm

the GaInP generates 0.41 $mA.cm^{-2}$ more than the AlGaAs cell.

The comparison of the EQEs reveals that the problem of photo-conversion at long wavelengths is not observed with the AlGaAs cell. On the contrary, the better response of the GaInP cell in the short wavelength range suggests a lower quality of the n-doped AlGaAs compared to n-doped GaInP. Combining the best layers of the two structures is an interesting solution to improve the PV efficiency.

The two alloys present the advantage of being almost lattice-matched to GaAs. The usual growth temperature of AlGaAs is higher than that of GaInP, but the temperature can be easily changed before forming the interface between these alloys. To this end, a short growth interruption can be applied, during which one can also switch the group V fluxes.

In the following section, we will focus on the electronic properties of these alloys and to understand their impact on the differences observed between AlGaAs and GaInP single junction cells.

4.3.2 Complementarity of AlGaAs and GaInP

In our growth configuration, the p-GaInP alloy exhibits low carrier mobility and therefore short diffusion length in the cells. We have seen that Be and P may play a significant role in the degradation of the alloy quality.

On the contrary Be doping in AlGaAs does not present any particular problems. This is another sign pointing P as the main source impurities in GaInP, since this element is absent in AlGaAs . Comparing our Hall effect characterizations of Be-doped III-V alloys in Figure 4.18 we note:

- Lower p-doping levels are accessible with AlGaAs, $2.4.10^{16} cm^{-3}$ in comparison with $2.10^{17} cm^{-3}$ in GaInP.
- For identical doping level, majority carriers mobility is higher in AlGaAs than in GaInP. Moreover since lower doping levels are accessible with AlGaAs, one can benefit from mobilities significantly higher than in our GaInP base.

Hence, Be-doped AlGaAs is an attractive alternative to Be-doped GaInP for the base layer of solar cells.

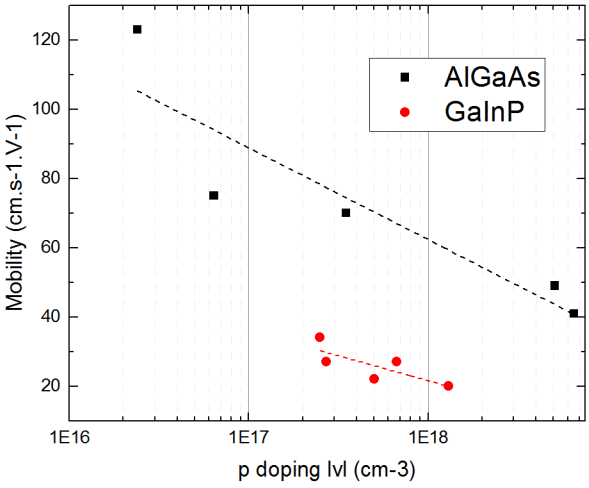

Figure 4.18: Mobility of majority carriers in Be-doped III-V alloys measured by Hall effect.

On the other hand, Si-doping of AlGaAs is known for being a source of degradation. Watanabe et al observed that Si-doping of the AlGaAs causes the introduction of DX centers in the alloy [126]. The concentration of these defects increases with the Si-doping level and the Al content. Concentrations of DX centers as high as $10^{18} cm^{-3}$ were measured for an $Al_{0.34}GaAs$ with a free electron concentration of

$3.10^{17} cm^{-3}$[126]. Therefore, a significant concentration of these defects may degrade the properties of the $Al_{0.28}GaAs$ emitter and the $Al_{0.7}GaAs$ window layer of the cells. Moreover, the Si doping efficiency depends on the $Al_xGa_{1-x}As$ composition. Around this composition of 0.34 in Al, Si-doping efficiency was found to decrease by an order of magnitude in comparison to other alloy compositions [127] .The presence of inactive Si impurities is a factor which degrades the free carrier mobility. The emitter composition in AlGaAs cells (xAl= 0.38 to xAl=0.24 tested) is in the range where decrease of the Si-doping efficiency is observed.

Takashi et al tested the effects of Si doping on AlGaAs properties and cells efficiency [128]. They grew p-n cells (thick n-doped base in this cell configuration) and compared two n-dopants, Si and Se. They measured the PL decay time for these two dopants. The DX centers present in the sample doped with Si cause severe degradation of the carrier lifetime (less than 0.3 ns) in comparison to the sample doped with Se (lifetime above 4 ns). Figure 4.19 shows that the degradation is also visible in the EQE of the cells. Clear decrease of the PV conversion occurs at the wavelengths absorbed in the Si-doped area (the back of the cell, i.e. long wavelengths).

GaInP does not exhibit degradation caused by Si-doping, which leads to the better performance of the GaInP cell in the short wavelengths range Figure 4.17.

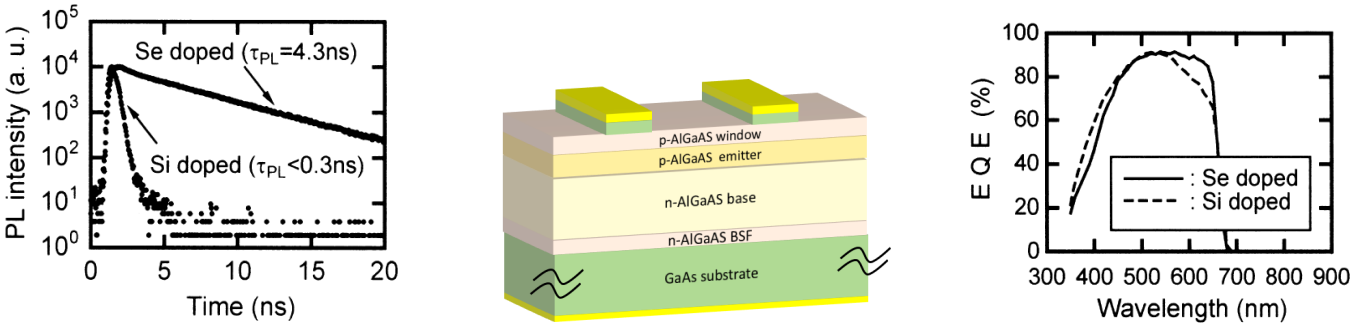

(a) From [128] (b) (c) From [128]

Figure 4.19: Influence of Si doping on AlGaAs properties, comparison with Se doping. a) Effect on the PL decay time. b) Simple sketch of the n-p cell structure used by Takahashi and al. c) EQE degradation related to the Si-doped area of AlGaAs base of the cells.

Thus, the two materials present a remarkable complementarity. Using phosphides for the n-doped layers of the cell and AlGaAs for the p-type side, we can expect great benefit for the cell photocurrent. Indeed the main recombination sources of both materials can be avoided.

However, in order to improve the PV efficiency, the heterojunction must collect enough photocurrent to compensate the shrinkage of Voc that will be caused by the band off-set at the hetero-interface and by the lower bandgap of the AlGaAs. Indeed at the Al content tested for the heterostructures, the GaInP/AlGaAs hetero-interface will present a staggered junction (with $\Delta Ec = 110$mEv and $\Delta Ev = 220$meV for a GaInP with a 1.9 eV bandgap and an $Al_{0.29}Ga_{0.71}As$ alloy with a bandgap of 1.79eV [129]), see Figure 4.20.

4.3.3 Realisation of GaInP/AlGaAs heterojunction cell

For the realization of the heterojunction, the structure of the window and emitter of the GaInP cell are grown on the base and BSF of the AlGaAs structure (Figure 4.21).

During the epitaxy we interrupt the growth interruption between the base and the emitter in order to switch the group V and adjust the Ga effusion cell and substrate temperature. Such a growth interruption might favor impurities incorporation in a critical region (the p-n junction). To minimize possible detrimental effect, we used a short interruption of 1 min.

In Figure 4.22 , the EQE of the heterojunction cell is plotted and compared with the EQE of the two homojunction cells (their structure are detailed in Figure 4.21). The heterojunction cell adds the benefits of its two components, the structure shows good conversion in the short and long wavelengths, cumulating the GaInP and AlGaAs responses.

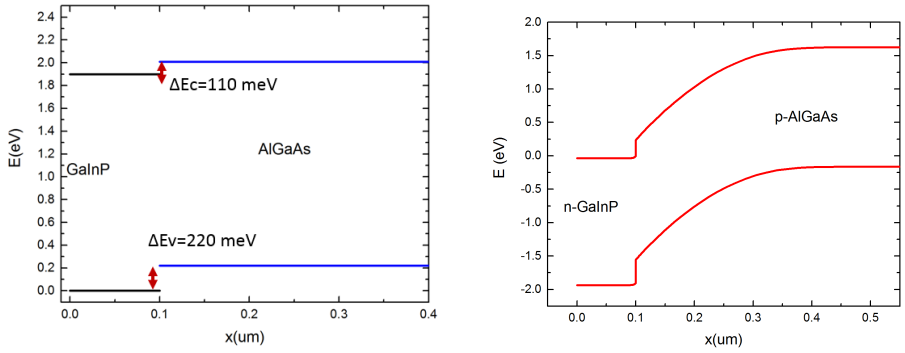

(a) (b)

Figure 4.20: a) Details on the band off-set between GaInP and $Al_{0.29}Ga_{0.71}As$. b) Band diagram at the hetero-interface for GaInP doped at n=$2.10^{18}cm^{-3}$ and AlGaAs doped at p=$2.10^{16}cm^{-3}$.

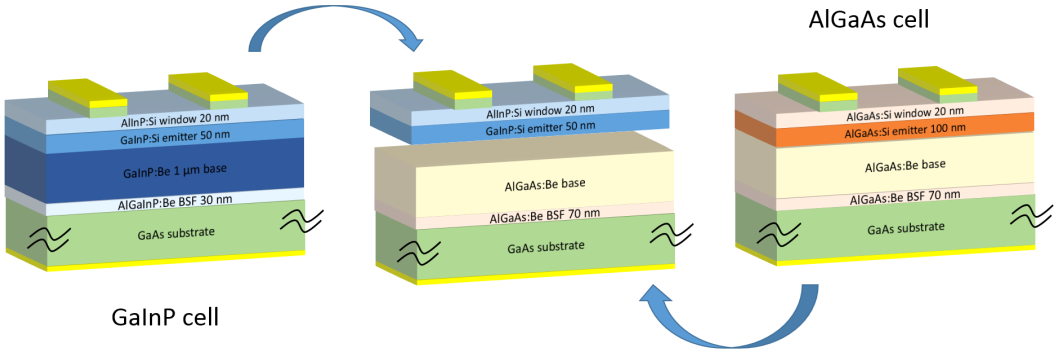

Figure 4.21: The Heterojunction combines the front of the GaInP cell with the rear of an AlGaAs cell.

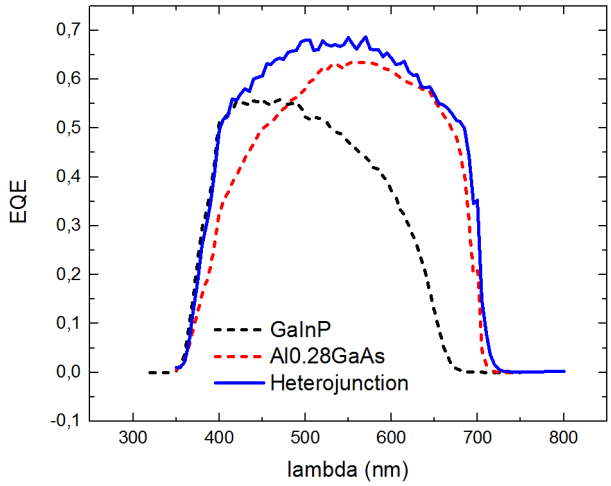

Figure 4.22: EQE of the GaInP, AlGaAs and heterojunction cell.

We then studied the influence of the $Al_xGa_{1-x}As$ base composition on the heterojunction cell performances. Increasing the Al content in the alloy induces an increase of the bandgap Eg, this is of interest to improve the Voc. On the other hand, higher AlGaAs bandgap reduces the absorption range and thus the Jsc. Let us recall that AlGaAs offers the possibility to approach the optimal value of 1.73 eV for tandem application with Si cell, for an Al content of 0.25.

$Al_xGa_{1-x}As$ cells with x= 0.37, 0.28 and 0.25 were fabricated. Figure 4.23 show very clearly the shift of the absorption edge induced by the reduction of the Al content. Table 4.4 gives more details on the cells characteristics of these cells which do not include any anti-reflection coating. With xAl=0.37 the bandgap of AlGaAs is close to the GaInP bandgap and only little improvement of Jsc is observed. Lowering the Al content provides remarkable improvement of the Jsc which reaches 12.05 $mA.cm^{-2}$ at 0.25 Al content.

On the other hand, the Voc decreases with the bandgap energy, lowering from 1.26 V at xAl=0.37, to 1.247 V for xAl=0.25 Al content. In other words, this Voc reduction is only 13 meV while the AlGaAs bandgap decreases by 150 meV. This translates into a remarkable reduction of the Woc: 0.624 V for xAl=0.37 to 0.487 V for xAl = 0.25 (in the very best III-V solar cells, Woc $\approx$ 0.4 V). Besides, the FF increase between xAl = 0.37 and xAl = 0.25 indicates that the alloy quality improves with the reduction of the Al content (see in Table 4.4).

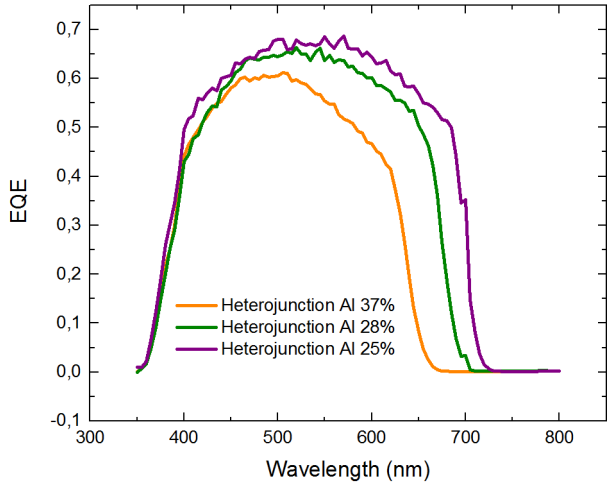

Figure 4.23: Influence of the AlGaAs composition on the EQE of heterojunction cells.

	GaInP cell	Heterojunction cells		
Al content	-	xAl=0.37	xAl=0.28	xAl=0.25
Jsc ($mA.cm^{-2}$)	8.15	8.78	11.46	12.05
FF	0.82	0.77	0.81	0.82
Voc (V)	1.3	1.26	1.26	1.247
Efficiency	**9.66**	**8.5**	**11.7**	**12.3**
Eg (eV)	1.89	1.884	1.771	1.734
Woc (V)	0.59	0.624	0.511	0.487

Table 4.4: Characterization results for comparison of GaInP cell and heterostructure cells with various $Al_xGa_{1-x}As$ composition.

With 37% of Al, the improvement of Jsc is not sufficient to compensate from the Voc reduction and the heterojunction does no surpass the GaInP cell. At lower Al content, the current increase is significant and Voc is only slightly penalized. This results in an important boost of efficiency and Woc reaches 0.487 V.

Figure 6 shows that the increase of Al content does not only shift the absorption edge of the cell to short wavelengths. Indeed, in the 450-600 nm wavelength range, the EQE lowers significantly with the Al content.

This is probably related to the DX centers concentration or/and Oxygen incorporation which increase with the Al content of the alloy[130]. Acting as carrier traps and non-radiative recombination centers, these punctual defects degrade the carrier lifetime [131, 130]. and thereby the PV efficiency. This might be at the origin of the improvements observed when decreasing the Al content of our heterojunction cells.

In conclusion, the GaInP/AlGaAs heterojunction appears as a very effective way to circumvent the base limitations that we faced in our GaInP PV cells.

4.3.4 Towards a state-of-the-art MBE-grown III-V cell for tandem on Si

We evidenced that the heterojunction is a promising architecture for the elaboration of a performant III-V top cell. Further optimization, described elsewhere [132], allowed to improve the cell efficiency much farther.

In section 3.2.5, we have seen that inserting an intrinsic layer in the middle of the p-n junction could be beneficial if the gain of photocarrier collection compensates the negative impact of this intrinsic layer on the Voc and FF. This was not the case when the residual doping level of the "intrinsic" layer was too high.

The $Al_{0.25}Ga_{0.75}As$, has been selected for its low residual doping and for the range of low p-type doping levels which is accessible in this alloy. It was therefore very relevant to test the insertion of an undoped region as well as a low p-type doped region (p=$2.10^{16} cm^{-3}$) in the AlGaAs base. Such cells were fabricated, they comprise a 50 nm GaInP emitter, a 100 nm AlGaAs i-layer and a 900 or 1900 nm AlGaAs base. A 65 nm SiNx anti reflection coating was sputtered on the cells. Two devices were certified by the Fraunhofer ISE calibration laboratory, Figure 4.24 displays the certified results.

The cell with a 2-µm-thick base has the following characteristics: Jsc reaches 17.66 $mA.cm^{-2}$, for a FF of 84.37% and a Voc of 1.254 V. This thicker cell has then an efficiency of 18.7%. The cell with a 1-µm-thick base has a lower Jsc of 16.33 $mA.cm^{-2}$, FF 86.06%, and a Voc 1.292 V. This thinner cell has thus an efficiency of 18.16%.

We see that high performances have been obtained. Remarkable figures are, for instance, the FF of 86% and the Woc of 0.44 V of the 1-µm-base cell. Increasing the base thickness does improve the photocurrent, indicating that absorption of light above the bandgap is not complete in the 1-µm-base cell. Although for the 2-µm-thick cell, the decrease of FF and Voc indicates that recombination of minority carriers in the bulk limits the cell performance. The optimal thickness of the base probably lies between 1 and 2 µm.

With this heterojunction architecture, we establish a record of efficiency for a MBE-grown III-V cell designed for a tandem cell based on a bottom Si cell: previous record was a GaInP cell with 16.6% efficiency [49]. We are confident that the 20% goal, fixed for the tandem top cell, is accessible. Indeed, there is still room for improvement: replacing our anti-reflection coating with an optimal MgF2/ZnS stack will be profitable, residual impurities in the phosphide layers could be reduced in the emitter side with a purer phosphorus source, the exact design of the heterostructure can be further optimized.

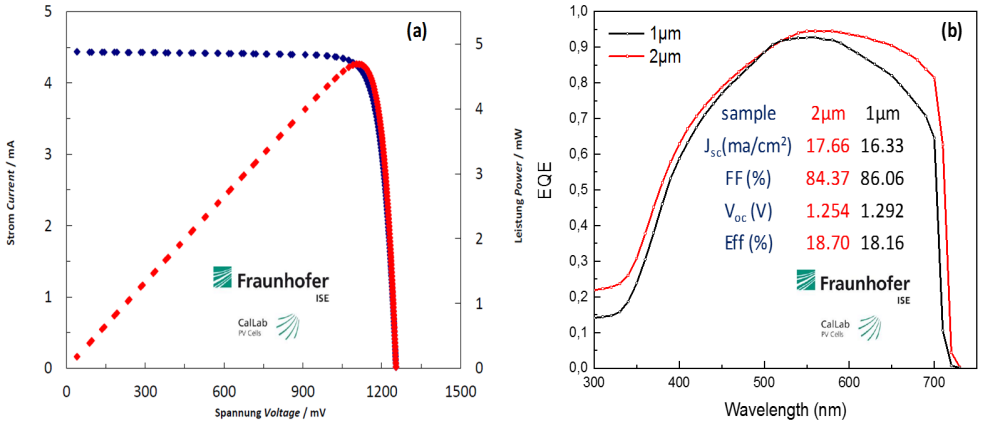

Figure 4.24: IV curve and EQE of the best GaInP/AlGaAs heterojunction cells.

Take away message from Chapter four:

- The large difference of substrate temperature between MBE and MOCVD growth of GaInP alloy, may explain the different properties of this compound elaborated by these two techniques. Annealing of MBE-grown GaInP has been tested to improve the quality of this material. No real benefit was observed on the performance of the solar cells.
- We have evidenced by PL and CL spectroscopies that Be doping degrades the GaInP properties.
- Comparing MBE and MOPVE samples fabricated at C2N, we inferred that impurity incorporation is lower with MOVPE. Nevertheless, we carried out TRFLIM on both samples and found that minority carriers have similar diffusion lengths for the two types of sample. MBE sample has a satisfying carrier lifetime of 2.3 ns.
- The mobilities of minority carrier determined by the TRFLIM experiment are low in comparison to values reported in the literature. This parameter was identified as the main limitation of the performance of our cells.
- MBE sample has as a diffusion length of 260nm, while data gathered from MOVPE samples from other laboratories indicate a diffusion length longer than 2 μm in GaInP solar cells grown by MOVPE.
- One path toward improvement of GaInP is to load an elemental phosphorus source of higher quality. It will be tested as soon as possible.
- • Heterojunction combining n-GaInP and p-AlGaAs is an effective solution to circumvent the low carrier mobility in Be-doped GaInP and the poor properties of Si-doped AlGaAs. Heterojunction cell with an efficiency of 18.7% was elaborated. This result represents the new state-of-the-art for MBE-grown single junction solar cell with a wide bandgap.

General conclusion and perspectives

Conclusion

The GaInP material which we chose for the III-V cell fabrication, was grown on GaAs and extensively studied. This alloy exhibits various properties depending on its growth conditions. Different growth temperatures and V/III ratio were tested and optimized by maximizing the photoluminescence intensity of the epitaxial layers. At a growth rate of 1 µm/h, we selected a growth temperature of 500°C and a V/III ratio of 12. For lower growth temperature, the GaInP exhibits a weaker PL intensity, dominated by transitions from impurity levels at energies below the bandgap. Moreover, at lower V/III ratio, a columnar modulation of the group III composition was observed. The amplitude of the composition change is slightly superior to 2%.

Then, we focused on the different layers composing the cell, by investigating their influence on the solar cell photoconversion efficiency. The passivation of the GaInP p-n junction with AlGaInP layer of different compositions was tested. AlInP proves to be the best material for the window by increasing the photocurrent of the cell by 2 $mA.cm^{-2}$. Indeed, AlInP offers more transparency to the wavelengths absorbed by GaInP. On the other hand, the composition of the back surface field passivation layer has little impact on the performance of the cells. Thinning the n-doped emitter from 100 nm to 50 nm also enhances the photocurrent. Placing the depleted region of the p-n junction closer to the surface, where absorption is more important, increases the number of electron-hole pairs separated and collected.

Despite further optimization of the structure of the GaInP cells, their efficiency was found to plateau at 11.6%. It appears that the photocurrent is the limiting factor of the cells and the p-doped base layer is at the origin of this effect. The introduction of non-intentionally doped layer in the structure did not improve the efficiency of the cell.

Time-resolved fluorescence imaging permitted to study the dynamic of carriers transport in the GaInP base layer. We measured a carrier diffusion length of 260 nm. This value is too short to ensure efficient collection of photo-carriers generated at the rear of the cell. However, the carrier lifetime is found to be comparable to state-of-the-art lifetimes for MBE-grown GaInP. Improving the minority carrier mobility is the road that will allow the improvement of the diffusion length and therefore the increase of photocurrent collected in the cells.

Combining the front of the GaInP cell with the rear of an AlGaAs cell is demonstrated as an effective solution to improve the cell response at long wavelengths. A record efficiency for high bandgap III-V cell grown with MBE was certified at 18.7%.

Finally, a process was elaborated to transfer the active III-V layers on a host support (glass or Si wafers). With a full back-metallization of the III-V cell and a planar host, the transfer process was successful and the photo-conversion efficiency of the transferred structures was similar to that of the "normal" cells. First attempts to implement the transfer with grid back-contacts (necessary for a tandem use) have revealed mechanical problems due to the stress at the interface between the III-V stack and the bonding polymer during curing. Solutions have been tested and are apparently satisfying, but need a validation by cell measurements.

Perspectives

The results presented above give good hints to improve the GaInP cells. In the future, a better understanding of the factor impacting the electronic properties of the material is needed. The impurities responsible for the residual doping of GaInP and for its poor hole mobility have to be identified. The test of purer elemental P sources may already lead to significant improvements. Then, growth contaminants could be limited by adjusting the growth procedure. As an example, substrate deoxidation in a separate chamber could avoid Oxygen release in the growth chamber. The use of phosphine as a P precursor could also be a relevant solution. Indeed, hydrogen radicals can be beneficial to prevent the incorporation of impurities in the growing layers or be efficient to passivate some punctual defects (this might partly explain the good MOCVD-grown GaInP properties obtained by some groups). This benefit could be exploited in the so-called "gas-source MBE" configuration (with elemental sources for group III + hydrides for group V species).

It is at the price of an acute attention to conditions reducing the presence of impurities in the MBE chamber that the photo-conversion efficiency of the PV cells will reach state-of-the-art figures.

In my opinion the short-term perspectives for the project must focus on the tandem process. Catching up with best high bandgap III-V cells is demanding, moreover intrinsic limits of MBE growth may be difficult to overcome and could prevent the team to compete with the best MOVPE-grown cells.

Finally, the GaInP/AlGaAs hetero-structure appears as an interesting path to remove these barriers and reach the 20% efficiency goal for the top cell. That is why, the main work axis for the laboratory has to be the development of the transfer of III-V cell and its bonding for the elaboration of a full tandem. First challenge to overcome, is related to the patterned back-contact of the III-V cell and the cleaving issues observed here. Then, the increase of the sample area which can be transferred on Si cells can be a major obstacle for the IPVF, and more generally for the large-scale production of this particular III-V/Si tandem process. Currently the tandem cells are limited to a 1 cm^2 area. Increasing the cells to a few cm^2 and then to a full wafer is not straightforward, the mechanical and inhomogeneity issues scaling with the wafer size.

Longer term perspectives lies at the IPVF project scale. During these three years, I became aware of other stakes of Photovoltaics. Too often, we focus ourselves on physical figures while the field is highly competitive and somehow in race for the highest efficiency. However, the development of PV technologies for market application demand so many resources in both investment and time, that the community must also tackles the issues linked to the sustainability of the solution, and their compatibility with production lines. Indeed, technologies which are not based on Si, struggle to enter the PV market and eventually lose market share with the years. Next processes have to develop the tandem solution as an "upgrade" of standard Si solar cells, meaning that the tandem devices can be fabricated with minor changes to the Si cell and add the less steps to the Si process flow. Regarding the sustainability, the use of AlGaAs appears as underrated solution to my eyes. Indeed, GaInP performs better that its arsenide competitor but AlGaAs offer less sensible growth: no ordering or composition modulations, no specific composition needed for lattice matching, a bandgap value only depending on the composition... AlGaAs permit to avoid the use of Indium, much rarer than Aluminum, which should prevent any raise of the price of the raw material composing the devices. It appears more sustainable from a resource point of view and more robust to growth and process variations. It therefore leads to equivalent efficiency for less constrains. The ideal solar cell is not the highest efficiency cell, it is a cell combining efficiency to low costs. Therefore a PV cell using abundant resources and offering the less challenges for fabrication has an advantage.

Communications:

- A.Michaud, Journées Nationales du Photovoltaïque (JNPV), Dourdan, France, Décembre 2017 (poster)
- A Michaud, Concentrated Photovoltaic Conference (CPV-14), Puertollano, Spain, April 2018 (poster)
- A Michaud, European PV solar ernergy conference and exhibition (EU PVSEC), Brussels, Septembre 2018 (poster)
- A Michaud, Workshop sur la Transistion Energétique, Palaiseau, France, Novembre 2018 (poster)
- A Michaud, IEEE Photovoltaic Specialist Conference (PVSEC 46), Chicago, USA, Juin 2019 (poster)

Publications:

- A. Ben Slimane, A. Michaud,O. Mauguin,X.Lafosse, J-C. Harmand, S. Collin, "1.73eV AlGaAs-based solar cell grown by MBE" submitted to Progress in Photovoltaics, Research and appplications
- A Michaud, A. Ben Slimane, A.Bercegol, R. Lachaume, L. Lombez, J-C. Harmand, J. Fernandez Martin, S. Collin, " Elaboration of III-V top cell for tandem cell with Silicon" ,submitted to IEEE 46th Photovoltaic Specialists Conference (PVSC), 2019

List of Figures

List of Tables

Bibliography

[1] Alan J Heeger. Soalr fuels and artificial photosynthesis. Science and innovation to change our future energy options. *Royal Society of chemistry*, (January):1–23, 2012.

[2] Photosynthesis. *https://www.ck12.org/biology/photosynthesis-summary/lesson/Photosynthesis-Advanced-BIO-ADV/*.

[3] Dr. Simon Philips and Werner Warmuth. Fraunhofer ISE: Photovoltaics Report, updated: 14 March 2019. (March), 2019.

[4] Renewable Energy Policy Network for the 21st century REN21. *Renewables 2018 Global status report*. 2017.

[5] Tenth Edition. International Technology Roadmap for Photovoltaic, 2018 results. (March), 2019.

[6] IPCC. *Global Warming of 1.5 degree, Summary for Policymakers*. 2018.

[7] BP. BP Energy Outlook 2019 edition. 2019.

[8] William Shockley and Hans J. Queisser. Detailed balance limit of efficiency of p-n junction solar cells. *Journal of Applied Physics*, 32(3):510–519, 1961.

[9] Hung Ling Chen, Andrea Cattoni, Nicolas Vandamme, Julie Goffard, Aristide Lemaitre, Amaury Delamarre, Benoit Behaghel, Kentaroh Watanabe, Masakazu Sugiyama, Jean Francois Guillemoles, and Stephane Collin. 200nm-thick GaAs solar cells with a nanostructured silver mirror. *2017 IEEE 44th Photovoltaic Specialist Conference, PVSC 2017*, pages 1–4, 2018.

[10] D. Knig, K. Casalenuovo, Y. Takeda, G. Conibeer, J. F. Guillemoles, R. Patterson, L. M. Huang, and M. A. Green. Hot carrier solar cells: Principles, materials and design. *Physica E: Low-Dimensional Systems and Nanostructures*, 42(10):2862–2866, 2010.

[11] Louise C. Hirst and Nicholas J. Ekins-Daukes. Fundamental losses in solar cells. *Progress in Photovoltaics: Research and Applications*, 19(3):286–293, 2011.

[12] Lev Kreinin, Ninel Bordin, Asher Karsenty, Avishai Drori, and Naftali Eisenberg. Experimental analysis of the increases in energy generation of bifacial over mono-facial PV modules. *Proceedings of the 26th European Photovoltaic Solar Energy Conference*, pages 3140–3143, 2011.

[13] Fabian Fertig, Sebastian Nold, Nico Wöhrle, Johannes Greulich, Ingrid Hädrich, Karin Krauß, Max Mittag, Daniel Biro, Stefan Rein, and Ralf Preu. Economic feasibility of bifacial silicon solar cells. *Progress in Photovoltaics: Research and Applications*, 24(6):800–817, 2016.

[14] R. Guerrero-Lemus, R. Vega, Taehyeon Kim, Amy Kimm, and L. E. Shephard. Bifacial solar photovoltaics - A technology review. *Renewable and Sustainable Energy Reviews*, 60:1533–1549, 2016.

[15] P. T. Chiu, D. C. Law, R. L. Woo, S. B. Singer, D. Bhusari, W. D. Hong, A. Zakaria, J. Boisvert, S. Mesropian, R. R. King, and N. H. Karam. 35.8% space and 38.8% terrestrial 5J direct bonded cells. *2014 IEEE 40th Photovoltaic Specialist Conference, PVSC 2014*, pages 11–13, 2014.

[16] Tatsuya Takamoto, Hidetoshi Washio, and Hiroyuki Juso. Application of InGaP/GaAs/InGaAs triple junction solar cells to space use and concentrator photovoltaic. *2014 IEEE 40th Photovoltaic Specialist Conference, PVSC 2014*, pages 1–5, 2014.

[17] Pan Dai, Lian Ji, Ming Tan, Shiro Uchida, Yuanyuan Wu, Aierken Abuduwayiti, Maliya Heini, Qi Guo, Lifeng Bian, Shulong Lu, and Hui Yang. Electron irradiation study of room-temperature wafer-bonded four-junction solar cell grown by MBE. *Solar Energy Materials and Solar Cells*, 171(March):118–122, 2017.

[18] Frank Dimroth, Matthias Grave, Paul Beutel, Ulrich Fiedeler, Christian Karcher, Thomas N.D. Tibbits, Eduard Oliva, Gerald Siefer, Michael Schachtner, Alexander Wekkeli, Andreas W. Bett, Rainer Krause, Matteo Piccin, Nicolas Blanc, Charlotte Drazek, Eric Guiot, Bruno Ghyselen, Thierry Salvetat, Aurélie Tauzin, Thomas Signamarcheix, Anja Dobrich, Thomas Hannappel, and Klaus Schwarzburg. Wafer bonded four-junction GaInP/GaAs//GaInAsP/GaInAs concentrator solar cells with 44.7% efficiency. *Progress in Photovoltaics: Research and Applications*, 22(3):277–282, 2014.

[19] Sascha Van Riesen, Martin Neubauer, Alexander Boos, Miguel Munoz Rico, Christophe Gourdel, Sven Wanka, Rainer Krause, Pascal Guernard, and Andreas Gombert. New module design with 4-junction solar cells for high efficiencies. *AIP Conference Proceedings*, 1679, 2015.

[20] Marina Buljan, João Mendes-Lopes, Pablo Benítez, and Juan Carlos Miñano. Recent trends in concentrated photovoltaics concentrators' architecture. *Journal of Photonics for Energy*, 4(1):040995, 2014.

[21] Muhammad Burhan, Muhammad Wakil Shahzad, and Kim Choon Ng. Long-term performance potential of concentrated photovoltaic (CPV) systems. *Energy Conversion and Management*, 148:90–99, 2017.

[22] Fraunhofer ISE and NREL. Current Status of Concentrator Photovoltaik Technology. 2015.

[23] Bifacial modules Soitec tracker. *https://www.solarpowerworldonline.com/2018/04/what-are-bifacial-solar-modules/.*

[24] Zhengshan J. Yu, Joe V. Carpenter, and Zachary C. Holman. Techno-economic viability of silicon-based tandem photovoltaic modules in the United States. *Nature Energy*, 3(9):747–753, 2018.

[25] Manoj Jaysankar, Miha Filipič, Bartosz Zielinski, Raphael Schmager, Wenya Song, Weiming Qiu, Ulrich W. Paetzold, Tom Aernouts, Maarten Debucquoy, Robert Gehlhaar, and Jef Poortmans. Perovskite-silicon tandem solar modules with optimised light harvesting. *Energy and Environmental Science*, 11(6):1489–1498, 2018.

[26] Florent Sahli, Jérémie Werner, Brett A. Kamino, Matthias Bräuninger, Raphaël Monnard, Bertrand Paviet-Salomon, Loris Barraud, Laura Ding, Juan J. Diaz Leon, Davide Sacchetto, Gianluca Cattaneo, Matthieu Despeisse, Mathieu Boccard, Sylvain Nicolay, Quentin Jeangros, Bjoern Niesen, and Christophe Ballif. Fully textured monolithic perovskite/silicon tandem solar cells with 25.2% power conversion efficiency. *Nature Materials*, 17(9):820–826, 2018.

[27] Tomas Leijtens, Kevin A. Bush, Rohit Prasanna, and Michael D. McGehee. Opportunities and challenges for tandem solar cells using metal halide perovskite semiconductors. *Nature Energy*, 3(10):828–838, 2018.

[28] Kelsey A. W. Horowitz, Michael Woodhouse, Lynn Gedvilas, Paul A. Basore, and David C. Bobela. Economic competitiveness of III-V on silicon tandem one-sun photovoltaic solar modules in favorable future scenarios. *Progress in Photovoltaics: Research and Applications*, 25(1):41–48, 2016.

[29] Timothy et al Ward, J. Scott; Remo. Techno economic analysis of three different substrate removal and reuse strategies for III/V solar cells. *Prog. Photovolt: Res. Appl.*, 24(September):1284–1292, 2016.

[30] Jongseung Yoon, Sungjin Jo, Ik Su Chun, Inhwa Jung, Hoon Sik Kim, Matthew Meitl, Etienne Menard, Xiuling Li, James J. Coleman, Ungyu Paik, and John A. Rogers. GaAs photovoltaics and optoelectronics using releasable multilayer epitaxial assemblies. *Nature*, 465(7296):329–333, 2010.

[31] G. J. Bauhuis, P. Mulder, E. J. Haverkamp, J. C.C.M. Huijben, and J. J. Schermer. 26.1% thin-film GaAs solar cell using epitaxial lift-off. *Solar Energy Materials and Solar Cells*, 93(9):1488–1491, 2009.

[32] G. J. Bauhuis, P. Mulder, E. J. Haverkamp, J. J. Schermer, E. Bongers, G. Oomen, W. Köstler, and G. Strobl. Wafer reuse for repeated growth of III-V solar cells. *Progress in Photovoltaics: Research and Applications*, 18(3):155–159, 2010.

[33] Romain Cariou, Jan Benick, Frank Feldmann, Oliver Höhn, Hubert Hauser, Paul Beutel, Nasser Razek, Markus Wimplinger, Benedikt Bläsi, David Lackner, Martin Hermle, Gerald Siefer, Stefan W. Glunz, Andreas W. Bett, and Frank Dimroth. III-V-on-silicon solar cells reaching 33% photoconversion efficiency in two-terminal configuration. *Nature Energy*, 3(4):326–333, 2018.

[34] Stephanie Essig, Christophe Ballif, Myles A. Steiner, Christophe Allebé, Adele Tamboli, Timothy Remo, John F. Geisz, Antoine Descoeudres, Kelsey Horowitz, Michael Woodhouse, David L. Young, Matthieu Despeisse, Manuel Schnabel, J. Scott Ward, and Loris Barraud. Raising the one-sun conversion efficiency of III V/Si solar cells to 32.8% for two junctions and 35.9% for three junctions. *Nature Energy*, 2(9):17144, 2017.

[35] Juan C. Jimeno, Rubén Gutierrez, Vanesa Fano, Ahmed Habib, Carlos Del Cañizo, Muhammad A. Rasool, and Aloña Otaegi. A 3 Terminal Parallel Connected Silicon Tandem Solar Cell. *Energy Procedia*, 92:644–651, 2016.

[36] Tomonori Nagashima, Kenichi Okumura, Kiyohito Murala, and Yoshio Kimura. Three-terminal tandem solar cells with a back-contact type bottom cell. *Conference Record of the IEEE Photovoltaic Specialists Conference*, 2000-Janua:1193–1196, 2000.

[37] Bouchier Daniel Connolly James P, Mercaraglia Denis, Renard Charles. Designing III-V multijunction solar cells on silicon. *Progress in Photovoltaics: Research and Applications*, 22(7):810–820, 2014.

[38] Thomas P White, Niraj N Lal, and Kylie R Catchpole. Tandem Solar Cells Based on High-Efficiency for $>$ 30 % Efficiency. *IEEE Journal of Photovoltaics*, 4(1):208–214, 2014.

[39] S M Vernon, M Geoffroy, M M Sanfacon, Spire Corporation, and One Patriots. High efficiency concentrator cells from GaAs on Si. (5):353–357, 1991.

[40] Arthur Onno, Jiang Wu, Qi Jiang, Siming Chen, Mingchu Tang, Yurii Maidaniuk, Mourad Benamara, Yuriy I. Mazur, Gregory J. Salamo, Nils Peter Harder, Lars Oberbeck, and Huiyun Liu. Al0.2Ga0.8As Solar Cells Monolithically Grown on Si and GaAs by MBE for III-V/Si Tandem Dual-junction Applications. *Energy Procedia*, 92:661–668, 2016.

[41] Carrie L. Andre, John A. Carlin, John J. Boeckl, David M. Wilt, M. A. Smith, A. J. Pitera, M. L. Lee, Eugene A. Fitzgerald, and Steven A. Ringel. Investigations of high-performance GaAs solar cells grown on Ge-Si1-xGex-Si substrates. *IEEE Transactions on Electron Devices*, 52(6):1055–1060, 2005.

[42] Giuliano Vescovi, Damir Asoli, Umear Naseem, James P Gilboy, Christian Sundvall, Andreas Dahlgren, K Erik Svensson, Nicklas Anttu, Mikael T Bj, and Lars Samuelson. A GaAs Nanowire Array Solar Cell With 15 . 3 %. *IEEE Journal of Photovoltaics*, 6:185, 2016.

[43] Gwenaëlle Hamon, Nicolas Vaissiere, Romain Cariou, Raphaël Lachaume, José Alvarez, Wanghua Chen, Jean-Paul Kleider, Jean Decobert, and Pere Roca i Cabarrocas. Plasma-enhanced chemical vapor deposition epitaxy of Si on GaAs for tunnel junction applications in tandem solar cells. *Journal of Photonics for Energy*, 7(2):022504, 2017.

[44] Karen Derendorf, Stephanie Essig, Eduard Oliva, Vera Klinger, Tobias Roesener, Simon P. Philipps, Jan Benick, Martin Hermle, Michael Schachtner, Gerald Siefer, Wolfgang Jäger, and Frank Dimroth. Fabrication of GaInP/GaAs//Si solar cells by surface activated direct wafer bonding. *IEEE Journal of Photovoltaics*, 3(4):1423–1428, 2013.

[45] M. M.R. Howlader, P. R. Selvaganapathy, M. Jamal Deen, and T. Suga. Nanobonding technology toward electronic, fluidic, and photonic systems integration. *IEEE Journal on Selected Topics in Quantum Electronics*, 17(3):689–703, 2011.

[46] Laura Vauche, Elias Veinberg Vidal, C Jany, J Decobert, Cécilia Dupré, and Pierre Mur. Development of III-V on Si Multijunction Photovoltaics by Wafer Bonding. *IEEE Journal of Photovoltaics*, (November):1–5, 2017.

[47] Stephanie Essig, Christophe Allebe, John F. Geisz, Myles A. Steiner, Bertrand Paviet-Salomon, Antoine Descoeudres, Adele Tamboli, Loris Barraud, Scott Ward, Nicolas Badel, Vincenzo Lasalvia, Jacques Levrat, Matthieu Despeisse, Christophe Ballif, Paul Stradins, and David L. Young. Boosting the efficiency of III-V/Si tandem solar cells. *2017 IEEE 44th Photovoltaic Specialist Conference, PVSC 2017*, pages 1–3, 2018.

[48] J. F. Geisz, M. A. Steiner, I. García, S. R. Kurtz, and D. J. Friedman. Enhanced external radiative efficiency for 20.8% efficient single-junction GaInP solar cells. *Applied Physics Letters*, 103(4), 2013.

[49] P. Dai, S. L. Lu, Y. Q. Zhu, L. Ji, W. He, M. Tan, H. Yang, M. Arimochi, H. Yoshida, S. Uchida, and M. Ikeda. The investigation of GaInP solar cell grown by all-solid MBE. *Journal of Crystal Growth*, 378:604–606, 2013.

[50] Romain Cariou. Material Science Epitaxial growth of Si(Ge) materials on Si and GaAs by low temperature PECVD: towards tandem devices.

[51] S. A. Ringel, J. A. Carlin, C. L. Andre, M. K. Hudait, M. Gonzalez, D. M. Wilt, E. B. Clark, P. Jenkins, D. Scheiman, A. Allerman, E. A. Fitzgerald, and C. W. Leitz. Single-junction InGaP/GaAs solar cells grown on Si substrates with SiGe buffer layers. *Progress in Photovoltaics: Research and Applications*, 10(6):417–426, 2002.

[52] Masafumi Yamaguchi and Chikara Amano. Efficiency calculations of thin film GaAs solar cells on Si substrates. *Journal of Applied Physics*, 58(9):3601–3606, 1985.

[53] I. Kallfass, P. Pahl, H. Massler, A. Leuther, A. Tessmann, S. Koch, and T. Zwick. A 200 GHz monolithic integrated power amplifier in metamorphic HEMT technology. *IEEE Microwave and Wireless Components Letters*, 19(6):410–412, 2009.

[54] S.E Hopper; M Kauer; V Bousquet. InGaN multiple quantum well lased diodes grown by molecular beam epitaxy. *Electronics Letters*, 40(1):33,34, 2004.

[55] N. Somaschi, V. Giesz, L. De Santis, J. C. Loredo, M. P. Almeida, G. Hornecker, S. L. Portalupi, T. Grange, C. Antón, J. Demory, C. Gómez, I. Sagnes, N. D. Lanzillotti-Kimura, A. Lemaítre, A. Auffeves, A. G. White, L. Lanco, and P. Senellart. Near-optimal single-photon sources in the solid state. *Nature Photonics*, 10(5):340–345, 2016.

[56] Tom Foxon John Orton. Molecular beam epitaxy, a short story. *Oxford University Press*, 2015.

[57] A. Y. Cho. Film Deposition by Molecular-Beam Techniques. *Journal of Vacuum Science and Technology*, 8(5):S31–S38, 1971.

[58] http://lampx.tugraz.at/hadley/ss1/bands/bandstruc.

[59] M. C. DeLong, D. J. Mowbray, R. A. Hogg, M. S. Skolnick, J. E. Williams, K. Meehan, Sarah R. Kurtz, J. M. Olson, R. P. Schneider, M. C. Wu, and M. Hopkinson. Band gap of completely disordered Ga 0.52 In 0.48 P. *Applied Physics Letters*, 66(23):3185–3187, 2002.

[60] A. Gomyo, T. Suzuki, K. Kobayashi, S. Kawata, I. Hino, and T. Yuasa. Evidence for the existence of an ordered state in Ga0.5In 0.5P grown by metalorganic vapor phase epitaxy and its relation to band-gap energy. *Applied Physics Letters*, 50(11):673–675, 1987.

[61] I. Garcia, I. Rey-Stolle, C. Algora, W. Stolz, and K. Volz. Influence of GaInP ordering on the electronic quality of concentrator solar cells. *Journal of Crystal Growth*, 310(23):5209–5213, 2008.

[62] Yongming Zhao, Kuilong Li, Jianrong Dong, Hui Yang, Shuzhen Yu, Xulu Zeng, and Yurun Sun. Influence of GaInP ordering on the performance of GaInP solar cells. *Journal of Semiconductors*, 37(7):073001, 2016.

[63] S. F. Yoon, K. W. Mah, H. Q. Zheng, and P. H. Zhang. Effect of V/III ratio and temperature dependence of carrier concentration in partially ordered and disordered Ga0.52In0.48P grown on GaAs substrates. *Journal of Crystal Growth*, 208(1):197–204, 2000.

[64] Theresa M. Christian, Daniel A. Beaton, Kunal Mukherjee, Kirstin Alberi, Eugene A. Fitzgerald, and Angelo Mascarenhas. Amber-green light-emitting diodes using order-disorder Al xIn1-xP heterostructures. *Journal of Applied Physics*, 114(7), 2013.

[65] Angelo Mascarenhas. Spontaneous Ordering in Semiconductor Alloys. 2002.

[66] J. S. Song, S. H. Seo, Y. C. Choi, H. S. Song, Y. H. Chang, M. H. Oh, D. C. Oh, T. Yao, J. H. Chang, C. S. Han, and K. W. Koo. High external emission efficiency in intentionally ordered GaInP/GaAs structures. *Applied Physics Letters*, 94(5), 2009.

[67] S. F. Yoon, K. W. Mah, H. Q. Zheng, and P. H. Zhang. Effects of substrate temperature on the properties of In0.48Ga0.52P grown by molecular-beam epitaxy using a valved phosphorus cracker cell. *Journal of Crystal Growth*, 191(4):613–620, 1998.

[68] K. W. Park, C. Y. Park, and Y. T. Lee. Band gap tunability of molecular beam epitaxy grown lateral composition modulated GaInP structures by controlling V/III flux ratio. *Applied Physics Letters*, 101(5):1–5, 2012.

[69] K. W. Park, C. Y. Park, Sooraj Ravindran, S. J. Kang, H. Y. Hwang, Y. D. Jho, Y. R. Jo, B. J. Kim, and Y. T. Lee. Enhancement of minority carrier lifetime of GaInP with lateral composition modulation structure grown by molecular beam epitaxy. *Journal of Applied Physics*, 116(4), 2014.

[70] B. J. Spencer, P. W. Voorhees, and J. Tersoff. Morphological instability theory for strained alloy film growth: The effect of compositional stresses and species-dependent surface mobilities on ripple formation during epitaxial film deposition. *Physical Review B - Condensed Matter and Materials Physics*, 64(23):2353181–23531831, 2001.

[71] C. Dorin, J. Mirecki Millunchick, Y. Chen, B. G. Orr, and C. A. Pearson. Lateral composition modulation in short period superlattices: The role of growth mode. *Applied Physics Letters*, 79(25):4118–4120, 2001.

[72] I. Vurgaftman, J. R. Meyer, and L. R. Ram-Mohan. Band parameters for III-V compound semiconductors and their alloys. *Journal of Applied Physics*, 89(11 I):5815–5875, 2001.

[73] Laurent Grenouillet. Spectroscopie optique de nouveaux materiaux a base de (Ga,In)(N,As) pour la realisation de composants a cavite verticale emettant a 1.3 um sur substrat GaAs. 2001.

[74] Varshni YP. Temperature dependence of the energy gap in semiconductors. *Physica*, 34:149, 1967.

[75] C. Y. Liu, Shu Yuan, J. R. Dong, S. J. Chua, M. C.Y. Chan, and S. Z. Wang. Temperature-dependent photoluminescence of GaInP/AlGaInP multiple quantum well laser structure grown by metalorganic chemical vapor deposition with tertiarybutylarsine and tertiarybutylphosphine. *Journal of Applied Physics*, 94(5):2962–2967, 2003.

[76] Zhuo Deng, Jiqiang Ning, Zhicheng Su, Shijie Xu, Zheng Xing, Rongxin Wang, Shulong Lu, Jianrong Dong, Baoshun Zhang, and Hui Yang. Structural dependences of localization and recombination of photogenerated carriers in the top gainp subcells of GaInP/GaAs double-junction tandem solar cells. *ACS Applied Materials and Interfaces*, 7(1):690–695, 2015.

[77] Shigekazu Minagawa, Yoshihiro Hamakawa, Youji Inoue, Masahiko Kondow, and Taneo Nishino. Anomalous temperature dependence of the ordered Ga 0.5 In 0.5 P photoluminescence spectrum . *Applied Physics Letters*, 54(18):1760–1762, 2002.

[78] https://attolight.com/.

[79] Thomas Neisius. Techniques EDX , EELS et HAADF en TEM : possibilités d ' analyse et applications.

[80] FIB preparation. *https://sal.nanofab.utah.edu/files/2014/07/FIB-1.png*.

[81] Yiyi Wang, Ahmet S. Özcan, Gözde Özaydin, Karl F. Ludwig, Anirban Bhattacharyya, Theodore D. Moustakas, Hua Zhou, Randall L. Headrick, and D. Peter Siddons. Real-time synchrotron x-ray studies of low- and high-temperature nitridation of c -plane sapphire. *Physical Review B - Condensed Matter and Materials Physics*, 74(23):1–11, 2006.

[82] S. K. Tiku. Self-Compensation in Rapid Thermal Annealed Silicon-Implanted Gallium Arsenide. *Journal of The Electrochemical Society*, 132(9):2237, 2006.

[83] C. M. Wolfe and G. E. Stillman. Self-compensation of donors in high-purity GaAs. *Applied Physics Letters*, 27(10):564–567, 1975.

[84] P. Blood, J. S. Roberts, and J. P. Stagg. GaInP grown by molecular beam epitaxy doped with Be and Sn. *Journal of Applied Physics*, 53(4):3145–3149, 1982.

[85] S. P. Najda, A. Kean, R. W. Streater, and A. J. Springthorpe. SIMS measurements of oxygen impurities in AlGaInP semiconductor material and laser diodes. *Journal of Crystal Growth*, 220(3):226–230, 2000.

[86] S. Heckelmann, D. Lackner, F. Dimroth, and A. W. Bett. Material quality frontiers of MOVPE grown AlGaAs for minority carrier devices. *Journal of Crystal Growth*, 464:49–53, 2017.

[87] K. Akimoto, M. Kamada, K. Taira, M. Arai, and N. Watanabe. Photoluminescence killer center in AlGaAs grown by molecular-beam epitaxy. *Journal of Applied Physics*, 59(8):2833–2836, 1986.

[88] N. Xiang, A. Tukiainen, J. Dekker, J. Likonen, and M. Pessa. Oxygen-related deep level defects in solid-source MBE grown GaInP. *Journal of Crystal Growth*, 227-228:244–248, 2001.

[89] A. Le Corre, J. Caulet, M. Gauneau, S. Loualiche, H. L'Haridon, D. Lecrosnier, A. Roizes, and J. P. David. Influence of oxygen incorporation on beryllium-doped InGaAs grown by molecular beam epitaxy. *Applied Physics Letters*, 51(20):1597–1599, 1987.

[90] John C. Zolper, Albert G. Baca, and Scott A. Chalmers. Thermally stable oxygen implant isolation of p-type Al0.2Ga 0.8As. *Applied Physics Letters*, 62(20):2536–2538, 1993.

[91] A. E. Von Neida, S. J. Pearton, W. S. Hobson, and C. R. Abernathy. Interaction of Be and O in GaAs. *Applied Physics Letters*, 54(16):1540–1542, 1989.

[92] Hayato Kawasaki, Katsunori Konishi, Daisuke Adachi, Hisashi Uzu, Toru Irie, Kunta Yoshikawa, Kunihiro Nakano, Toshihiko Uto, Wataru Yoshida, Kenji Yamamoto, and Masanori Kanematsu. Silicon heterojunction solar cell with interdigitated back contacts for a photoconversion efficiency over 26%. *Nature Energy*, 2(5):17032, 2017.

[93] P. Würfel, T. Trupke, T. Puzzer, E. Schäffer, W. Warta, and S. W. Glunz. Diffusion lengths of silicon solar cells from luminescence images. *Journal of Applied Physics*, 101(12), 2007.

[94] Tsutomu Yamazaki, Yukiharu Uraoka, Takashi Fuyuki, Hayato Kondo, and Yu Takahashi. Photographic surveying of minority carrier diffusion length in polycrystalline silicon solar cells by electroluminescence. *Applied Physics Letters*, 86(26):262108, 2005.

[95] F. J. Schultes, T. Christian, R. Jones-Albertus, E. Pickett, K. Alberi, B. Fluegel, T. Liu, P. Misra, A. Sukiasyan, H. Yuen, and N. M. Haegel. Temperature dependence of diffusion length, lifetime and minority electron mobility in GaInP. *Applied Physics Letters*, 103(24), 2013.

[96] N. M. Haegel, T. J. Mills, M. Talmadge, C. Scandrett, C. L. Frenzen, H. Yoon, C. M. Fetzer, and R. R. King. Direct imaging of anisotropic minority-carrier diffusion in ordered GaInP. *Journal of Applied Physics*, 105(2), 2009.

[97] C. Scandrett, Arsen Sukiasyan, A. G. Norman, Homan Yuen, Ting Liu, T. Christian, N. M. Haegel, A. Mascarenhas, Evan Pickett, and Pranob Misra. Doping dependence and anisotropy of minority electron mobility in molecular beam epitaxy-grown p type GaInP. *Applied Physics Letters*, 105(20):202116, 2014.

[98] A. S. Gudovskikh, J. P. Kleider, N. A. Kalyuzhnyy, V. M. Lantratov, and S. A. Mintairov. Band structure at heterojunction interfaces of GaInP solar cells. *Solar Energy Materials and Solar Cells*, 94(11):1953–1958, 2010.

[99] N.A. Kaluzhniy, A.S. Gudovskikh, M.Z. Shvarts, V.M. Andreev, S.A. Mintairov, and V.M. Lantratov. Numerical modelling of GaInP solar cells with AlInP and AlGaAs windows. *Thin Solid Films*, 516(20):6739–6743, 2007.

[100] A. E. Kibbler, J. F. Geisz, D. J. Friedman, Sarah R. Kurtz, K. A. Bertness, and J. M. Olson. Passivation of Interfaces in High-Efficiency Photovoltaic Devices. *MRS Proceedings*, 573(May), 2011.

[101] M. Burgelman, P. Nollet, and S. Degrave. Modelling polycrystalline semiconductor solar cells. *Thin Solid Films*, 361:527–532, 2000.

[102] T. S. Kuan, P. E. Batson, T. N. Jackson, H. Rupprecht, and E. L. Wilkie. Electron microscope studies of an alloyed Au/Ni/Au-Ge ohmic contact to GaAs. *Journal of Applied Physics*, 54(12):6952–6957, 1983.

[103] G. Stareev. Formation of extremely low resistance Ti/Pt/Au ohmic contacts to p-GaAs. *Applied Physics Letters*, 62(22):2801–2803, 1993.

[104] Shulong Lu, Hiroshi Yoshida, Masayuki Arimochi, Hui Yang, Pan Dai, Masao Ikeda, Wei He, Shiro Uchida, and Lian Ji. High-efficiency GaAs and GaInP solar cells grown by all solid-state molecular-beam-epitaxy. *Nanoscale Research Letters*, 6(1):2–5, 2011.

[105] Taizo Masuda, Stephanie Tomasulo, Jordan R. Lang, and Minjoo Larry Lee. Comparison of single junction AlGaInP and GaInP solar cells grown by molecular beam epitaxy. *Journal of Applied Physics*, 117(9), 2015.

[106] Sadao Adachi. 12 Carrier Transport Properties. 2009.

[107] Z.Z. Sun, S.F. Yoon, and W.K. Loke. Electrical properties of silicon- and beryllium-doped GaInP and (AlGa)InP grown by solid source molecular beam epitaxy. *Journal of Crystal Growth*, 235(1-4):8–14, 2002.

[108] Hassanet Sodabanlu, Akinori Ubukata, Kentaroh Watanabe, Takeyoshi Sugaya, Yoshiaki Nakano, and Masakazu Sugiyama. Extremely High-Speed GaAs Growth by MOVPE for Low-Cost PV Application. *IEEE Journal of Photovoltaics*, 8(3):887–894, 2018.

[109] J. F. Zheng, J. D. Walker, M. B. Salmeron, and E. R. Weber. Interface segregation and clustering in strained-layer InGaAs/GaAs heterostructures studied by cross-sectional scanning tunneling microscopy. *Physical Review Letters*, 72(15):2414–2417, 1994.

[110] H. Toyoshima, T. Niwa, J. Yamazaki, and A. Okamoto. In surface segregation and growth-mode transition during InGaAs growth by molecular-beam epitaxy. *Applied Physics Letters*, 63(6):821–823, 1993.

[111] Masafumi Yamaguchi, Hiroyuki Yamada, Yasuhiro Katsumata, Kan Hua Lee, Kenji Araki, and Nobuaki Kojima. Efficiency potential and recent activities of high-efficiency solar cells. *Journal of Materials Research*, 32(18):3445–3457, 2017.

[112] R. R. King, D. Bhusari, A. Boca, D. Larrabee, X. Q. Liu, W. Hong, C. M. Fetzer, D. C. Law, and N. H. Karam. Band gap-voltage offset and energy production in next-generation multijunction solar cells. *Progress in Photovoltaics: Research and Applications*, 19(7):797–812, 2011.

[113] A. Van Geelen, P. R. Hageman, G. J. Bauhuis, P. C. Van Rijsingen, P. Schmidt, and L. J. Giling. Epitaxial lift-off GaAs solar cell from a reusable GaAs substrate. *Materials Science and Engineering B*, 45(1-3):162–171, 1997.

[114] Stephanie Essig, Myles A Steiner, Christophe Alleb, John F Geisz, Bertrand Paviet-salomon, Scott Ward, Antoine Descoeudres, Vincenzo Lasalvia, Loris Barraud, Nicolas Badel, Antonin Faes, Jacques Levrat, Matthieu Despeisse, Christophe Ballif, Paul Stradins, and David L Young. Realization of GaInP / Si Dual-Junction Solar Cells. *IEEE Journal of Photovoltaics*, 6(4):1012–1019, 2016.

[115] M. Mühlberger, I. Bergmair, A. Klukowska, A. Kolander, H. Leichtfried, E. Platzgummer, H. Loeschner, Ch Ebm, G. Grützner, and R. Schöftner. UV-NIL with working stamps made from Ormostamp. *Microelectronic Engineering*, 86(4-6):691–693, 2009.

[116] Mark A. Eddings, Michael A. Johnson, and Bruce K. Gale. Determining the optimal PDMS-PDMS bonding technique for microfluidic devices. *Journal of Micromechanics and Microengineering*, 18(6), 2008.

[117] Hongkai Wu, Bo Huang, and Richard N. Zare. Construction of microfluidic chips using polydimethylsiloxane for adhesive bonding. *Lab on a Chip*, 5(12):1393–1398, 2005.

[118] J. Dekker, A. Tukiainen, N. Xiang, S. Orsila, M. Saarinen, M. Toivonen, M. Pessa, N. Tkachenko, and H. Lemmetyinen. Annealing of the deep recombination center in GaInP/AlGaInP quantum wells grown by solid-source molecular beam epitaxy. *Journal of Applied Physics*, 86(7):3709–3713, 1999.

[119] Daniel J. Chmielewski, Kevin Galiano, Pran Paul, Drew Cardwell, Santino Carnevale, John A. Carlin, Aaron R. Arehart, Tyler J. Grassman, and Steven A. Ringel. Comparative study of 2.05 eV AlGaInP and metamorphic GaInP materials and solar cells grown by MBE and MOCVD. *2017 IEEE 44th Photovoltaic Specialist Conference, PVSC 2017*, pages 1–4, 2018.

[120] Adrien Bercegol, Daniel Ory, Daniel Suchet, Stefania Cacovich, Olivier Fournier, Jean Rousset, and Laurent Lombez. Quantitative optical assessment of photonic and electronic properties in halide perovskite. *Nature Communications*, 10(1), 2019.

[121] Kan Hua Lee, Keith W.J. Barnham, John S. Roberts, Diego Alonso-Alvarez, N. P. Hylton, Markus Fuhrer, and Nicholas J. Ekins-Daukes. Investigation of Carrier Recombination Dynamics of InGaP/InGaAsP Multiple Quantum Wells for Solar Cells via Photoluminescence. *IEEE Journal of Photovoltaics*, 7(3):817–821, 2017.

[122] T. Takamoto, E. Ikeda, H. Kurita, and M. Ohmori. Structural optimization for single junction InGaP solar cells. *Solar Energy Materials and Solar Cells*, 35(C):25–31, 1994.

[123] N. Xiang, A. Tukiainen, M. Pessa, J. Dekker, and J. Likonen. Oxygen impurities in Ga<inf>0.51</inf>In<inf>0.49</inf>P grown by solid-source molecular beam epitaxy. *Journal of Materials Science: Materials in Electronics*, 13(9):3–6, 2002.

[124] T. Martin, C. R. Stanley, A. Iliadis, C. R. Whitehouse, and D. E. Sykes. Identification of the major residual donor in unintentionally doped InP grown by molecular beam epitaxy. *Applied Physics Letters*, 46(10):994–996, 1985.

[125] T. Yokotsuka, A. Takamori, and M. Nakajima. Growth of heavily Be-doped AlInP by gas source molecular beam epitaxy. *Applied Physics Letters*, 58(14):1521–1523, 1991.

[126] Miyoko Oku Watanabe, Kouhei Morizuka, Masao Mashita, Yasuo Ashizawa, and Yasuhito Zohta. Donor levels in si-doped algaas grown by mbe. *Japanese Journal of Applied Physics*, 23(2):L103–L105, 1984.

[127] H Okamoto T Ishibashi, S Tarucha. Si and Sn doping in AlGaAs grown by MBE. *Japanese Journal of Applied Physics*, 8:L476–L478, 1982.

[128] Ken Takahashi, Yasushi Minagawa, and Shigeki Yamada. Improved efficiency of Al Ga As solar cells with a pp \ n \ n structure. *Solar Energy Materials*, 66:525–532, 2001.

[129] Iljong Kim, Yonghoon Cho, Kwanshik Kim, Byungdoo Choe, H Lim, Il-jong Kim, Yong-hoon Cho, Kwan-shik Kim, and Byung-doo Choe. Band lineup transition in AlGaAs / InGaP from capacitance voltage analysis. 3488:0–3, 1996.

[130] M R Islam, R V Chelakara, K G Fertitta, P A Grudowski, A L Holmes, F J Ciuba, Hewlett-packard Laboratories, and Palo Alto. The growth and characterization of AlGaAs double heterostructures for the evaluation of reactor and source quality. *Journal of Electronic Materials*, 24(6), 1995.

[131] Chikara Amano, Koshi Ando, and Masafumi Yamaguchi. The effect of oxygen on the properties of AlGaAs solar cells grown by molecularbeam epitaxy. *Journal of Applied Physics*, 2853, 1988.

[132] S. Collin A. Ben Slimane, A. Michaud, O.Mauguin, X. Lafosse, J-C. Harmand. 1.73 eV AlGaAs solar cell grown by MBE (submitted). *Progress in Photovoltaics: Research and Applications.*